Magnetic Field Generation in Laser-Plasma Interactions

Eleanor Rose Tubman

Doctor of Philosophy

University of York

Physics

September 2016

"The best and most beautiful things in the world cannot be seen or even touched. They must be felt within the heart"

Helen Keller

Abstract

The primary focus of this thesis is understanding the production of magnetic fields during laser-plasma experiments. Each chapter investigates a different mechanism of producing magnetic fields. The first is from the by-product of launching asymmetric shocks which drive Biermann battery generated magnetic fields. The second looks at the reconnection of magnetic fields between two laser focal spots and the third is from fields produced around a current carrying loop target.

Blast waves are investigated in the laboratory using a fast framing camera to capture multiple images on a single shot. In analysing the images, the blast wave's trajectory is compared to a Sedov-Taylor solution and the coupling of the laser energy into the shock wave is calculated to be 0.5-2%. The evolution of the blast wave's shape is characterised by fitting an ellipse to the outer edge and is observed to progress into a more symmetrical shape. Calculations show that two shocks produced in the interaction cause the change in ellipticity.

We experimentally demonstrate that when two laser spots are placed in close proximity reconnection occurs. Diagnostics, including proton radiography, X-ray detectors and an optical probe, record and diagnose the existence of a semi-collisional reconnection event. The experimental data and simulations show that both Nernst and anisotropic pressure effects need to be taken into account for understanding and predicting the correct plasma dynamics observed.

Magnetic fields are produced by driving a current through a loop attached to two plates and new measurements recording the voltages induced are presented in this thesis. It is found that the predicted values for the resistance, capacitance and inductance do not match those extracted from the experimental data and reasons for these are presented. Ideas for furthering this research to enhance our understanding in this area are given.

Contents

List of Tables

List of Figures

Acknowledgements

Firstly I would like to thank my supervisor Professor Nigel Woolsey. It has been through his supervision that I have been so fortunate to have opportunities that have led to such an interesting and enjoyable PhD. I am extremely grateful for his support and guidance through the last four years.

My time at the University of York has led me to meet many amazing people. The staff and students of the York Plasma Institute have given me help and light relief when needed. Thank you in particular to Philip Durey, Andy West, David Blackman, Martin Read, Andy Rossall, John Pasley and Kate Lancaster who always had my back and supported me. I would also like to extend my thanks to Chris Ridgers. He has always been enthusiastic any time I have stopped to consult him on some puzzling physics, no matter how little time he might have and has reminded me never to stop questioning things.

I would like to thank the York University Sailing and Windsurfing Club for showing me the ropes and giving me some much needed time out when things got stressful in my PhD. The members of this club have become some of the greatest friends and drinking buddies a person could meet!

Thank you to all those on experiments who have imparted knowledge and wisdom and when, after long hours, have come up with simplest of sentences that seem the funniest thing ever. Also thank you to those who have helped me in analysing results and listened patiently to me trying to figure things through for the nth time. I would like to thank in particular, although not limited to, Joe Cross, Archis Joglekar, Matt Hill, Nick Butler, Hugo Doyle, Clement Goyon, David Turnbull, Brad Pollock and Peter Kordell. Additionally I am very grateful to Peter Graham, Robbie Scott, Gordon Kam and Ben Esse, as well as some of the names already mentioned, who have helped me running simulations or analysing results for

sections of this thesis. Additionally I also extend my thanks to Gianluca Gregori and David Riley for inviting me to be involved in their experimental campaigns.

I also wish to thank the teams at the facilities I have completed experiments at; the Jupiter Laser facility, the Central Laser Facility and the Orion laser, AWE. I would like to especially thank Graham Cooper, Jon Skidmore, Matt Hill and Ed Gumbrell from AWE who were so instrumental in achieving the results that we did. Thanks also to Colin Danson who ensured the smooth running of the experiment. John Foster was a huge asset to our experiment at AWE and I cannot thank him enough for his time and effort he put in to this research. He is an exceptional example to learn by, from his care taken in both planning experiments and interpreting of results. I would like to thank the teams at RAL especially to Chris Spindloe and his team for putting together our targets for Vulcan and Orion, and James and Rob for helping in the target area. Without these teams this research would not be possible, and it is often through their hard work in maintaining the facilities and providing such key support that the data is of the quality it is.

I would like to acknowledge those who I have met and had great discussions with at conferences and realised we are definitely not alone in getting through the times when you start to lose your path. They have always been encouraging of my work and have made me feel not too weird a person when I get excited about magnetic fields!

Spending time abroad I have been privileged to work with some of the most inspirational people and I wish to thank them for letting me work along side them. Louise Willingale allowed me to work with her at the University of Michigan and inspired me into taking research further than my PhD. John Moody welcomed me at LLNL and through his excellent guidance and thorough approach to tackling the physics problems I was able to learn so much.

I would finally like to thank my family for always being there when I have needed them. They have provided me with the reminders that a PhD is such a unique experience and builds up your knowledge in a way that sometimes you have to step back to appreciate.

Declaration

I declare that the work presented in this thesis, except where it is otherwise stated, is based on my own research and has not been submitted previously for a degree in this or any other university. Part of the work presented in this thesis has been published in:

- E. R. Tubman et al. *Nanosecond Imaging of Jet- and Shock- Like Features*, IEEE Transactions on Plasma Science. **42**, 2496 (2014)

Each experiment described in this thesis was performed as a collaboration with other researchers. The author was involved in setting-up, running and collecting data from each of the experiments. Analysis of the results in Chapter 4 was done with the help of a code written by Mr. L. G. Kam. The simulations from FLASH supporting the results were run by Dr. R. H. H. Scott with input from the author. The majority of the experimental analysis was completed solely by the author.

Chapter 5 discusses an experiment conceived by Prof. Nigel Woolsey and developed and led by the author, with assistance from collaborators and the team at the Orion laser, AWE. The author's own analysis of the results is shown for the diagnostics presented. The design and interpretation of the spectrometer data was worked on with Mr. P. Durey, Dr. J. M. Foster and Mr. B. D. Esse. Simulations from NYM were run by Dr. P. Graham. Simulations in IMPACTA and discussions of the overall results was completed with Dr. A. S. Joglekar.

Thomson scattering results presented in Chapter 6 were analysed by Dr. C. Goyon and Dr. B. B. Pollock, and the calculations of the circuit-relevant parameters were calculated following the advice of Dr. J. D. Moody and Dr. A. Hazi.

Chapter 1

Introduction

High energy density physics systems can be created with the use of lasers, where plasmas generated are at pressures of greater than 1 Mbar [1]. Dawson discussed the uses of lasers for plasma formation in 1964 [2], where he calculated that, with high power lasers (>10^9 W), plasmas of keV temperatures could be formed. These could then be used to investigate interactions with magnetic fields, which are relevant to supernovae and collisionless shocks, as well as understanding other properties of plasmas. Since this paper was written, lasers have been proven to be of great scientific use and, due to further advancements in their technologies, the intensities achievable have enabled a broader range of astrophysical situations to be researched. There have been a number of papers reviewing how laboratory astrophysics has advanced our knowledge of the universe, such as by Ripin *et al.* 1989 [3], Rose 1991 [4], Remington *et al.* 2000 [5], Takabe 2001 [6], Bulanov *et al.* 2009 [7] and Belyaev *et al.* 2012 [8].

The development of high power laser facilities has been primarily driven by the use of lasers in inertial confinement fusion (ICF) research, as a possible renewable energy resource. The research being done into ICF continues to benefit numerous areas of laser-plasma physics, from enhancing knowledge on the extreme plasma conditions created to helping the understanding of shock physics and instabilities occurring both within experiments and astrophysical conditions. Modern high energy laser facilities are available for academic research, such as at the National Ignition Facility (NIF), Lawrence Livermore National Laboratories (LLNL) [9], the Orion laser at the Atomic Weapons Establishment (AWE) [10], the Laser Mégajoule at

Commissariat l'Energie Atomique [11], and the Omega laser at the University of Rochester [12], to name just some of the large laser facilities that exist. The experiments are accompanied by vast amounts of computational and theoretical research. This is discussed in another paper by Dawson [13], showing some of the breadth that simulations can be used for. Simulations and experimental data, being used in parallel, are of great importance. Improvements, to both lasers, plasma diagnostics and computers, mean that more complex problems can be addressed through a combination of modelling and experiments, giving greater insights into a wider range of astrophysics and plasma physics in general. [1]

1.1 Laboratory Astrophysics

Astrophysics is a study of distant objects. Information is gathered by the use of telescopes and interpreted using computer simulations and theories. The physics applied to the interpretation of the astrophysical objects can be tested in the laboratory. In the past few decades lasers have enabled laboratory experiments designed to simulate the dynamics and enhance our knowledge of laboratory astrophysics.

The scaling laws that allow these large astrophysical objects to be reproduced within the laboratory environment were discussed in a paper in 1977 by Connor and Taylor [14]. These laws are invariant under a wide variety of transformations. Ryutov *et al.* [15] extended these approaches to connect laboratory experiments to astrophysics using the Euler set of equations. This means that when considering two hydrodynamical systems, such as one which exists on a larger scale within the universe and one which exists on the laboratory scale, if they are geometrically similar, the systems will follow ideal hydrodynamics.

The original paper by Ryutov *et al.* [15] was written for the application of comparing experimental results to supernovae. The progressions of these scalings were further investigated in a paper Ryutov *et al.* in 2000 [16] by applying them to ideal magnetic hydrodynamics and also by Drake in 2000 [17] for high energy particles. The scaling of such experiments allows comparisons to take 3 forms, as explained by Takabe in 2001 [6] and Falize *et al.* in 2011 [18]. The first is where the experiment is *identical* to the astrophysical processes, such as in investigations

of the equation of state, atomic physics and opacities. These can be directly related to the larger scale physics due to the fundamental nature of these measurements. The second is when the experiment is *similar* to astrophysical objects and can be compared under scaling laws. Shocks and jets are examples of these systems, where knowledge gained from observations within the laboratory can be scaled to astrophysics even though they might be taking place on very different spatial and temporal scales. The final set of experiments are those which currently do not have a scaling law but the physics resembles that found in other phenomena. It is by these scalings that the understanding of physics gained within the laboratory can be applied to many plasma processes found in the universe.

Studies of supernova remnants (SNRs) and laboratory experiments have begun to explain how magnetic fields have come to exist in the universe. The Biermann battery process [19] and the turbulent amplification of magnetic fields at a shock front is one potential mechanism via which these magnetic fields are generated and amplified up to organised large-scale structures [20]. Blast waves are produced from large energy releases, which drive a rapid expansion of ejecta material, sweeping up surrounding material. The evolution of these blast waves progresses from an initial ballistic expansion to an adiabatic phase and then a radiative phase, until their dissipation. Research is being done into understanding both their evolution phases and their shape [21, 22, 23, 24]. The research into how the shape of the blast waves changes with time and how this generates magnetic fields is discussed within this thesis.

The magnetic fields surrounding the Earth are of great interest. The interactions these fields have with the solar wind in the Earth's magnetosphere is important due to the magnetic reconnection events that release energy stored in the magnetic field. The solar wind contains particles ejected from the sun's corona and these can be accelerated in the outflow region of the reconnection events. These particles are accelerated along the magnetic field lines and collide with atoms in the Earth's upper atmosphere, emitting light, seen as the aurora [25, 26]. This is just one of the many events that occur within the universe due to magnetic reconnection, and there are many more reconnection events occurring within other astrophysical plasmas, such as in accretion discs, SNRs and at the heliopause [27]. Within the last 25

years laboratory experiments, using laser-plasma interactions, have also been able to demonstrate a geometry that supports reconnection and this is a rapidly growing area of research [28, 29, 30].

1.2 Inertial Confinement Fusion

Lasers are also used in fusion research at facilities, such as the NIF. The development of fusion is a worldwide objective, either through using magnetic confinement fusion (MCF) or ICF. Fusion, if brought to a commercially-viable scale, can address, in part, the rising world energy demand and depleting carbon based resources, helping to mitigate adverse influence on local air quality and the global climate. The fuel used in most current fusion scenarios is a deuterium-tritium (DT) mixture as shown in Equation (1.1). This is due to the high probability of a reaction from the large cross-sections associated with the reactants.

$$\mathrm{D} + \mathrm{T} \rightarrow {}^{4}\mathrm{He}\ (3.5\ \mathrm{MeV}) + \mathrm{n}\ (14.1\ \mathrm{MeV}) \tag{1.1}$$

The energies are split between the products in the 3.5:14.1 ratio due conservation of momentum and the ratio of the masses of the neutron and helium particles. On fusing DT the neutron produced in the reaction, carrying 14.1 MeV of the energy would escape, into a surrounding blanket. The blanket could consist of a water layer or lithium layers, to be heated by the neutrons or to create tritium fuel after neutrons interact with it. Another attraction of using DT as a fuel for fusion is that deuterium is found in large quantities in sea water and tritium can be bred in a fusion reaction using a lithium blanket.

The two routes to fusion differ in their set-up and operating conditions. MCF uses large magnetic fields to confine the plasmas. Alternatively, in ICF reactions, the fuel is contained within a small capsule and the lasers are fired onto the fuel to compress and ignite it, producing surplus energy in the reaction. The NIF was expected to have achieved ignition in 2012 but this was not reached and now research is needed to address the reasons for this. Some of the most prominent problems are to better understand the instabilities such as the Rayleigh-Taylor instability and issues from non-symmetrical fuel capsules seeding mixing in the capsule. There are other

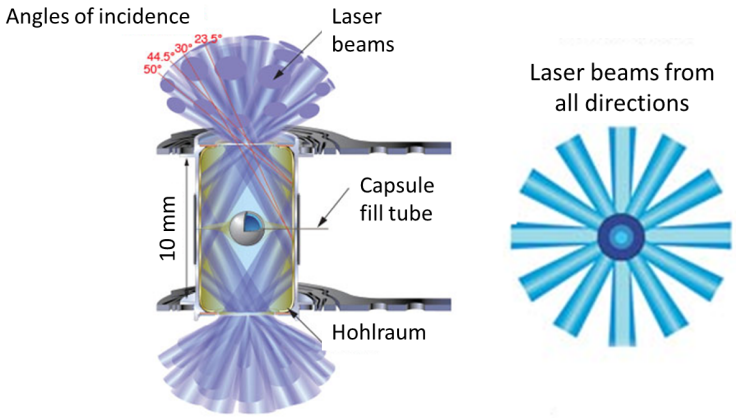

(a) Indirect drive **(b)** Direct drive

Figure 1.1: A diagram of an indirect and direct drive capsule for ICF with the laser beams focussed onto the hohlraum wall (1.1a) or directly onto the fuel (1.1b). [31]

effects not fully considered yet, such as magnetic field generation and reconnection in the plasma. The understanding of plasmas and magnetic fields interacting and potentially reconnecting is relevant to both MCF and ICF communities. In this thesis an experiment is conducted with the aim of creating a reconnection event applicable to laser-plasma interactions.

Within ICF there are two approaches to using the lasers to produce an implosion: direct and indirect drive. Schematics of these are shown in Figure 1.1. The NIF is currently a leader in using indirect drive, which uses a cylinder or hohlraum to enclose the fuel capsule. The lasers are fired in from opposite ends of the hohlraum and are incident on the hohlraum inner wall. This then emits X-rays that bathe the fuel capsule, causing the ablation of the capsule wall and compression of the fuel, and ultimately the ignition of the target. In direct drive research, being conducted at facilities such as the University of Rochester, the lasers are incident directly onto the target, to ablate the capsule wall and compress and heat the fuel to ignition [32].

It is hoped that with the continued investment of time and money, eventually one, or more, of these methods will reach the goal of producing commercially viable electricity.

1.3 Chapter Outline

Chapter 1 introduces the use of high power lasers for creating plasmas relevant to laboratory astrophysics studies and for developing ICF.

Chapter 2 presents an overview of relevant laser-plasma physics and the theory which will aid understanding of the subsequent chapters. Specifically, the theories of magnetic field generation, shock waves and magnetic reconnection are described.

Chapter 3 gives an overview of the research facilities used to conduct the experiments described in this thesis. Some diagnostics designed and fielded within these experiments, such as proton radiography, Thomson scattering and an X-ray spectrometer, are also explained.

Chapter 4 presents an experiment that was designed to primarily investigate magnetic field generation and amplification at a shock front. Results from an optical, fast framing camera are used to observe the Sedov-Taylor expansion of an emission front. Measurements are also made of the asymmetry of the emission front's shape with time. The experimental data from the camera is compared with data from other diagnostics, as well as 1D and 2D simulations.

Chapter 5 presents results from a magnetic reconnection experiment conducted at the Orion laser facility, suggesting a new reconnection mechanism. Proton radiography is the primary diagnostic used and an interpretation of the results, using both single and double laser spots on targets, is explained. The results from other diagnostics such as streaked interferometry, a gated X-ray detector and an X-ray spectrometer are also presented in support of the measurements made by the protons. Simulations run using two codes are also shown. Relevant parameters for a reconnection experiment are calculated, and the results discussed overall.

Chapter 6 presents results investigating the generation of magnetic fields around loop targets. The voltage generated by impacting loop targets with a laser are recorded using small circuit boards attached to the targets. The signals generated assist with understanding the laser plasma interaction, as well as developing models of the equivalent electrical circuits that make up the target components.

Chapter 7 concludes this thesis, summarising the results and findings in each of the chapters.

Chapter 2

Theory

This chapter introduces a state of matter called plasma and describes how plasmas can be created using lasers. The intensities of interest in this thesis are $10^{14} - 10^{16}$ W/cm^2 which are also relevant to ICF research. The theory presented in this chapter will outline the processes by which energy is absorbed from the laser pulse, as well as how magnetic fields are produced in laser-plasma interactions. The interaction of these fields can lead to magnetic reconnection and the different models for this will be discussed.

In the following chapters, equations and parameters are given in SI units. CGS units are commonly used in astrophysics, however SI units are used in physics in general. Within laboratory astrophysics or laser-plasmas either of these two systems can be implemented. The NRL Plasma Formulary gives conversions between the systems for different formulae, if further descriptions are required for equations given here [33].

2.1 Laser-Plasma Physics

2.1.1 Definition of a Plasma

Plasmas can be formed when a gas or solid is heated until it becomes ionised and exhibits collective behaviour. To be defined as a plasma, the matter must fulfil several criteria; that it behaves as a fluid, reacts to externally applied electric fields and that it remains quasi-neutral overall [34].

Quasi-neutrality is when a plasma contains equal numbers of negative and

positive charges. However, at local scales the charges might not be in exact equilibrium. This occurs when the plasma reacts to an external electric field. The electrons act to screen this field, increasing the number of electrons in a local region, although quasi-neutrality is still maintained within the bulk plasma. The Debye length, λ_D is a screening distance over which ions are shielded by electrons from these electric fields. The Debye length must be smaller than the size of the system, L, i.e. $\lambda_D \ll L$. If there is a plasma with a non-zero ion temperature then the ions will also contribute to the Debye shielding. If we assume that the ions are cold and immobile, the Debye length is given by Equation (2.1)

$$\lambda_D = \sqrt{\frac{\epsilon_0 k_B T_e}{n_e e^2}} \tag{2.1}$$

where n_e is the electron number density, ϵ_0=8.85 × 10⁻12 Fm^{-1}, T_e is the electron temperature, and e is the electric charge. The plasma parameter can then be calculated from the number of electrons in a Debye sphere, $N_D = \frac{4}{3}\pi n_e \lambda_D^3$.

In an external electric field the electrons and ions, of charge q, are forced in opposite directions, due to the Lorentz force, Equation (2.2)

$$\mathbf{F} = q\left(\mathbf{E} + \mathbf{v} \times \mathbf{B}\right) \tag{2.2}$$

where $\mathbf{F}$ is the force experienced, $\mathbf{E}$ is the electric field, $\mathbf{B}$ is the magnetic field and $\mathbf{v}$ is the velocity of the charged particle. The electrons will give energy to ions via Coulomb collisions, such that the relative momentum between the ions and electrons that are accelerated in the fields is balanced by the momentum dissipated in collisions. These collisions result in a resistivity η which is derived from Ohm's law,

$$\frac{e}{m_e}\mathbf{E} = -\nu_{ei}\mathbf{u_{rel}} \tag{2.3}$$

where $\mathbf{u_{rel}}$ is the relative velocity between the ions and electrons, ν_{ei} is the electron-ion collision frequency. Using the electric current, $\mathbf{J} = -n_e e \mathbf{u_{rel}}$ and resistivity, η,

$$\eta = \frac{m_e \nu_{ei}}{n_e e^2} \tag{2.4}$$

Equation 2.3 is rearranged to give

$$\mathbf{E} = \eta \mathbf{J} \tag{2.5}$$

Then taking the electron-ion collision frequency ν_{ei},

$$\nu_{ei} = \frac{n_e Z^2 e^4}{16\pi\epsilon_0^2 m_e^2 v_e^3} \tag{2.6}$$

the Spitzer resistivity, η_S, can be calculated [35], using the electron thermal velocity for v_e

$$\frac{1}{2} m_e v_e^2 = \frac{3}{2} k_B T_e \tag{2.7}$$

$$\eta_S = \frac{\pi Z e^2 m_e^{1/2} \ln\Lambda}{(4\pi\epsilon_0)^2 T_e^{3/2}} \tag{2.8}$$

where Z is the charge and m_e is the electron mass. A correction has been applied to the resistivity in Equation (2.8), called the Coulomb logarithm, $\ln\Lambda$. This accounts for the smaller scattering angles as well as large angle scatterings, which is what Equation (2.4) assumes. The Coulomb logarithm is the log of the ratio of the largest to the smallest distance the electron and ion will be separated, l_{max}/l_{min}, at collision. The Debye length is the maximum distance an electron will be from an ion for scattering to take place. l_{min}, the minimum distance, is approximated by the largest of either the classical distance of the closest approach or the de Broglie wavelength of the electron,

$$l_{min} = \max\left(\frac{Ze^2}{4\pi\epsilon_0 m_e v^2}, \frac{\hbar}{2m_e v_T}\right) \tag{2.9}$$

where $\hbar$ is the reduced Planck constant and v_T is the thermal velocity,

$$v_T = \sqrt{\frac{k_B T_e}{m_e}} \tag{2.10}$$

2.1.2 Kinetic and Fluid Theory

The final criteria for a plasma is that it must behave like a fluid, i.e. that it supports collective phenomenon, such as waves.

In describing the motion of a plasma, there are three methods that can be

used; particle, kinetic and hydrodynamic. The particle approach uses the equations of motion and Maxwell's equations for individual particles. For systems with many particles, such as a plasma, this requires a very large number of calculations. The kinetic theory uses distribution functions to represent ensembles of particles, for example the Vlasov-Fokker-Planck (VFP) equation describes the evolution of distributions. The hydrodynamic model takes into account the conservation laws and uses Maxwell's equations to describe a single fluid, with local thermodynamic equilibrium (where the plasma is in a Maxwell-Boltzmann distribution although radiation can be lost from the plasma overall [36]). However, this breaks down when the plasma becomes more collisional and then the kinetic approach is required.

The kinetic theory starts by assuming a distribution function $f(x,v,t)$ gives the number of particles in a volume by

$$dN = f(x,v,t)dxdydzdv_xdv_ydv_z \tag{2.11}$$

The total number of particles in a volume with a velocity of between v to $v+dv$ is

$$dn = f(x,v,t)dv_xdv_ydv_z \tag{2.12}$$

This function can be modified by either the electrons and ions colliding, or sources of particles and energy being added to the plasma. If we assume no additional sources then the distribution function evolution is given as $\frac{df}{dt} = C(f)$, so that

$$\frac{\partial f}{\partial t} + \frac{\partial x}{\partial t}\frac{\partial f}{\partial x} + \frac{\partial v}{\partial t}\frac{\partial f}{\partial v} = C(f) \tag{2.13}$$

$$\frac{\partial f}{\partial t} + (\mathbf{v}\cdot\nabla)f + \left(\frac{\partial \mathbf{v}}{\partial t}\cdot\nabla_{\mathbf{v}}\right)f = C(f) \tag{2.14}$$

Equation, (2.14), is the Boltzmann (kinetic) equation. In assuming a non-zero $\frac{\delta f}{\delta t}$ when short-range collisions are dominant, such as for weakly ionised gases, the moments of the kinetic equation are as shown in magnetohydrodynamics Equations (2.15)-(2.17).

$$n = \oint f(\mathbf{x}, \mathbf{v}, t) d^3\mathbf{v} \tag{2.15}$$

$$\mathbf{u} = \frac{1}{n} \oint \mathbf{v} f(\mathbf{x}, \mathbf{v}, t) d^3\mathbf{v} \tag{2.16}$$

$$K = \frac{1}{n} \oint \frac{1}{2} m v^2 f(\mathbf{x}, \mathbf{v}, t) d^3\mathbf{v} \tag{2.17}$$

where the zeroth moment, (2.15), gives the number density, the first moment, (2.16), gives the velocity, $\mathbf{u}$, of a fluid element and the second moment, 2.17, gives the mean kinetic energy, K. The moments can continue on to derive higher moments infinite times, however closure is needed. The moments are often truncated after the second moment. To do this the heat flux might be neglected, assuming an adiabatic plasma, or an equation of state used instead of the third moment.

If the plasma is collisionless then $C(f) = 0$. The resulting equation is known as the Vlasov equation, and is more commonly written as

$$\frac{\partial f}{\partial t} + \nabla.(f\mathbf{v}) + \frac{1}{m}(\mathbf{F}.\nabla_{\mathbf{v}}) f = 0 \tag{2.18}$$

where F is the standard Lorentz force. When integrating Equation (2.18) over all velocity space it gives the continuity equation, a description of the conservation of particle number density,

$$\frac{\partial n}{\partial t} + \nabla \cdot (n\mathbf{u}) = 0 \tag{2.19}$$

The Vlasov equation be further modified to give the force balance equation, multiplying by mv and integrating over velocity space with use of earlier equations, (2.15)-(2.17), to give,

$$mn\left[\frac{\partial \mathbf{u}}{\partial t} + (\mathbf{u}.\nabla)\mathbf{u}\right] + \nabla.\mathbf{P} - nq(\mathbf{E} + \mathbf{u} \times \mathbf{B}) = 0 \tag{2.20}$$

where $\mathbf{P}$ is the pressure tensor $P_{ij} = m \int f(\mathbf{x}, \mathbf{v}, t)(v_i v_j - u_i u_j) d^3\mathbf{v}$. These later equations, (2.19) and (2.20), give us some of the hydrodynamic equations.

If there is a highly ionised, collisional plasma, as is present in some of the experiments in this thesis, the VFP equation is used, where terms have been added to the right-hand side (RHS) of Equation (2.19) to account for electron-ion collisions [37, 38, 39].

$$\frac{\partial f}{\partial t} + \nabla.(f\mathbf{v}) + \frac{1}{m}(\mathbf{F}.\nabla_{\mathbf{v}}) f = -\nabla_{\mathbf{v}}\left(\frac{\langle \Delta \mathbf{v} \rangle}{\Delta t} f\right) + \frac{1}{2}\nabla_{\mathbf{v}}\nabla_{\mathbf{v}} : \left(\frac{\langle \Delta \mathbf{v} \Delta \mathbf{v} \rangle}{\Delta t} f\right) \tag{2.21}$$

Here the term with $\mathbf{\Delta v}$ describes the rate of advection and $\mathbf{\Delta v \Delta v}$ is the rate of diffusion.

All of the equations shown are used to describe a large number of physical processes within plasma physics.

2.1.3 Plasma Frequency

The fluid theory and hydrodynamic equations are an appropriate treatment of the propagation of the laser through the plasma. When an intense laser hits a target, it heats the target and provides enough energy to ionise the material. This creates a plasma, liberating electrons from the target, in an ablating plume. The propagation of the laser through an under-dense plasma can be described by the dispersion relation, Equation (2.22),

$$\omega_L^2 = k^2 c^2 + \omega_{pe}^2 \tag{2.22}$$

where ω_L is the laser frequency, k is the wavenumber and ω_{pe} is the electron plasma frequency. The electrons within the plasma oscillate at w_{pe} when displaced by perturbations from the heavier ions. The displacement creates a small charge separation with an electric field acting on the electron to restore it back to its original position. The electron plasma frequency is given by Equation (2.23), derived from the movement of a charged particle in a field, assuming a collisionless, uniform plasma with static or cold ions.

$$\omega_{pe} = \sqrt{\frac{n_0 e^2}{m_e \epsilon_0}} \tag{2.23}$$

The laser will also have an electric field associated with it, which is often expressed in terms of the normalised vector potential, a_0, as shown in Equation (2.24)

$$a_0 = \frac{eE}{m_e \omega_L c} \tag{2.24}$$

where E is the electric field of the laser. The intensity of the polarised laser light can then be described using a_0 as

$$I = 1.4 \times 10^{18} a_0^2 \lambda^2 \text{ W/cm}^2\mu\text{m}^2 \tag{2.25}$$

where λ is the wavelength of the laser in μm. For 1 μm lasers, intensities $> 10^{18}$ W/cm^2 and $a_0 \geq 1$ relativistic effects have to be considered, but when a_0 is much lower than this, as used within this thesis, then relativistic effects can be neglected.

The critical electron density is defined as being the point where the plasma frequency equals the laser frequency. When this happens, as shown by Equation (2.22), the wavenumber of the plasma wave, k, must go to zero. The laser will be able to propagate through a plasma of increasing density until the critical electron density where it is then reflected or absorbed, being allowed to travel no further into the target. The critical electron density is described by Equation (2.26).

$$n_{crit} = \frac{\epsilon_0 m_e \omega_L^2}{e^2} = \frac{1.1 \times 10^{21}}{\lambda_L[\mu\text{m}]^2} \text{cm}^{-3} \tag{2.26}$$

If the laser is required to travel further into a target, where the electron density is greater, then a laser of a higher frequency or shorter wavelength must be used.

2.1.4 Laser-Target Interaction Physics

The processes that occur when a laser of 1 μm wavelength hits a target are intensity and material dependent. Lasers of intensities $\leq 10^8$ W/cm^2 will heat the target causing material to evaporate, but it is only when the laser is above this intensity that it will start to ionise the target. For ionisation to occur the atom requires a photon of energy $E = h\nu$, where h is the Planck constant and ν is the frequency of the photon to be absorbed. A larger flux of photons ($\geq 10^9$ W/cm^2) onto target will provide enough energy for multi-photon ionisation. The ionisation results in free electrons, which are able to extract energy from the laser via collisional absorption. This will further heat the plasma. At intensities closer to 10^{14} W/cm^2 effects such as resonance absorption and scattering instabilities can also take place. These are outlined in the following sections.

Figure 2.1 shows the different regions a laser-plasma interaction creates on a solid density target. The laser is incident from the right, heating the material directly as it propagates into the target, until it reaches the critical density. The expanding plasma (region C) is of a low density and contains hot electrons. As a result this region will experience less effective collisional absorption. The temperature of this

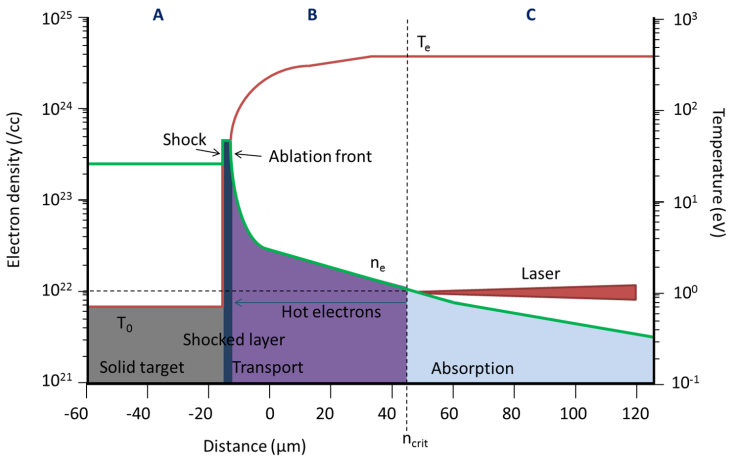

Figure 2.1: A diagram of of the laser-plasma interaction regions within a target. The graph shows the electron density and temperature profile for a laser of wavelength 0.35 μm and an intensity of 10^{15} W/cm^2 [1].

plasma cannot be increased any further by the laser.

Beyond the critical density (region B) conduction of the heat through the target is progressed by electrons which transport energy into higher densities. The ablation process, occurring at the ablation front, launches a shock wave into the target. Due to high pressures and conservation of momentum at the front, this compresses and heats the remaining target material (region A) [40].

The density scale length, L, of the plasma at the front surface of the target is defined by Equation (2.27). This is an important parameter, as the longer the scale length of the plasma, the better the absorption of the laser energy. However, longer scale lengths will also encourage heating of the plasma away from a central region, which in some experiments is not ideal and may enhance laser-plasma instabilities.

$$\frac{L}{n_e} = \frac{dz}{dn_e} \tag{2.27}$$

2.1.5 Absorption Processes

At laser intensities of $10^{12} - 10^{16}$ W/cm^2 the important absorption processes are inverse bremsstrahlung and resonance absorption.

2.1.5.1 Inverse Bremsstrahlung

Inverse bremsstrahlung is a collisional transfer of energy from the laser field to the electrons. Electrons oscillating in the field of the laser can interact with the electrostatic field of an ion and scatter, decoupling the electron from the laser and

remove energy from the beam. Further scattering of the electrons then heat the local surrounding plasma and target. This is the main absorption method when using lasers of intensities $10^{12} - 10^{15}$ W/cm^2.

The spatial damping rate of the laser energy due to inverse bremsstrahlung (κ) can be described by Equation (2.28), as derived by Wilks and Kruer [41],

$$\kappa \propto \frac{Z n_e^2}{T_e^{3/2}} \left(1 - \frac{n_e}{n_c}\right)^{-1/2} \tag{2.28}$$

where Z is the charge. The equation demonstrates the dependence of inverse bremsstrahlung absorption on the temperature and density of the material. A lower temperature, higher Z plasma will absorb more laser energy via inverse bremsstrahlung. It also shows that κ is increased closer to the critical surface. At the critical surface this expression tends to zero. This agrees with Equation (2.22) that at the critical surface the wavenumber goes to zero, where the laser cannot travel any further into the target.

2.1.5.2 Resonance Absorption

At the critical surface the laser energy of P-polarised light is absorbed by resonance absorption [42]. This is angle dependent and a major absorption process in this region. When the laser approaches the critical density and is refracted, the p-polarisation has an electric field vector perpendicular to the surface of the target at the critical density. This drives a plasma (Langmuir) wave and accelerates suprathermal electrons in the electric field. S-polarised light does not interact with the plasma wave as the electric field vector is not orientated in such a way to accelerate electrons [32, 43]. This is a non-collisional absorption mechanism which is efficient up to about 50%. The fraction of the energy absorbed by this process is

$$f_R = \frac{1}{2}(2.3\tau \exp^{-\frac{2\tau^3}{3}})^2 \tag{2.29}$$

where $\tau = (\omega L/c)^{1/3} \sin\theta$ and L is the plasma scale length. This is maximum when τ=0.8 giving an optimum angle of incidence, θ of 20-30° [43, 37].

The laser light is able to propagate as far as described by Equation (2.30)

$$n_e = n_c \cos^2(\theta) \tag{2.30}$$

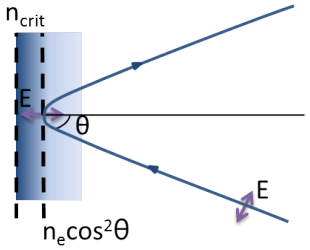

Figure 2.2: A diagram of resonance absorption and the maximum density the laser can propagate to before being refracted away from the surface.

where θ is the angle of incidence of the laser. The laser will approach the critical surface until it is specularly reflected back [44].

2.1.6 Parametric Instabilities

The laser light can also be absorbed by other plasma processes such as parametric instabilities. These are generally detrimental to the laser heating effect as the instabilities couple laser energy into non-thermal energies populations of electrons. There are 3 primary instabilities, stimulated Brillouin scattering (SBS), stimulated Raman scattering (SRS) and two-plasmon decay (TPD). If there is an external high-intensity wave (i.e. the laser) driven at a frequency ω_L and another oscillation wave existing within the plasma (i.e. the electron plasma wave) of frequency ω_{pe} then these two waves can generate side-bands with a combination of frequencies from these two waves [44]. These can then result in hot electrons and scattering of laser light.

TPD occurs when an incident laser photon decays into two plasmons. This occurs under the conditions of $\omega_{pe} = \frac{\omega_L}{2}$, when the plasma density is close to $n_c/4$. This instability only occurs in these very specific conditions. However, when there are steep density gradients the generation conditions are only present over small regions.

SRS involves an inelastic scattering of a photon into an electron plasma wave. This process takes place in densities of $< n_c/4$. When it occurs there is a broad-band of electron plasma waves frequencies that can be amplified, where the range is dependent on the electron density gradient.

SBS is when a photon is backscattered from a phonon, loosing momentum in the process. The phonon grows parametrically by the absorption of scattered photon

energy. This process takes place at any point where the density is $< \frac{n_c}{4}$.

In both the scattering processes they provide positive feedback. The electromagnetic wave left is able to scatter again, meaning these processes can grow exponentially.

2.1.7 Energy Transport

When energy has been absorbed from the laser the electrons assist in transporting it through the target, into areas of higher density that the laser cannot propagate to.

Ions, being much heavier than electrons, are slower, by a factor of $(m_i/m_e)^{1/2}$, than the electrons and so are neglected in considering heat transportation. The diffusion of heat within the target is given by the Spitzer-Harm equation

$$q_S = -\kappa_{SH} \nabla T \tag{2.31}$$

where q_S is the heat flow, ∇T is the temperature gradient inside the target and κ_{SH} is the Spitzer-Harm conductivity which depends on the temperature, $T^{5/2}$. This heat flow arises from a distortion of the Maxwellian velocity distribution. The Spitzer-Harm model works for small perturbations in the distribution, and also assumes that the electron mean free path, λ_e is smaller than the temperature scale length L_T. Beyond these assumptions the model breaks down, particularly in large temperature gradients. Electrons carry more energy away from the critical surface and, due to a charge imbalance, they set up an electric field. A return current is drawn to keep charge neutrality. The return current has a much lower energy, so the electrons from the critical density region travelling to the ablation surface contribute to net heating of the target. However, to model heat transport in a target in hydrodynamic codes, a flux limiter is added to fix how much of the heat flows with these hotter electrons. This is due to the hotter electrons having mean free path much longer than the temperature scale length, creating unrealistic scenarios. The value of the flux limiter is a currently debated topic, although not further discussed in this thesis [45].

Hot electrons, generated in the laser-plasma interactions, stream ahead of the bulk plasma. These electrons carry magnetic fields with them via the Nernst effect

[46]. This transport is described via the VFP equation, (2.21). Taking the first velocity moment of the VFP equation, (2.21), results in Ohm's law

$$\frac{e}{m_e}(\mathbf{E}+\mathbf{v}\times\mathbf{B}) = -\frac{\nabla\mathbf{P_e}}{n_e m_e} + \underline{\underline{\alpha^c}}\cdot\frac{\mathbf{j}}{n_e e} - \underline{\underline{\beta^c}}\cdot\frac{\nabla T_e}{m_e} \tag{2.32}$$

where $\underline{\underline{\alpha^c}}$ and $\underline{\underline{\beta^c}}$ are normalised resistivity and thermoelectric tensors. The $\beta_\wedge$ component of $\underline{\underline{\beta^c}}$ gives rise to this Nernst effect. Using the classical transport equations from Braginskii [47], a Nernst velocity is calculated, as shown by Haines [48]

$$v_N \approx \frac{2q_e}{5n_e k_B T_e} \tag{2.33}$$

where $q_e = -n_e T_e \tau_{ei} \kappa_\perp^c \cdot \nabla T_e / m_e$ and $\kappa_\perp^c$ is the normalized thermal conductivity tensor [49].

The magnetic fields produced in a laser-plasma can influence the electron transport due to the Lorentz force if the following conditions are met:

$$\omega_{ce}\tau_{ei} > 1 \tag{2.34}$$

$$\omega_{ce} = \frac{eB}{m_e c} \tag{2.35}$$

where τ_{ei} is the electron-ion collision time and ω_{ce} is the electron gyrofrequency.

2.2 Magnetic Field Generation

Magnetic fields can be generated in laser-plasma experiments via several mechanisms, both direct and indirect. One mechanism is the Biermann battery effect, published in 1950 by Biermann [19]. He observed that magnetic fields exist in stars and interstellar medium where none were thought to exist initially. The induction equation shown in Equation (2.36) does not explain where a magnetic field could be generated from if none existed to start with.

$$\frac{\partial\mathbf{B}}{\partial t} = \nabla\times(\mathbf{v}\times\mathbf{B}) + \frac{\eta}{\mu_0}\nabla^2\mathbf{B} \tag{2.36}$$

Instead Biermann derived an equation to describe the changing magnetic field using the momentum balance equation, where charge separation results in an electric field, and therefore growth of magnetic fields.

$$n_e m_e\left(\frac{d\mathbf{v_e}}{dt} + \mathbf{v_e}\cdot\nabla\mathbf{v_e}\right) = -n_e e\left(\mathbf{E} + \mathbf{v_e}\times\mathbf{B}\right) - \nabla p_e - v_e m_e(\mathbf{v_e} - \mathbf{v_i}) \tag{2.37}$$

where $\mathbf{v_e}$ is the electron velocity and p_e is an isotropic electron pressure. If inertial and resistive terms (the term on the left-hand side (LHS) and last term on the RHS, respectively) are dropped then Equation (2.38) is reached.

$$\mathbf{E} + \mathbf{v}\times\mathbf{B} = -\frac{\nabla p_e}{n_e e} \tag{2.38}$$

Finally by taking the curl of this equation and using Faraday's equation $\nabla\times\mathbf{E} = -\frac{\partial B}{\partial t}$ this yields Equation 2.39.

$$\frac{\partial\mathbf{B}}{\partial t} = \nabla\times(\mathbf{v}\times\mathbf{B}) - \frac{\nabla n_e\times\nabla p_e}{n_e e} \tag{2.39}$$

The second term on the RHS of this equation is the Biermann battery term, as when $B = 0$ the first term on the LHS is equal to zero. Therefore, to get a magnetic field generated the second term, on the LHS, needs to have non-parallel pressure and density gradients. This can be achieved under certain conditions. Generally pressure is also a function of density so the gradients are often parallel and there is no generation of magnetic fields. The pressure and density can be non-parallel when vorticity is present, such as when non-spherical shocks are produced. Vorticity is defined by $\omega = \nabla\times\mathbf{v}$ where $\mathbf{v}$ is the velocity of the shock. The magnetic field generated via this is [50]

$$B_{vort} = \frac{m_i\omega}{e} = \frac{(\rho-1)^2}{\rho}\frac{m_i}{e}\left|\frac{\partial\mathbf{v}_{shock}}{\partial S}\right| \tag{2.40}$$

where ρ is the shock compression ratio, m_i is the ion mass and $\partial v/\partial S$ is the tangential gradient of the shock velocity, which is proportional to the shape and symmetry of the shock [50]. Introducing asymmetry into a shock, therefore, results in vorticity, and the generation of magnetic fields.

Magnetic fields are also produced toroidally around a laser spot due to the laser driven non-parallel density and temperature gradients. There is a density gradient perpendicular to the target which increases towards the surface and a temperature gradient parallel to the target surface, around the laser spot edges. If the time-scales of the laser pulse duration (t) on the order of nanosecond, L_n the spatial scale

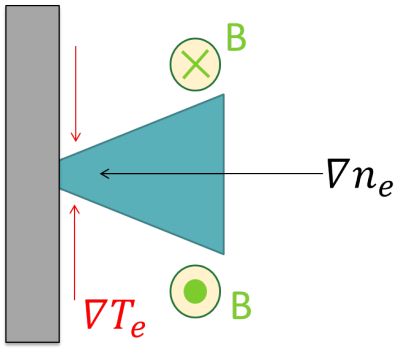

Figure 2.3: A diagram of the temperature and density gradients created at a laser spot and the resulting magnetic fields produced.

lengths around 10 μm, T_e electron temperatures up to 1 keV and L_T the temperature gradient scale length of several microns then magnetic fields calculated by Equation (2.39) can be approximated by Equation (2.41). For the case given here the magnetic fields would be on the order of megagauss [43].

$$\mathrm{B(MGauss)} \approx 10\left(\frac{\mathrm{t}}{1\ \mathrm{ns}}\right)\left(\frac{\mathrm{T_e}}{1\ \mathrm{keV}}\right)\left(\frac{30\ \mu\mathrm{m}}{\mathrm{L_n}}\right)\left(\frac{30\ \mu\mathrm{m}}{\mathrm{L_T}}\right) \tag{2.41}$$

2.3 Shock Waves

A few areas of particular interest to laboratory astrophysics are the magnetization of interstellar plasmas [50] and the role of shock waves in active galactic nuclei and young stellar objects. More recently shock wave experiments have explored how turbulent flow may amplify magnetic fields [20] and help explain the strong fields that exist within SNRs, such as Cassiopeia A [51].

Shock waves are produced when a large pressure is applied to a system and a hydrodynamic compression wave is created. The front of the shock wave is charac-

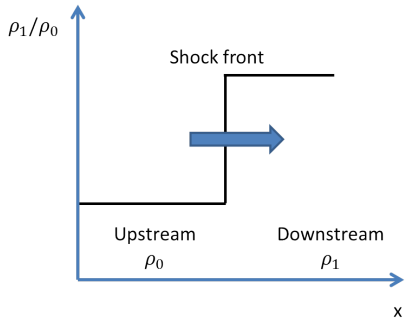

Figure 2.4: A diagram of the density jump across a shock front. The material, from the shock frame, appears to be travelling in the direction indicated by the blue arrow.

terised by a steep gradient in temperature and density, as it moves into unshocked material. As the shock does so it rapidly changes the material properties in the downstream region, shown in Figure 2.4. If the wave is moving faster than the local sound speed, then a shock wave can be supported. The conditions across the shock front are solved in the following equations, using the conservation of mass, momentum and energy in planar and steady state solutions. The subscripts 0 and 1 denote upstream and downstream regions, respectively.

$$\rho_1 u_1 = \rho_0 u_0 = \text{const.} \tag{2.42}$$

$$\rho_1 u_1^2 + p_1 = \rho_0 u_0^2 + p_0 = \text{const.} \tag{2.43}$$

$$\frac{1}{2}u_1^2 + \epsilon_1 + \frac{p_1}{\rho_1} = \frac{1}{2}u_0^2 + \epsilon_0 + \frac{p_0}{\rho_0} = \text{const.} \tag{2.44}$$

where ϵ is the specific internal energy. These three equations are known as the Rankine-Hugoniot relations. They assume that the shock is not radiative, that the shock width is infinitesimally small and that the upstream and downstream material is in a steady state for an extended region. These equations can also be used to calculate the density change over the shock front, using Equation (2.44) and rewriting it using the polytropic equation of state such that

$$\epsilon = \frac{1}{(\gamma - 1)}\frac{p}{\rho} \tag{2.45}$$

where $\gamma = C_p/C_v$, the ratio of specific heat at constant pressure to specific heat at constant volume. Assuming that γ does not change across the shock, it becomes

$$\frac{\rho_1}{\rho_0} = \frac{(\gamma+1)p_1 + (\gamma-1)p_0}{(\gamma+1)p_0 + (\gamma-1)p_1} = \frac{u_0}{u_1} \tag{2.46}$$

Then in the conditions of a strong shock when $p_1 >> p_0$ or $M \geq 10$ where M is the Mach number given by the ratio of the flow speed to the sound speed ($M = v/c_s$)

$$\frac{\rho_1}{\rho_0} \rightarrow \frac{\gamma+1}{\gamma-1} \tag{2.47}$$

Assuming a polytropic gas where $\gamma = 5/3$ then the ratio of the pre- to post-shock density is 4.

In an ideal gas the sound speed is given by Equation (2.48),

$$C_s = \sqrt{\frac{\gamma p}{\rho}} \tag{2.48}$$

where p is the pressure and ρ is the gas density. A shock compresses and heats the material in front of the shock as it passes over the front, in a process that is irreversible [1].

Radiative shocks are those which cool after the shock passes through the material, by the downstream region emitting radiation. The photons released in the cooling process can also irradiate the pre-shocked material forming a precursor to the shock. The peak temperature of the material will occur just after the shock front has passed through. The temperature will then decrease over a radiative, relaxation region while density increases to maintain the pressure balance. This is a main difference between non-radiative and radiative shocks; density can far exceed the non-radiative limit of 4.

2.3.1 Blast Waves

Blast waves, which are studied in this thesis, are a type of shock wave that occur in astrophysics, where the conditions are not assumed to be constant with time. In a SNR an explosion of ejecta mass (typically of about 1 solar mass)) will be released from a supernova, and expand out with a near constant velocity (about 10^4 km/s), much greater than the sound speed of the surrounding material. This drives a fast shock wave, the blast wave. As the blast wave expands outwards, the surrounding material is heated until the pressure of the heated material exceeds the thermal pressure of the ejecta. At this point a reverse shock is driven back, towards the explosion point. The ratio of densities of the upstream and downstream can be given by Equation (2.47). This initial phase is called the ballistic phase and will continue until the material being swept up by the shock equals that of the ejecta mass, $M_{ej} \approx M_{sweep}$. The radius at which this occurs is

$$R = \left(\frac{3M_{ej}}{4\pi\rho_0}\right)^{\frac{1}{3}} \tag{2.49}$$

where M_{ej} is the mass of the ejecta material and ρ_0 is the density of the interstellar medium.

After this point the blast wave will follow a Sedov-Taylor solution. This assumes that it is a point-like explosion where the finite mass of the ejecta, radiative losses and the pressure of the surrounding material have been considered to be negligible, as derived by Sedov [22], Taylor [24] and Von Neumann [52]. The Sedov-Taylor solution only depends on the energy in the shock, the time of the shock and the density of the pre-shock material.

$$R(t) \propto E^{\beta} \rho^{n} t^{\gamma} \tag{2.50}$$

By dimensional analysis of Equation (2.50), the values for each power can be found. This gives the Sedov-Taylor solution as shown in Equation (2.51), where R is the radius of the shock wave, αE is the fraction (α) of the energy (E) coupled into the shock, η is a dimensionless similarity variable given as 1.15167 [53] and ρ is the density. This Sedov-Taylor solution assumes a spherical geometry, therefore $\gamma = 2/5$.

$$R(t) = \eta \left(\frac{\alpha E}{\rho} \right)^{\frac{1}{5}} (t)^{\frac{2}{5}} \tag{2.51}$$

The interior of the SNR is still radiating and at a point late in its development the radiative losses will become important to the hydrodynamics. When this happens the blast wave enters the radiative phase and the shocked material will be able drop to lower temperatures than at the shock front. The rate of expansion of the blast wave will then slow quicker than $t^{-}3/5$. Then phases, such as a pressure driven snow-plough and a momentum conserving snowplough [54], can be reached by the blast wave, where the pressure pushes the shock front outwards or the blast wave conserves momentum continuing on its expansion. During these phases the relationship between R and t becomes closer to $R \propto t^{\frac{1}{4}}$. Gradually the shock front slows down even further and eventually fades away when the expansion velocity reaches c_s [55, 53].

2.4 Magnetic Field Reconnection

Magnetic reconnection is a phenomena that occurs in many astrophysical situations, for example at the Earth's magnetosphere and in the corona on the sun's surface. The plasmas in these situations are also described by the plasma-β, which is a ratio of the thermal pressure to magnetic pressure, as shown in Equation (2.52),

$$\beta = \frac{P_{th}}{P_B} = \frac{n_e T_e}{B^2/2\mu_0} \tag{2.52}$$

where the thermal pressure is $P_{th} = n_e T_e$ and the magnetic pressure is $P_B = B^2/2\mu_0$.

In astrophysical events the reconnection is considered collisionless, with a low plasma-β, due to strong magnetic field pressures. Low plasma-β reconnection events can also be encountered in tokamaks where densities are low, whereas the reconnection events that occur within a laser-plasma environment are often of high plasma-β.

In a reconnection event, opposing field lines are forced to break and reconnect to form lower energy configurations. Reconnection requires the formation of a current sheet between the two colliding fields, where the sheet is neutral and the resistivity can be high. This allows the magnetic fields to decouple from the electrons and ions and reorganise. Several parameters are important in describing a reconnection geometry. The first of which is the Lundquist number, S, given as

$$S = \frac{v_A L}{\eta} \tag{2.53}$$

where L is the is half the length of the reconnection layer, η is the plasma resistivity and v_A is the Alfvén velocity,

$$v_A = \sqrt{\frac{B^2}{2\mu_0 m_i n_i}} = \omega_{ci}\delta_i \tag{2.54}$$

where ω_{ci} is the ion gyrofrequency and δ_i is the ion skin depth. The Lundquist number describes the ratio of diffusive (2.55) to Alfvén (2.56) timescales,

$$\tau_{Diff} = \mu_0 L^2/\eta \tag{2.55}$$

$$\tau_A = L/v_A \tag{2.56}$$

The reconnection region, where the magnetic field decouples from the plasma, is very small in scale compared to the larger scale lengths of the global region. It is these small scales that make reconnection a challenging problem to model and characterise. In addition to the small scales, the rate of reconnection is important and currently an open question [56].

2.4.1 Sweet-Parker Reconnection

The model for magnetic reconnection was first published by Sweet (1958) [57] and Parker (1958) [58] who predicted the rate at which the reconnection occurs, assuming a system in steady state and as a single fluid. This model has a slow reconnection rate, where a current sheet is formed in between the reconnecting fields.

The resistivity is assumed to be low in the plasma, so that the magnetic fields are frozen-in-flow. When the plasmas come together and collide the resistivity increases. The plasma decouples from the fields and the magnetic fields rearrange themselves into a more stable and lower energy configuration. Energy is then released along the current sheet in the form of jets. The width of the reconnection region, 2δ, as shown in Figure 2.5, is dependent on the resistivity of the plasma and on the plasma inflow velocity, v_{in}.

$$\delta = \frac{\eta}{\mu_0 v_{in}} \tag{2.57}$$

The reconnection rate of this model is slow as the inflowing plasma is travelling at fractions of the Alfvén velocity. The outflow plasma, however, travels at

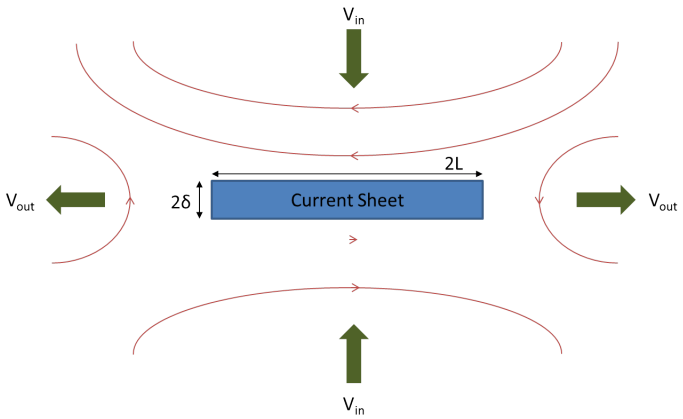

Figure 2.5: A diagram of Sweet-Parker reconnection where magnetic field lines are shown in red.

approximately the Alfvén velocity, having gained energy from magnetic energy being transferred to kinetic energy via resistive heating. Mass continuity requires the same amount of mass flowing into the reconnection region, Lv_{in}, to balance the mass flowing out, δv_{out}. The reconnection rate, therefore, is fixed by the inflow velocity. The Lundquist number, $S^{-1/2} = v_{in}/v_A$, (where the Alfvén velocity is assumed for v_{out}) is large in astrophysical systems and this means that the predicted reconnection rate from the inflow velocity is too slow to match the reconnection conditions occurring.

Although the model does not fit systems with large Lundquist numbers, it has been confirmed by the MRX magnetic reconnection machine by Ji *et al.* [59]. Resolving the issue of the rate of reconnection is not easy, due to requiring high resistivity in a region of small thickness. High resistivity, in turn, limits the width of the outflow, and therefore the outflow velocity, meaning that again there are limits on the inflow velocity for this model.

2.4.2 Petschek Reconnection

Petschek came up with a faster rate of reconnection in 1964 [60]. The rate of reconnection is increased by reducing the length of the current sheet to L', so that the ratio of the width to length of the dissipation region is lowered. This increases the plasma inflow velocities into the reconnection region, assuming that the diffusion region and external scale length do not have to be the same. Petschek decided this after observations that lines were reconnecting near one point and that the resistivity along a longer line is not necessary.

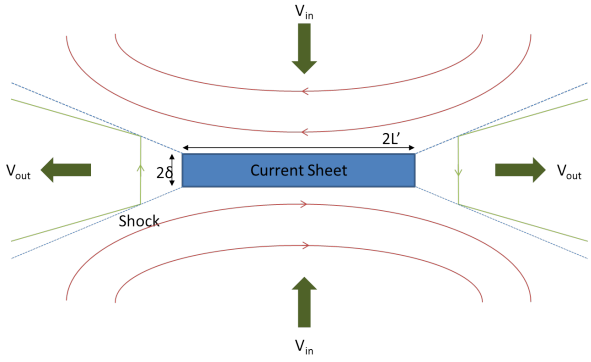

Figure 2.6: A diagram of Petschek reconnection where magnetic field lines are shown in red.

The Petschek model assumes instead of the energy being released in the diffusion region, the energy is released in shock waves travelling outwards, as shown in Figure 2.6. This then allows more plasma to flow into the reconnection region, increasing the reconnection rate. The rate in this model is comparable to the Alfvén velocity, a scenario much more closely matching real situations. However this model, like Sweet-Parker, is not a good description of reconnection events observed, due to lacking accurate detail about the diffusion region. Simulations modelling this type of reconnection find the fields do not reconnect on their own, and the resistivity needs to increase near the outer edges of the current sheet in order to sustain this reconnection [61]. It has been found by Uzdensky that Petschek's theory requires there to be a constraint on the length L', which then means that no increase in reconnection rate from the Sweet-Parker model has been achieved. The exception is when there are large gradients in the resistivity [56, 62].

2.4.3 Hall Reconnection

Hall reconnection is a collisionless process which treats the plasma as two fluids, rather than just one, assuming that $v_e \neq v_i$. In the region close to the reconnection the electrons and ions are handled separately. If the ions have decoupled from the magnetic fields before reaching the current sheet, due to their gyroradius being longer than an electron's, then the magnetic field is only carried by the electrons. The current sheet width, therefore, can be on a much smaller scale than the ions gyroradius. The electron mean free path still needs to be larger than the current

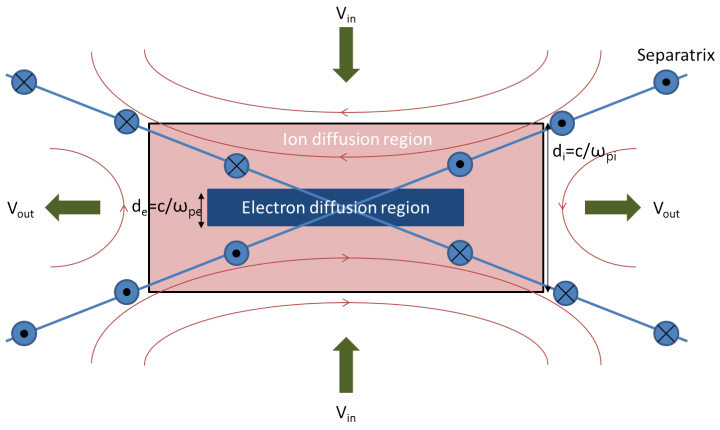

Figure 2.7: A diagram of Hall reconnection with magnetic field lines around the spots in red, and the fields shown along the separatrix region, in blue.

sheet half-width, so allowing the reconnection to be considered collisionless. The electrons flow vertically in the current sheet and are released in the outflow. This in-plane current also generates another magnetic field surrounding it which can be seen along the separatrix region in Figure 2.7

A signature of reconnection that can also appear in Hall reconnection is the ejection of electrons in jets, from the outflow region, carrying with them the energy released in the reconnection process. This reconnection process is much faster than the others mentioned previously and provides better matching to astrophysical and laboratory systems [63, 64].

2.4.4 Nernst Effect and Reconnection

Recent studies of the Nernst effect [65] have shown the importance of considering the Nernst effect in reconnection events. The Nernst effect advects magnetic fields with heat flow, down temperature gradients. Braginskii added further terms to the magnetic field Equation (2.39) to describe the Nernst effect, resulting in Equation (2.58)

$$\frac{\partial B}{\partial t} = \nabla \times \left(\mathbf{v} \times \mathbf{B} - \frac{\mathbf{j} \times \mathbf{B}}{n_e e} + \frac{\nabla p_e}{n_e e} + \frac{\nabla T_e}{e} + \frac{2\mathbf{q_e} \times \mathbf{B}}{5P_e} - \eta \mathbf{j} \right) \tag{2.58}$$

where $\mathbf{v}$ is the bulk flow velocity. The third term on the RHS of Equation 2.58) gives the Biermann battery term, as already seen in Section 2.2, the first term on the RHS gives the frozen-in-flow movement, the second term is the Hall term, the fourth term is the thermoelectric term and the last term on the RHS describes the resistive diffusion. The Nernst term is described by the fifth term on the RHS [47].

The laser creates heat flows that are driven out by advection, travelling at the Nernst velocity, v_N, without electron currents which are required for the Hall effect. The reconnection rate is then on a scale proportional to the heat flow velocity, rather than the Alfvén velocity. Considering the Nernst effect in reconnection would give a semi-collisional model as the hotter electrons are collisionless and the magnetic field is frozen to them. However, there is still a bulk flow of plasma, where colder electrons will help transport the fields and these are considered collisional [48].

The importance of either the Hall or Nernst effect in a reconnection environ-

ment is considered by the comparison of the Hall term, $\mathbf{j} \times \mathbf{B}/en_e$ to the Nernst heat flow, $\mathbf{v_N} \times \mathbf{B}$. The Haines number takes the ratio of these to give

$$H_N = \frac{en_e|v_N|}{|j|} = \frac{1}{5}\kappa_\perp^c \beta \omega_{ce} \tau_{ei} \tag{2.59}$$

2.4.5 Anomalous Resistivity

Anomalous resistivity is when an instability occurs what allows the reconnection rate to increase through anomalous collisions. The reconnection velocity from the Hall reconnection model actually yields the same reconnection velocity as that from anomalous resistivity, apart from the reconnection length is undefined in Hall reconnection. The resistivity instability occurs when the reconnection width is smaller than $\delta < B/\mu_0 J$. The small thickness means there is a large enough pressure created from resistive heating, which eventually expands the current sheet width, until the resistive heating from the instability is reduced sufficiently for it to become stable again. The increasing width of the reconnection width, decreases the Lundquist number and increases the inflow velocity, allowing faster reconnect [66, 67].

2.5 Summary

In summary, this chapter has established some of the relevant theory required for the experiments discussed in this thesis. Understanding the physics that occurs within a laser-plasma interaction and the method via which energy is absorbed from the laser beam is important for helping to interpret data. The Biermann battery mechanism is able to describe how magnetic fields are generated when non-parallel density and temperature gradients exist, both around the laser spot and when an asymmetrical shock is produced. If two laser spots are focussed in close proximity to one another, magnetic reconnection can occur from the opposing fields generated around each spot. There are numerous models that predict a reconnection rate, and some of these will be discussed further in Chapter 5.

Chapter 3

Facilities and Diagnostics

In the past few decades the development of lasers has enabled research to progress rapidly and probe the frontiers of physics knowledge. The lasers are now able to provide peak powers exceeding 1 PW [68]. The high power laser facilities allow research into areas such as ICF, laboratory astrophysics, high energy density regimes and plasma physics. Experimental work detailed in this thesis was conducted using three different laser facilities in the UK and in the USA. This chapter gives a brief overview of each of the facilities, and also about the principal diagnostics used on the experiments.

3.1 Producing Laser Beams

The production of a solid-state laser beam goes through several stages. The laser pulse is initially created in an oscillator. This light contains nanojoules of energy and might be femtoseconds or picoseconds in pulse length. The beam is produced from a material such as as Nd:YAG (neodymium-doped yttrium aluminium garnet) or Nd:glass (neodymium-doped glass), where flash-lamps pump the medium. Pumping is when the atoms in the medium are energised into an excited state and photons passing through cause stimulated emission of the same wavelength and direction as itself. There can be mirrors at either end of the cavity medium which reflect light back through the material, increasing the beam flux further. The wavelength, λ, of the photons is set by the distance between the two mirrors, i.e. $L = \lambda n/2$ where n is a positive integer number and L is the length of the cavity. Some light will finally be

allowed to leak from the optics and provide a low energy beam for the subsequent amplification stages. The leakage of the light from the optics can also be controlled using Q-switching and mode-locking.

Q-switching is a technique that allows shorter, high energy pulses to be created rather than continuous wave beams. This is done by closing the cavity to the beam until maximum population inversion is achieved by the pump lasers, and then when the cavity is opened, the full energy stored will be released in a single pulse. Mode-locking can be used in this situation by locking together modes of the beam that are close in frequency. The lasing material has a bandwidth such that it can only lase within a range of frequencies.

After the beam is created in the oscillator the light used for long (nanosecond) pulses is typically passed through pre-amplifier modules (PAMs). The PAMs contain rod or disc amplifiers pumped by flash-lamps. The PAMs will also shape and smooth the beam by spectral dispersion. Faraday rotators can be used to control the beam passing through the amplifier, and minimise pre-pulses in the beam. To help preserve the optics and prevent damage further along the laser the beam can be stretched. This involves increasing the time of the pulse, as well as also expanding up the beam size, so that the flux decreases. The stretching of the pulse in time is done by adding a 'chirp' to the beam. The chirp is added by a grating pair which will be used to separate the spectral components of the beam in time. This is called chirped pulse amplification (CPA). Optical parametric chirped pulse amplification is a further improvement to CPA, normally used for the shorter pulse lengths to allow even higher intensities and energies. It uses a non-linear crystal which two beams pass through, one as the pump beam to help amplify a second, weaker input signal beam from the oscillator. When the pump beam travels through the crystal its photons are converted into lower-energy photons and 'idler' photons which have an energy equivalent of the difference between the photon energies of the pump and signal beam. After amplification the light is passed through crystals to double or triple the frequency, depending on facility options and user requirements.

The process described here is a generalised method for how laser light is produced. The following facilities will, in principal, use a similar method to create their laser beams to that above, with some stages omitted or differing slightly.

3.2 Vulcan Laser Facility

The Vulcan laser system is situated at the Rutherford Appleton Laboratory and comprises a Nd:glass laser system which splits into 6 long pulse beams (nanoseconds) and two short pulse beams (picoseconds). The laser can be delivered to two separate target areas, although the area used for the experiment discussed in this thesis is Target Area West (TAW) [69]. The long pulses, of duration 0.5-8 ns, can also reach up to intensities of 10^{15} W/cm^2 on target. The long pulses can be used at 1053 nm or frequency doubled to 527 nm.

3.3 Jupiter Laser Facility

The Jupiter laser facility (JLF) is a user facility found on the site of the LLNL, existing alongside the NIF. Over the years different laser systems have been seen to come and go from the facility but currently it consists of several laser systems; Comet, Europa, Janus and Titan. The energy of the Janus laser beams are of up to 1 kJ per beam at a 1.05 μm wavelength. The pulses are on the order of nanosecond durations and can be focussed down to 20 μm spots. The beams are labelled West and East, and both are able to be frequency doubled.

3.4 Orion Laser Facility, AWE

Orion first started operations in 2010 [70] and its first academic experiment took place in 2013. The Orion facility houses 2 short pulse beams and 10 long pulses. The 2 short pulse beams are used to deliver 250 J of infra-red light per beam in 0.5 ps and 10 long pulse beams can deliver up to 500 J of ultra-violet light in 0.5-5 ns. This allows Orion to deliver up to 5 kJ using the long pulse beams.

The target chamber at Orion is a 4 m internal diameter sphere constructed from aluminium alloy. The 10 long pulse beams are fed in as two cones at 50° to the principal and horizontal axis. The set-up of Orion allows for flexibility in which beams can be used during an experiment, as seen in Chapter 5. The short pulse beams enter the chamber above the horizontal plane and are then focussed along the horizontal axis, using parabolas.

There are permanent diagnostics around the chamber, as well as diagnostics that can be inserted into the chamber using ten-inch manipulators (TIMs). These TIMs are used to reduce the need for pumping the chamber each time a new diagnostic is inserted and to allow for a more efficient collection of data [72, 71]. The design of the chamber and the availability of high intensity lasers was an attractive feature for this experiment, although also one which helped mould the final designs.

3.5 Proton Radiography

3.5.1 Target Normal Sheath Acceleration

High intensity lasers ($\geq 10^{18}$ W/cm^2) can be used to produce beams of protons for the imaging of magnetic and electric fields [73], proton ignition [74] for the fast ignition fusion effort and in medical applications such as cancer treatments [75] where proton beams could be used to kill cancer tumours in localised areas. The protons can be produced via several methods [76, 77], although the method used in this thesis was that of target normal sheath acceleration (TNSA) [78, 79, 80, 81] which is a widely researched ion acceleration mechanism [82]. The protons produced from targets in this manner are an ideal probe of fields, due to their reproducibility of a uniform beam quality, good spatial and, potentially, temporal resolution as well as high peak proton energies which limits scattering.

TNSA occurs when an intense laser hits a solid target and electrons near the surface absorb the laser energy. The electrons are accelerated away from the target

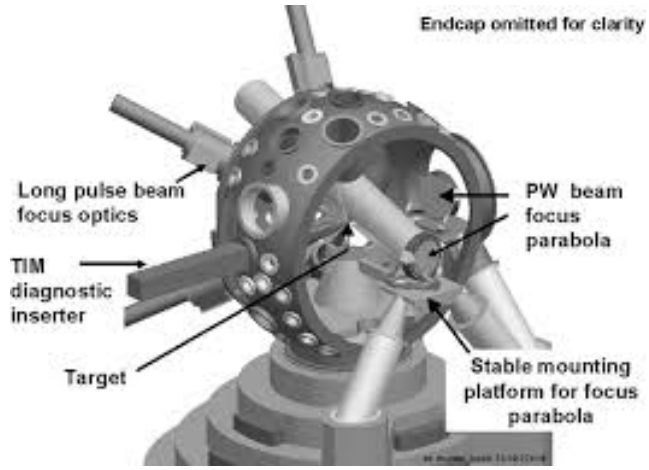

Figure 3.1: A image of the Orion target chamber [71].

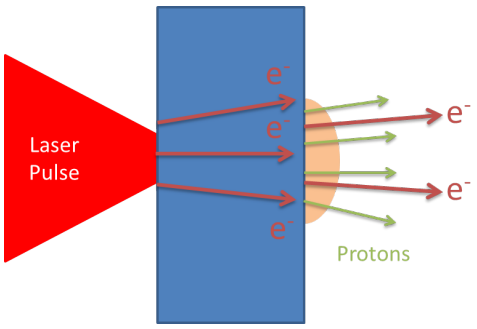

Figure 3.2: A diagram of target normal sheath acceleration where protons are accelerated from the rear side of a target following the sheath field set-up by the escaping electrons.

surface, in the direction of the original laser propagation until they leave the rear side of the target. However, there are heavy ions left in the target which do not respond as quickly as the electrons and so a depleted, positively charged region near the target rear surface sets up an electric field normal to the target, a sheath field. The ions within the Debye length are accelerated by the sheath field, and also leave the rear surface of the target, as shown in Figure 3.2. However the accelerating field is not homogeneous for all ions. The ions which are accelerated from further into the target have been slightly shielded from the sheath field by other ions in front and have a smaller acceleration. The lighter ions from the hydrocarbon contaminates, normally present on the surface of the targets, make up the majority of the beam. The hydrogen atoms ionise first and react quicker to the accelerating fields than other ions due to the charge to mass ratio. The proton beam usually has a half divergence angle of between 10-15° from a small virtual source, producing a laminar beam with protons of up to energies of 60 MeV [82]. The proton target, for Chapter 5, is a 25 μm thick, 3 mm diameter, gold foil. Normally there is a preference for producing protons from larger diameter targets to try to reduce fringe field effects from the edges, but due to spatial constraints within the Orion chamber the diameter needed to reduced for our experiment. The thickness of the proton target also affects the quality of the beam and it was found this thickness was optimum for producing a uniform beam, whilst maintaining high proton fluxes.

3.5.2 Proton Detection

The protons used in the radiography of an interaction are collected using radiochromic film (RCF), which is suitable for high dose measurements and more typically used

in medical applications. RCF is a plastic film made up of several layers depending on the type and sensitivity of the film. There are two types of RCF used in the experiments in this thesis, GAFCHROMIC©HD810 and EBT3. Different types of films are used, to improve the sensitivity or to make certain features clearer in the images produced. Diagrams of the layers that are contained within these types of RCF are shown in Figure 3.3.

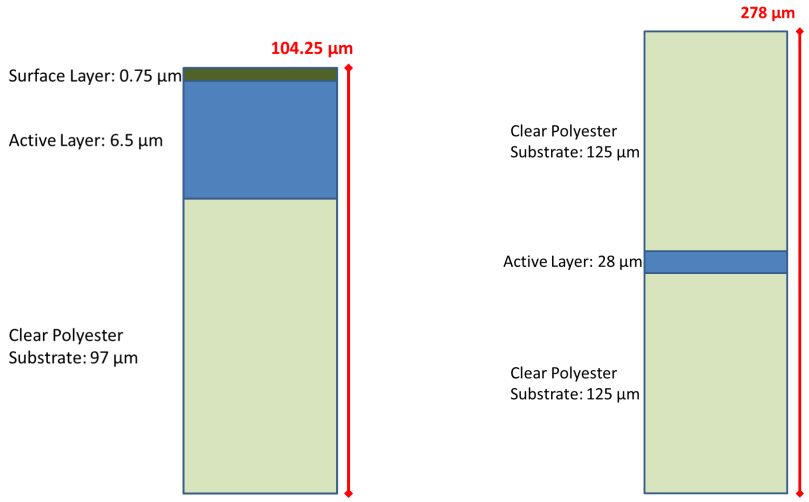

(a) HD810 RCF layers **(b)** EBT3 RCF layers

Figure 3.3: Diagrams of the layers within a piece of RCF. The active layer is the layer which contains the dye that turns colour when a proton deposits energy.

The active layer of the films contains a dye which when protons and heavy ions are incident on changes colour, normally to blue, due to photo-chemical reactions. The wider the active layer region, the more sensitive the film and the wider the range of proton energies it will record details from. The film will turn darker in colour the more irradiation it receives. The RCF is also sensitive to radiation such as gamma rays and electrons however, due to the shorter stopping range of protons it is mainly just these which affect the dye in the layers. The RCF stack is also always wrapped in thin, ~ 12 µm, aluminium foil to stop some heavier ions, soft X-rays and optical light reaching the film. Optical light has no short-term influence on the colouration of the film, making this a very useful diagnostic. The films are spaced with iron, gold and tantalum to help filter the different proton energies as well.

The approximate set-up and parameters for proton radiography are shown in Figure 3.4, where protons are produced from a foil by a short pulse laser and can then be passed through a grid, which imprints a pattern on to the beam. The

protons then pass through the interaction's fields, before being recorded at the RCF. There might also be a filter foil used after the proton foil target to help shield both the proton and main interaction target from unwanted debris or laser light. The filter foil used in the experiment in Chapter 5 was a 2 μm gold foil, thin enough to not scatter the protons but thick enough to protect the targets.

Protons with different energies and velocities can be produced from thin gold targets via the TNSA mechanism, as described previously. These different velocities result in the protons probing an interaction at different times, giving time resolution to this diagnostic. The time-of-flight (TOF) of the protons is

$$TOF = l\sqrt{\frac{m_p}{2E_p}} \tag{3.1}$$

where l is the distance travelled by the proton from the target it is produced at, to the layer of RCF that it reaches, m_p is the mass of the proton and E_p is the energy of the proton. The lower energy protons that will be probing at the later times are also more sensitive to scattering and may saturate the RCF if produced with large fluences.

The magnification, M, of the main target is given in Equation (3.2), although the distance to the RCF will change by a small amount, depending on the layer of the RCF being analysed and the thickness of the stack in front.

$$M = \frac{L + l}{L} \tag{3.2}$$

where L is the distance from the interaction to the RCF and l is the distance from the proton producing foil to the interaction. The energy and stopping distance of a proton is given from the Bethe stopping power equation. The energy lost

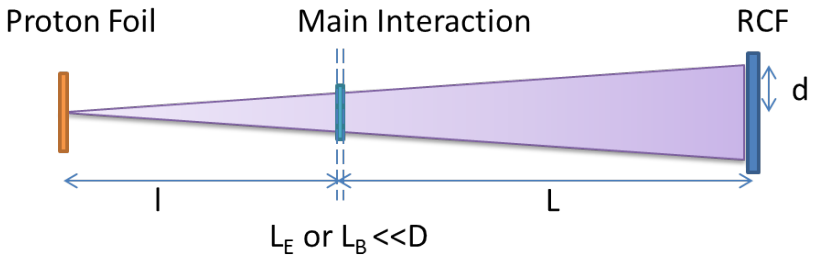

Figure 3.4: A diagram of the different distances used in calculating various proton probing parameters.

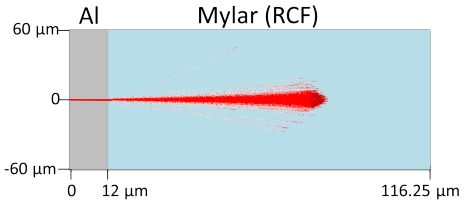

(a) Paths taken through Al and RCF for 1 MeV protons, as calculated using SRIM [83].

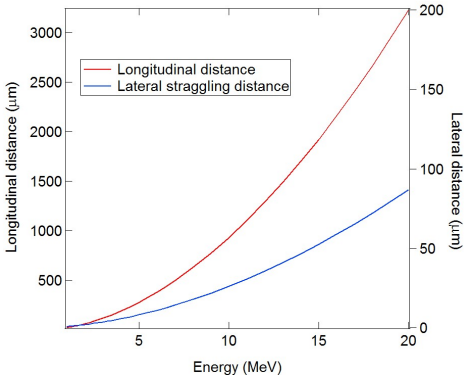

(b) A graph of the longitudinal and lateral distances travelled through RCF by protons of various energies.

Figure 3.5: An image and graph displaying the average longitudinal and lateral distances the protons travel through Al and RCF layers.

by the proton increases as its velocity decreases. They will deposit most of their energy in a Bragg peak [84]. If the proton's Bragg peak coincides with the active layer on the film then the proton of that energy is recorded. As the protons travel through the RCF stack and filter materials they will scatter. This is known as lateral straggling. There are some materials which will scatter the protons more than others or become activated, so filter materials chosen to go between RCF layers are carefully selected. Figure 3.5 shows the output from a simulation run using 'Stopping Range In Matter' (SRIM) [83], demonstrating the straggling of a proton through an RCF layer. Simulations are used to show where the Bragg peak of protons of different energies will occur. By building the RCF stack, the energies and scattering of each layer can be calculated, and an example stack is shown in Table 3.1.

3.5.3 Proton Deflections

Protons probing the electric and magnetic fields are subject to deflections, due to the Lorentz force as shown in Equation (3.3).

$$\mathbf{F} = q(\mathbf{E} + \mathbf{v} \times \mathbf{B}) \tag{3.3}$$

where $\mathbf{E}$ is the electric field, $\mathbf{B}$ is the magnetic field, q is the charge of the proton and $\mathbf{v}$ is the velocity of the proton. Probing a laser-plasma interaction with protons is designed so that the protons pass either perpendicular or parallel to the target's surface and predominantly subjected to magnetic fields or electric fields.

When the protons are displaced by the magnetic fields the deflection amount is proportional to the cross product of the magnetic field's magnitude and the proton's velocity. The amount the proton is deflected is described by Equation (3.4), calculated from the Lorentz force assuming that the length the field is experienced over, L_B, is much smaller than the distance from the interaction to the RCF, L,

$$B.L_B = \frac{d}{qL}\sqrt{2m_pE_p} \tag{3.4}$$

where d is the deflection at the RCF from the proton's original end position without deflection, L is the distance from the interaction to the RCF, E_p is the proton energy and L_B is the length over which the magnetic field, B, is experienced. This is also shown by Figure 3.4. Measuring this deflection from layer to layer of RCF, i.e. different energies of protons, will also verify whether it is a deflection from the electric or magnetic fields. The electric field deflection is given by Equation (3.5),

Layer Number	Layer Material	Thickness (μm)	Energy (MeV)	Time (ps)
	Al	12		
1	HD810	104.25	0.9	381
2	HD810	104.25	3.1	205
	Fe	50		
3	HD810	104.25	6.1	146
4	EBT3	280	8	128
	Fe	50		
5	HD810	104.25	10.1	114
6	EBT3	280	11.5	106
	Fe	250		
7	HD810	104.25	16.4	89
8	EBT3	280	17.4	87
	Fe	250		
9	HD810	104.25	21.2	78
10	EBT3	280	22.2	77
	Fe	500		
11	HD810	104.25	28	68
12	EBT3	280	28.5	68
	Fe	625		
13	HD810	104.25	34.5	61
14	EBT3	280	35.1	61

Table 3.1: A table of a RCF stack composition used in the reconnection experiment. The peak energies stopped within each layer have been calculated using SRIM [83] and the time of flights for the protons relevant to each layer are shown.

$$E.L_E = \frac{2dE_p}{qL} \tag{3.5}$$

where L_E is the length over which the electric field, E, is experienced, d is the deflection amount on the RCF from the proton's original position and L is the distance from the RCF to the interaction. If the deflection is due to the electric fields, there will be a deflection proportional to the proton energy by E_p^{-1} rather than a deflection proportional to $E_p^{-1/2}$ which is the case for a magnetic field.

The resolution of the protons is worked out from resolving the smallest known object in the experiment, which, in our experiment, are the grid lines seen clearly in the RCF images. The grid used on this experiment had 600 lines per inch (LPI) with gold wires 7.6±0.1 μm thick at a spacing of 34.2±0.1 μm. An image with a corresponding lineout is seen in Figure 3.6.

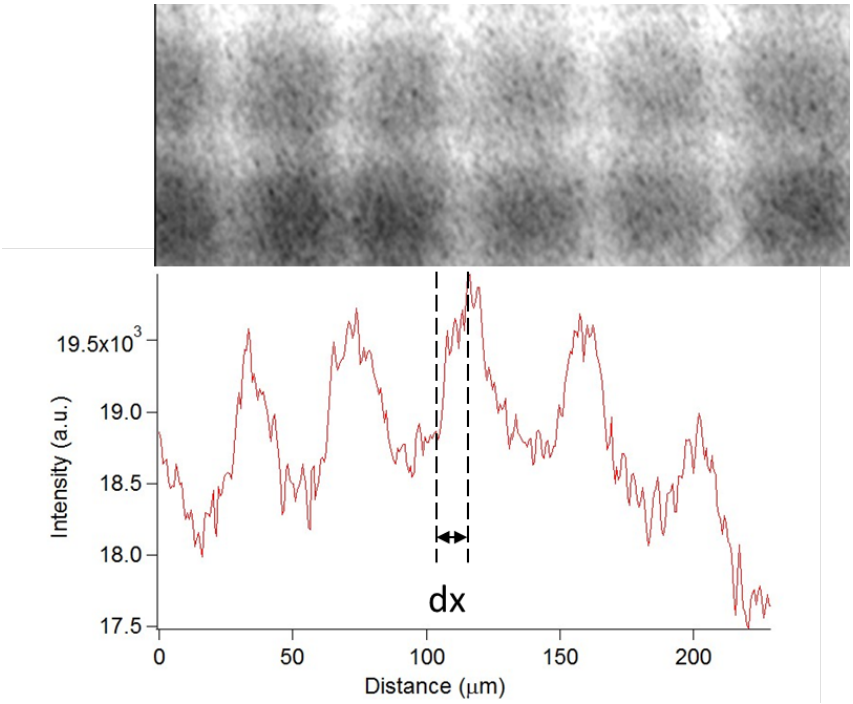

Figure 3.6: An image of a grid recorded by the RCF by 17.4 MeV protons and the corresponding lineout taken across its width. The length, dx, is twice the minimum resolution of the proton radiography.

The resolution measured from the RCF at target chamber centre, with a factor two magnification from the grid to TCC, is 8.3 μm. This resolution is limited by the RCF scan resolution. The protons of higher energy also normally produce better resolution than lower energies due to less scattering. Protons produced in this manner are more commonly calculated as having a virtual source size of approximately

3-5 μm which is a point that the proton beam can be extrapolated back to as its virtual origin. [85, 86].

3.6 Spectroscopy

Spectroscopy is the measurement of the radiation intensity at a range of wavelengths and energies. The different formations and shapes of the spectral lines lead to inferences about the temperature and density of a substance. Direct measurements of these properties might not often be possible, therefore, this indirect technique is a very useful method. The spectra that occurs from a plasma is due to emission and absorption of photons at energies which corresponds to the transition energies within atoms.

There are also free electrons within the plasma that can recombine with ions, or the free electrons might collide with ions and produce bremsstrahlung photons, which will also contribute to a spectrum. The use of atomic models is crucial to being able to interpret the data, so modelling programmes, such as PrismSpect and Spect3D [87], are used to reconstruct the spectra that might be produced in an experiment.

3.6.1 Orion Crystal Spectrometer

The experiment at the Orion laser facility used an X-ray spectrometer specifically designed for the purpose of measuring temperatures across two focal spots, in a magnetic reconnection geometry. This spectrometer fits onto the front of a gated X-ray detector (GXD) enabling the recording of 1D spatial and temporal information.

A GXD camera consists of four stripline micro-channel plates (MCPs) attached to a CCD, and is suitable for inserting into the chamber via a TIM. The CCDs are SI-1000 cameras, from Spectral Instruments, and record the output from the MCP. The MCP is made up of chrome strips then copper topped with 1000 Å of gold. Each pixel on the CCD is 9×9 μm and they are in an array of 4200×4200 pixels [88]. The four channels of the GXD could be separated out in time, taking a 210 ps sweep across each channel.

On the front of the spectrometer were four slits of 0.02×8 mm to allow light to

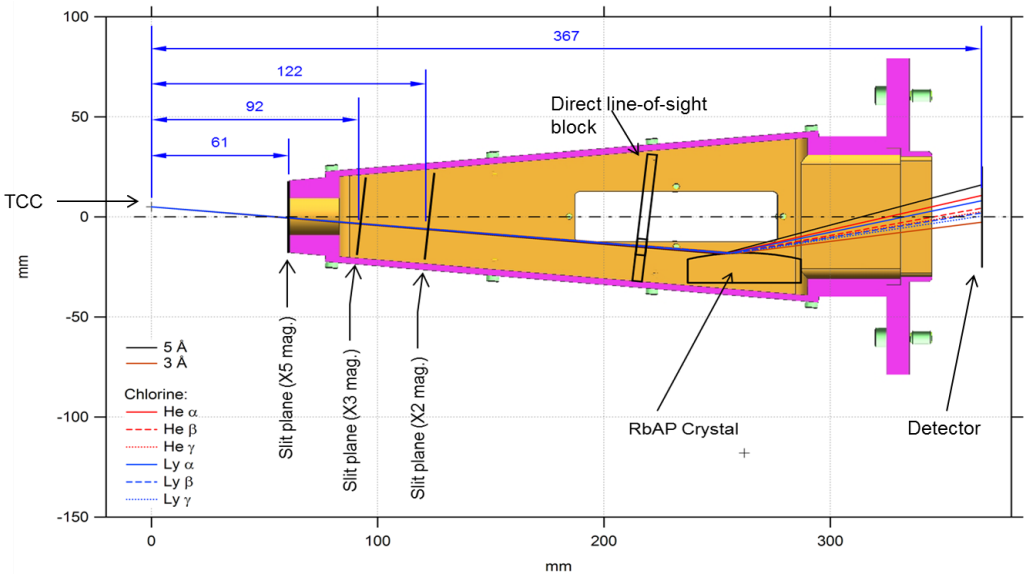

Figure 3.7: A diagram of the spectrometer used in the experiment, with the relevant parameters, and different locations for the front entrance slits for various magnifications [89].

fall onto each of the four channels of the GXD, where the temporal sweep direction matched with the spectral dispersion axis. The magnification of the spectrometer was either 2, 3 or 5, which was achieved by allowing the front slits to be placed in an appropriate location for the magnification, as shown in Figure 3.7. The design of the spectrometer allowed the magnification to be changed easily so that if the larger magnifications resulted in some spectral lines mirroring onto other strips the magnification could be reduced. However this was not an issue and so the majority of the data collected was using a magnification of 5.

The spectrometer used a cylindrically convex RbAP crystal (2d=26.121 Å) with a radius of curvature r=100 mm. A convex crystal has the advantage of being able to increase the spectral range of the detector as it can accept a wider range of Bragg angles, θ_B. The body and dimensions of the spectrometer are shown in Figure 3.7. The Bragg angle is given by

$$n\lambda = 2d\sin(\theta_B) \tag{3.6}$$

where n is the order of the interference, λ is the wavelength, d is the spacing between the diffracting planes of the crystal and θ is the Bragg angle. The dimensions of the spectrometer, δ, s, r, θ, h, L_S, L_D and α, are shown in Figure 3.8 and used with the following set of equations [90, 91]

$$\delta = \tan^{-1}\left(\frac{s - r.\cos\theta}{h - r.\sin\theta}\right) \tag{3.7}$$

$$\theta_B = \delta + \theta L_S = \frac{(h - r.\sin\theta)}{\cos\delta} \tag{3.8}$$

$$L_D = \frac{(f - r.\sin\theta)}{\sin 2\theta + \delta} \tag{3.9}$$

These equations are used to calculate where each wavelength will fall on the crystal. The dimensions for the experiment at Orion were s=-82.3 mm, h=277.5 mm, f=158.0 mm and α=48.3°.

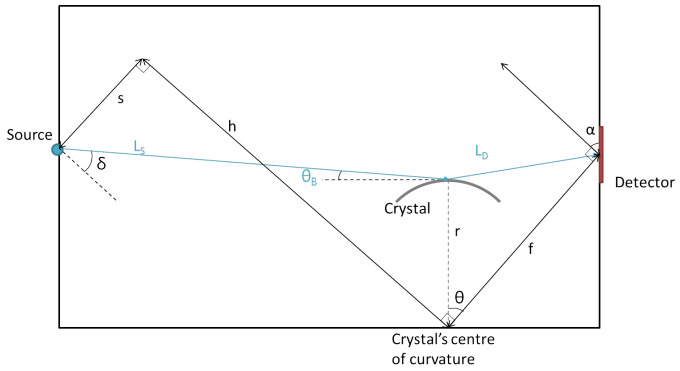

Figure 3.8: The layout of the spectrometer's crystal in relation to the detector and source as well as parameters required from the geometry.

The dispersion of the spectrometer is worked out using Equations (3.6)-(3.9). The dispersion is a measure of the energy per distance unit (e.g. eV/mm) on the camera,

$$\frac{d\lambda}{dX} = \frac{d\lambda}{d\theta}\frac{d\theta}{dX} = \frac{2d}{n}\cos\theta\frac{d\theta}{dX} \tag{3.10}$$

where X is the distance on the detector. $\frac{d\theta}{dX}$ can be calculated using a MATLAB script written to calculate the dispersion directly. The dispersion of this spectrometer is shown in Figure 3.9.

The pixel number was then converted to energy using a fit to the calculated dispersion. Checking known spectral line positions, as given in Table 3.2 for chlorine, on the detector also confirmed the conversion was correct.

3.6.2 Filtering of the Spectrometer

The spectrometer needed corrections applied to the intensity of wavelengths recorded due to the spectral sensitivity of the various components. There were also corrections due to the collection effects, such the energy range and solid angle intercepted by

Transition	Wavelength (eV)	Spectral line
	2622	K-α
1s2p-1s^2	2791	He-α
1s-2p	2963	Ly-α
1s3p-1s^2	3272	He-β
1s4p-1s^2	3441	He-γ
3p-1s	3508	Ly-β
4p-1s	3699	Ly-γ

Table 3.2: A table of spectral lines observed from Chlorine.

the pixels on the GXD.

Spectral sensitivity corrections are applied to the recorded signals to calculate the signal at the source. The gold photocathode of the GXD, crystal response and beryllium filter contributed to this correction. The photocathode spectral response is taken to be that of gold and is documented in Fraser *et al* [92], as shown in Figure 3.10. The angle of incidence of the light on the photocathode is also taken into account, by applying a scaling factor of cosec(θ) to the response curve given in the publication, where θ is the angle of incidence.

The filter response of the 25 μm thick Beryllium and crystal reflectivity are taken from work on X-ray interactions by Henke *et al* [93]. These are fairly constant across the X-ray wavelengths of interest in this experiment. The energy per pixel

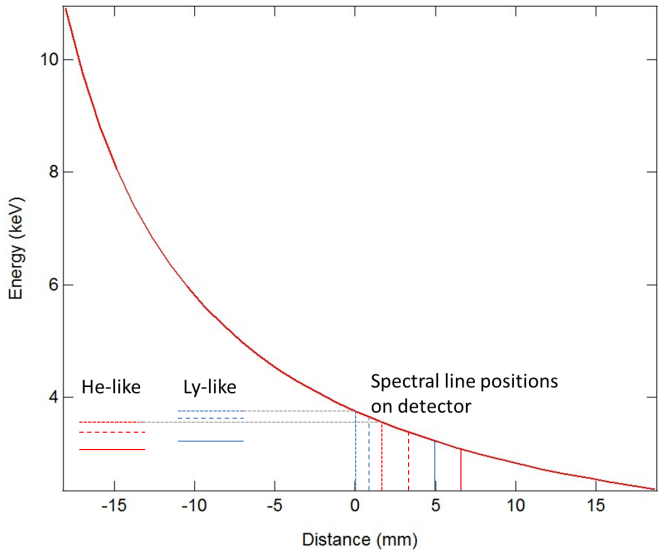

Figure 3.9: A graph showing the dispersion curve for the spectrometer used at Orion. Lines are shown for the He-like and Ly-like chlorine emission lines observed and where these will fall on the detector.

and solid angle intercepted per pixel is also corrected for, as the dispersion curve demonstrates that some pixels will intercept a wider range of energies than others.

The spectrometer will have corrections made due to all of these above mentioned effects. The photocathode response is the one which will have the largest effect on the intensities recorded, due to the widest variation over the spectral range.

3.6.3 Calculating a Temperature

Temperatures of a plasma can be calculated from the recorded spectral lines. Individual spectral lines can be identified depending on their position on the detector. Then one of two methods can be used to extract the temperature. The first method is to calculate line ratios. Pairs of integrated line intensities can be divided to give a ratio, R, described by Equation (3.11).

$$R = \frac{i_1}{i_2} = \frac{\omega_1 A_1 g_1}{\omega_2 A_2 g_2} \exp\left(-\frac{E_1 - E_2}{k_B T}\right) \tag{3.11}$$

where A is the relationship between the transition probabilities and oscillator strengths, ω is the line frequency, E is the energy level and g is the statistical weight for the energy states [94, 95]. Rearranging Equation (3.11) to give Equation (3.12) leads to a temperature measurement.

$$k_B T = \frac{E_2 - E_1}{\ln(\omega_2 g_2 A_2 R / \omega_1 g_1 A_1)} \tag{3.12}$$

However, this calculation will assume that the excited states of the two lines measured are both pumped by similar processes. This means that the ratio of emission only depends on the absolute number of ions of each type and their transition

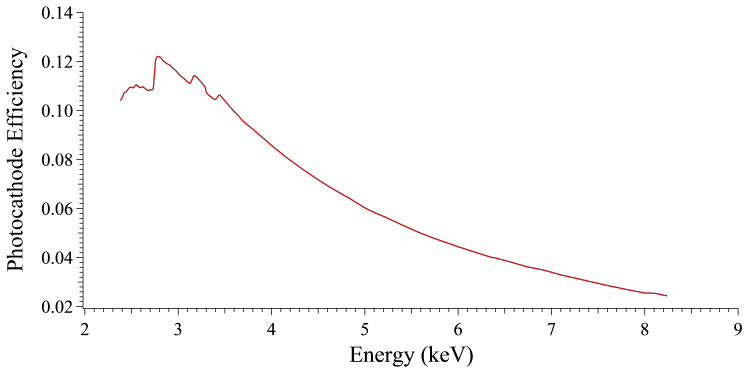

Figure 3.10: A graph of the photocathode spectral response for the GXD [92].

probability, A. The two lines also need to be optically thin, so that effects due to properties such as density do not need to be considered, which can make the calculation more complex. In the experiment explained in Chapter 5 there is an optically thick plasma and the line ratios gave unphysical results. Instead, a second method of fitting to the continuum emission is completed, where the emission is optically thin. The continuum is fitted to using Equation (3.13)

$$I = I_0 + A \exp\left(\frac{-(E - E_0)}{k_B T_e}\right) \tag{3.13}$$

where I_0 and A are constants, E and E_0 are energies and offsets in energies of the emission, and T_e is the electron temperature [95].

3.7 Thomson Scattering

Another diagnostic that can be used to measure temperature, as well as a spectrometer, is Thomson scattering. This was used at the Janus laser, where the West beam's laser light was scattered from a plasma due to interactions with the electrons. Collective scattering is when the laser light is reflected from thermal fluctuations of electrons and the light is Doppler shifted due to the phase of the thermal plasma wave. The shifts in wavelength and shape of the scattered light's spectra is then used to measure the temperature and density of the electrons and ions at the point which the laser beam scatters from.

The scattered wave vector and frequency ($\mathbf{k_s}$ and ω_s) are dependent on the wave vector and frequency of both the incoming laser beam ($\mathbf{k_i}$ and ω_i) and the electron oscillations causing the scattering ($\mathbf{k}$ and ω). Additionally, if the electrons have a spread in their velocities, v_e, then the scattered light will be broadened as well as Doppler shifted.

$$\omega = \omega_i + \mathbf{v_e}(\mathbf{k_s} - \mathbf{k_i}) \tag{3.14}$$

$$k = k_s - k_i \tag{3.15}$$

The form factor of the resulting spectrum is given by Equation 3.16

$$s(\mathbf{k}, \omega) = \frac{2\pi}{k n_e}\left[\left|1 - \frac{\chi_{eL}}{\epsilon_L}\right|^2 \frac{k}{k_\parallel} f_{e\parallel}\left(\frac{\omega}{k_\parallel}\right) + \left|\frac{\chi_{eL}}{\epsilon_L}\right|^2 \sum_i Z_i^2 f_{ik}\left(\frac{\omega}{k}\right)\right] \tag{3.16}$$

where $\epsilon_L = 1 + \chi_e + \chi_i$ is the dielectric function, χ_e and χ_i are the susceptibilities, i is the different number of ion species to be summed over, Z is the ion charge, f_e is the electron distribution and f_i is the ion distribution [96]. This equation is fitted to the shape of the spectrum resulting from the Thomson scattering signals and the density and temperature of the plasma are extracted. The scattering results in shifts from both the electron plasma wave (EPW) and the ion acoustic wave (IAW). The electron temperature and density can be the calculated using the shape and separation of the blue and red shifted peaks that occur in the EPW features, as seen by Equation (3.17),

$$\frac{\Delta\lambda_{EPW}}{\lambda_0} \approx 2\left[\frac{n_e}{n_{cr}} + 6\left(\frac{v_{th}}{c}\right)^2\right]^{1/2}\left(1 + \frac{3}{2}\frac{n_e}{n_{cr}}\right) \tag{3.17}$$

for scattering angles of 90°and $n_e/n_{cr} \leq 0.05$. The IAW features can be fitted using Equation (3.18)

$$\frac{\Delta\lambda_{IAW}}{\lambda_0} \approx \frac{4}{c}\sin(\frac{\theta}{2})\sqrt{\frac{k_B T_e}{m_i}\left(\frac{Z}{1 + k^2\lambda_D^2} + \gamma\frac{T_i}{T_e}\right)} \tag{3.18}$$

where θ is the scattering angle and γ is the specific heat ratio [97, 98].

3.8 Summary

There have been several different facilities and diagnostics discussed in this chapter. Proton radiography and an X-ray spectrometer were both used in an experiment described in Chapter 5 which was conducted at the Orion laser facility. Measurements of the magnetic and electric fields along with temperatures of the plasma will be calculated from these results. Thomson scattering is a diagnostic used at the Janus laser facility, and discussed in Chapter 6.

Chapter 4

Laboratory Produced Blast Waves

4.1 Introduction

Asymmetric blast waves are of interest in the generation of magnetic fields. Their existence in SNRs gives a potential mechanism for creating magnetic fields within the interstellar medium. The asymmetric shape of these blast waves means that the pressure and temperature gradients across them are non-parallel, allowing the Biermann battery mechanism to seed magnetic fields.

The experiment described in this chapter was conducted at the RAL using the Vulcan laser and the primary results presented are those from a fast framing camera. This camera captured multiple images of the self-emission of the plasma and, from the images, the evolution of the blast wave can be observed. An ellipse is fitted to the asymmetric emission front and the ratio of the major to minor axis is used to describe the shape. When using carbon rod targets the blast wave tends to become more symmetric with time, due to the production of two shocks from the target. Other targets such as plastic spheres and aluminium foils also show the two shocks travelling quite independently of each other, confirming that it is not just a single shock being produced in the interaction.

The chapter is organised such that, firstly, a brief overview is given of the experiments already conducted in this area and some of their results described. Then the set-up of the experiment is discussed. Results are shown from different types

of targets. Aluminium foils and plastic sphere targets show the production of jet- and shock- like features. The results from carbon rod targets produce smooth, near hemispherical emission fronts. These allow for matching a Sedov-Taylor solution to different projection angles along the emission front. From this Sedov-Taylor fit the amount of energy coupled in to the blast wave is calculated. Simulations from a hydrodynamic code, Helios, are also presented and compared with experimental results. The differences arising in the evolution at different projection angles is also further investigated by fitting an ellipse to the front and measuring the change in the asymmetry with time. The measurements made from the schlieren and interferometry images differ from those of the fast framing camera. However, using simulations from a 2D hydrocode, FLASH, these differences are explained. There is then a brief discussion as to how the two shocks are produced from the targets. The chapter summarises with key conclusions, as well as suggestions for further work.

4.2 Previous Work and Motivation

Blast waves produced in the universe and within the laboratory can follow a specific evolution which has been documented by several researchers [99, 100, 101, 50, 102, 103]. They start expanding in a ballistic phase and progress through further stages, as explained in Section 2.3.1.

Initial experiments, such as those by Grun *et al.* [21], demonstrated, when a high energy laser was incident onto a polystyrene foil, that a blast wave could be produced from the expansion of the ablated plasma into a nitrogen or xenon background gas. Schlieren imaging and optical emission were used to record the evolution of the blast wave. This evolution closely followed a Sedov-Taylor [22, 24] solution. Grun noted the blast waves produced in nitrogen were more stable and with smoother profiles than those observed in xenon. It was assumed there was an instability in xenon which perturbed the blast front, potentially due to anti-parallel thermal and ram pressures. These are of great interest and Grun's results showed the amplitudes of these grew with time.

Further work, building on the experiment by Grun, was done by several scientists [102, 101, 104] including Gregori *et al.* [50] and Meinecke *et al.* [20]. Gregori

was able to explain the instability Grun had observed, in more detail, as well as the relevance of this instability in seeding and amplifying magnetic fields. Gregori was able to show that the turbulent processes amplify the magnetic fields. The experiment used a carbon rod target and focussed laser beams of energies >700 J in 1.5-2 ns onto it, producing a blast wave from the rear side of the target. The blast wave was diagnosed using an optical probe beam with interferometry and shadowgraphy. Optical spectrometers were also used to infer temperatures and densities of the plasma and an induction (B-dot) probe enabled the measurement of magnetic fields. This experimental set-up has been used in many experiments [50, 20] and Meinecke *et al.* [20] continued on this work. An argon background gas was used to produce slower blast waves in different densities of gas. The magnetic fields produced were also further amplified by using grids to disturb the shock front and seed turbulent structures within the flow. This chapter will describe one aspect of an experiment designed to follow on from this earlier work.

4.3 The Experiment

This experiment was carried out using the Vulcan laser, TAW. The 6 laser beams at 1054 nm of square 2 ns duration, with a total energy of 1.4 kJ, were clustered into a single, 300 μm focal spot using phase plates, on to various targets including a 500 μm carbon rod, a 10 μm thick aluminium target and a 2 mm diameter, hollow, plastic sphere. The lasers entered the target chamber on an arc, in sets of 3 pairs, at ±25° and 0° to the horizontal axis. The target was enclosed in a chamber containing background gas of argon, at pressures between 0.7-2.6 mbar. A schematic of the set-up is shown in Figure 4.1. The interaction of the laser with the target creates an intense radiation source which ionises the background gas. A rapidly expanding ablation plasma pushes on the ionised background gas, eventually evolving into a blast wave. Diagnostics used in this experiment included an optical spectrometer, interferometry, schlieren imaging and a B-dot probe, as well as a fast framing camera. The main results presented in this chapter are those from the fast framing camera.

The schlieren and interferometry lines used an optical probe beam, produced from a Nd:YAG laser at 2ω (532 nm), with a pulse duration of 4 ns. The B-dot

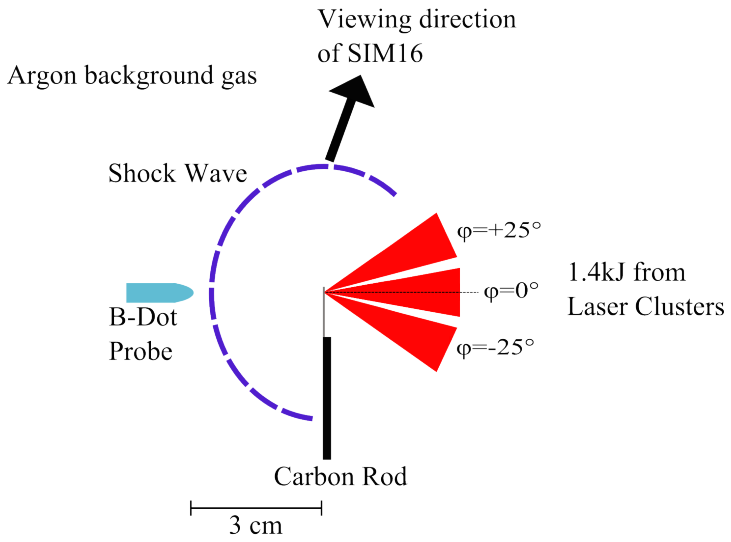

Figure 4.1: A schematic of the set-up for this experiment to measure the magnetic field across a blast wave. The 6 infra-red beams were focused in pairs in to single spot on a target. This drove a blast wave which propagated out towards a B-dot probe.

probes were situated between 1-3 cm from the target, directly opposite the incoming laser. They measured the magnetic field produced across the shock front from the voltages induced in the probe.

4.3.1 Optical Probe Setup

The experiment used two cameras with an optical probe to capture interferometry and shadowgraphy images. The data collected from these cameras on the blast wave can also be compared to the fast framing images. The optical probe was set-up using a Mach-Zehnder interferometry system, as shown in Figure 4.2.

The schlieren imaging used a knife edge as a schlieren stop. The Mach-Zehnder interferometer uses two beam paths, one which travels through the interaction and a second reference beam, to measure densities and temperatures. The beam travelling through the interaction can be refracted within the plasma, altering the phase of the beam. When the two beams are recombined they create interference patterns. Shifts occur in the interference lines where refraction has occurred. The amount of refraction and shift in the light's phase leads to information about the line-integrated plasma density. The cameras were operated with a single 4 ns exposure on each shot so did not yield as much data, for comparison of the blast wave progression, as the fast framing camera. However, the fast framing images have allowed us to confirm that the blast waves produced under similar conditions are generally repeatable and,

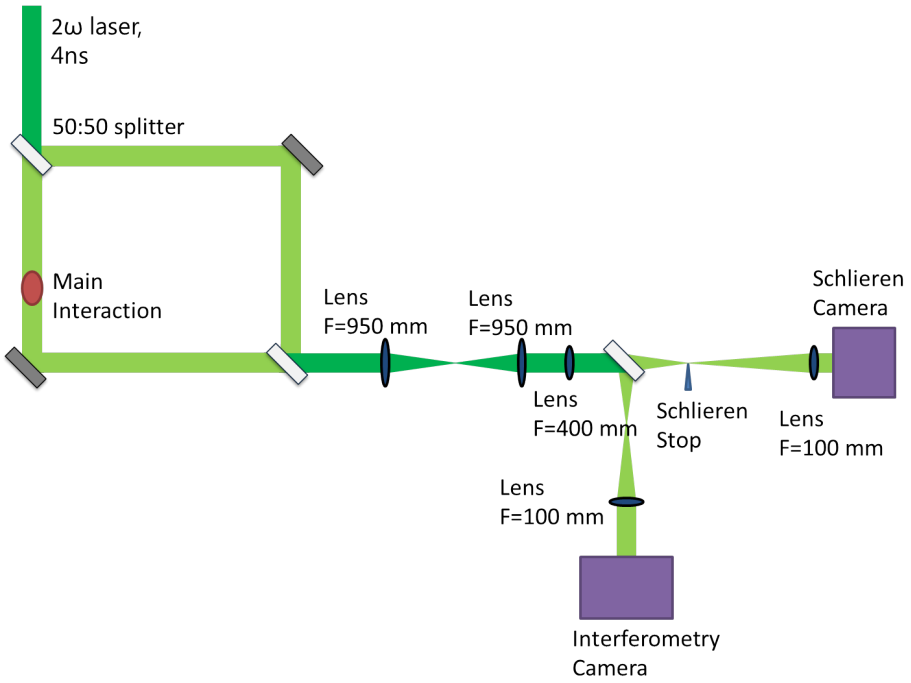

Figure 4.2: Setup of the interferometry and schlieren imaging using a Mach-Zehnder interferometer.

therefore, the individual shot images from the optical probe can be plotted together.

4.3.2 Imaging of the Optical Emission

A fast framing camera captures the optical emission from the interaction. Understanding of the blast wave dynamics on a single shot aids immediate assessment of the shot during an experimental campaign and enables the study of the dynamical evolution of the fluid from measurements of blast wave shapes and structures [105]. The multiple, fast framing camera measurements along a single line of sight are well suited to many laboratory astrophysics experiments where the phenomena of interest occur on hundreds of ns timescales. In this experiment, images were taken using a specialised imaging (SIM16) camera [106], which uses framing speeds of up to 200,000,000 frames per second. The camera contains 16 CCD detectors coupled to micro-channel plates fitted with a S25 photocathode.

The camera is used with filters to reduce the amount of light on the CCD, restricting the light collected to a selected spectral range. The filters used were a 0.8 neutral density filter reducing the overall emission by 85%, a 620 nm filter with a full width at half maximum (FWHM) of ±10 nm, reducing emission by 55% in the operating range of the filter and close to 0% outside of this, and the MCP and

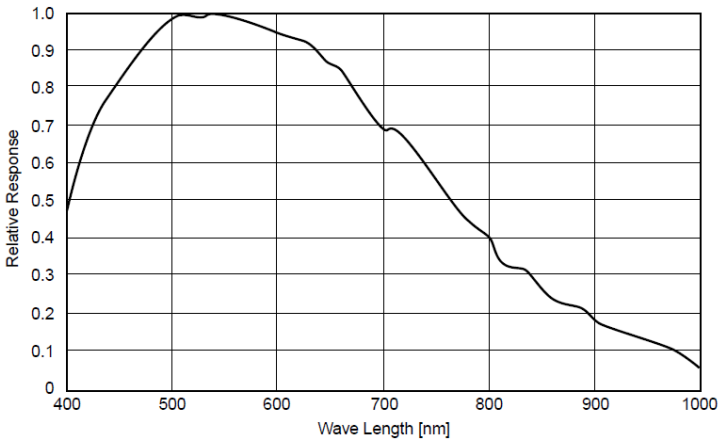

Figure 4.3: Spectral response of the SIM16 camera's MCP and photocathode, not taking into account additional filtering before the camera [107].

photocathode, with a spectral response as seen in Figure 4.3. This leads to an overall transmission of 12% between 610-630 nm and 0% transmission outside of this region. Therefore, the emission recorded by the fast framing camera is primarily from the Ar I and Ar II lines with potentially lines from some target material as well.

The images were taken using the set-up of optics shown in Figure 4.4.

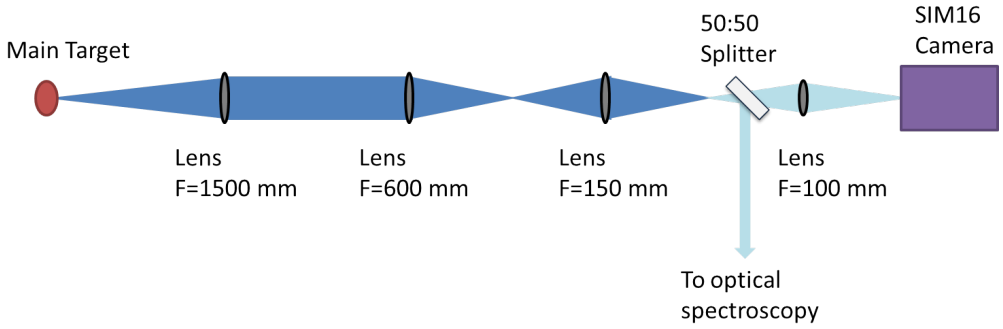

Figure 4.4: Optical set-up of the lenses for the SIM16 imaging.

The images recorded are similar to that shown in Figure 4.5. The time interval between each image could be requested pre-shot by the user. The timing of the images is within ±5 ns of the laser hitting the target, t_0.

A script was written and used to measure the distance to points in the image from a pre-defined target chamber centre (TCC). The code fitted a Gaussian curve to the intensity profile of the shock and took the position of the outer edge of the shock to be the base edge of the Gaussian peak. TCC was noted by using an alignment He:Ne laser to illuminate a wire target in pre-shot images [108]. The code plotted a Gaussian fit to the intensity profile at the outer edge of the emission

front. It then calculated the distance to the maximum intensity from TCC. This method of measuring the distance to the emission front has also been compared with measuring the distance by eye and the two methods agree to within an error of ±0.5 mm. The distances were measured in pixels on the images and converted to cm. The conversion value was determined by measuring the number of pixels across the known width of the target or from the distance between TCC to the B-dot probe.

4.4 Aluminium Foil Target Results

Figure 4.5 shows self-emission images recorded from a 5×5 mm, 10 μm thick aluminium foil target on which is focussed a total laser energy of 1500 J. The images are evenly spaced at 35 ns intervals, where time t=0 ns corresponds to when the laser beams hit the target. The image is the direct observation of bright self-emission from the aluminium plasma produced at the target and also from the background argon gas fill.

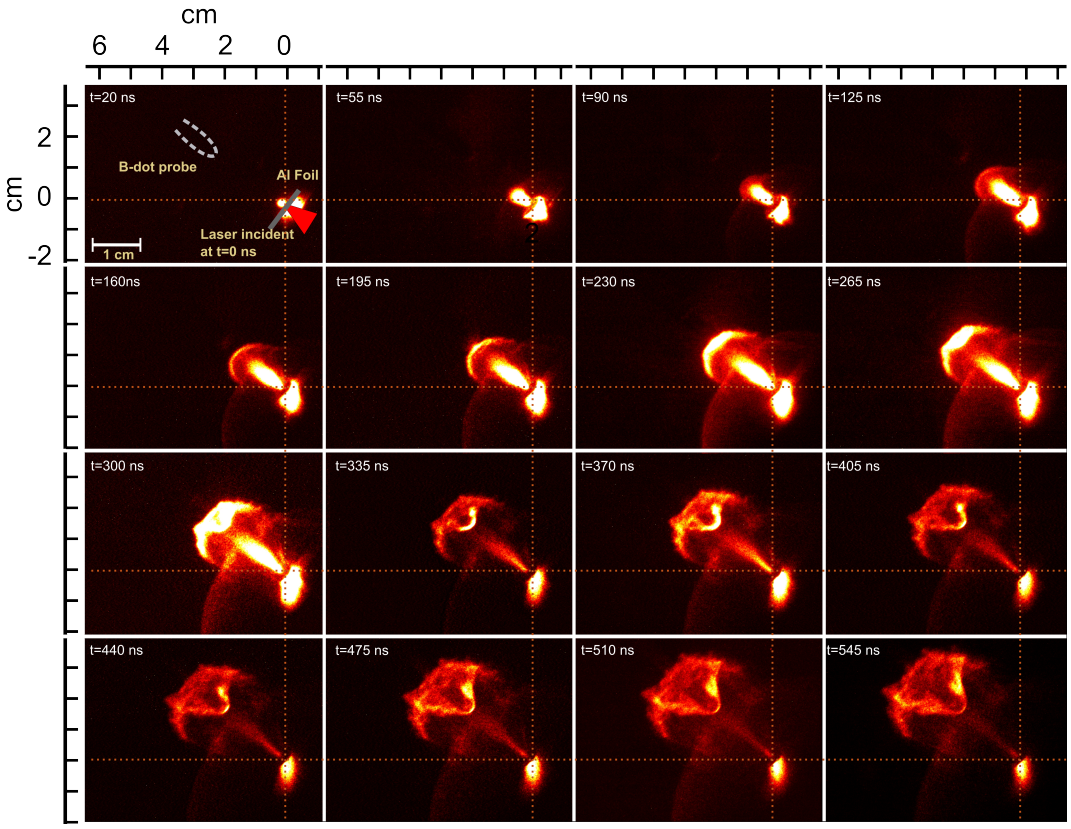

Figure 4.5: Images taken with the fast framing camera observing the self-emission from an aluminium foil in a 0.7 mbar background argon gas over time. The images are taken with a 5 ns exposure, separated by 35 ns. T=0 ns is the time when the lasers are switched on.

The target can be seen to be glowing at early times and a wide hemispherical emission front is launched along with a faster, more collimated, jet-like feature, following plasma breakout at the target rear surface. A glowing wider region in the lower right corner is assumed to be a hotter and denser area made up from the bulk ejected target material. Considering the image at 230 ns there are four main features observed. As already mentioned, in the lower right of the image the target material is emitting brightly. To the left of the target is a jet-like emission feature which has, ahead of it, a small, bright hemispherical emission front. In line with the tip of the jet-like feature is another dimmer, wider emission front propagating outwards.

The emission fronts and jet-like feature propagate into the argon gas, centred along the target surface normal and move towards the B-dot probe, driven by momentum conservation, as target material ablates away from the target front surface. The probe is placed at 3 cm distance from the Al foil target. Monitoring the wider, dimmer hemispherical emission front and measuring the distance travelled, suggests that it initially expands at ~200 km/s perpendicular to the target surface. As the emission front expands, it slows to ~65 km/s by 480 ns. These velocities are estimated to have a 10% error associated with them from measuring the distance to the edge of the emission front.

As the flow starts to approach the B-dot probe at 300 ns it appears that the edge of the emission front, nearest the probe, emits more intensely and starts to curve around the probe. It has also been observed from other time-sequences taken using the SIM16 [105, 109] that the probe appears to drive other structures within the plasma as it is disturbed.

In general, the differences in the intensity of emission across the image depends on the density and temperature of the plasma [110].

4.5 Plastic Sphere Target Results

Unlike the aluminium foil targets, the plastic spherical targets did not produce the jet-like features. An example of a fast framing camera image of the 2 mm spheres, in a 0.7 mbar argon background gas, is seen in Figure 4.6. The laser, for this shot,

had an energy of 1400 J and pulse length of 2 ns. The images in Figure 4.6 are separated by 30 ns. These images show that there appears to be two shock-like structures being produced in the interaction. There is a much wider, flatter front (highlighted by the green line) and a second, brighter emission front (highlighted by the blue line) which appears to be travelling at a slightly faster velocity of ~ 70 km/s at 260 ns, compared to the flatter shock's velocity of ~50 km/s. By 440 ns the two structures appear to be more separated and distinct, although both features are starting to slow down. These velocities also have a 10% error associated with them.

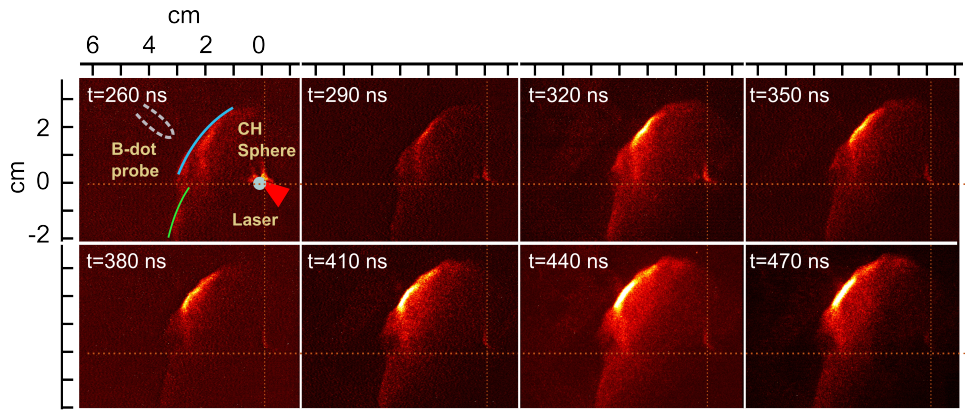

Figure 4.6: 8 of the 16 images collected using a plastic sphere target in a 0.7 mbar background argon gas. These images show the two features being emitted from the shock, highlighted with the green and blue lines. The images are taken with a 5 ns exposure.

4.6 Carbon Rod Target Results

A 500 μm diameter carbon rod target in a 0.7 mbar argon background gas was also used with a laser of 1500 J, as shown in Figure 4.7. The first impression of the images is that the emission front is smooth and fairly spherical. At early times (< 60 ns) the main target is seen to glow, while an emission front is launched into the surrounding gas. The emission front propagates out towards a B-dot probe sat 3 cm away from the main target. The emission front is much smoother than has been seen for aluminium and plastic targets and hemispherical in shape. As time progresses the emission front increases in size, growing dimmer beyond 380 ns.

The interferometry and schlieren imaging cameras also recorded images, as seen in Figure 4.8, showing similar shaped blast waves to those observed by the SIM16 camera. However, due to their single image per shot, a series of shots are

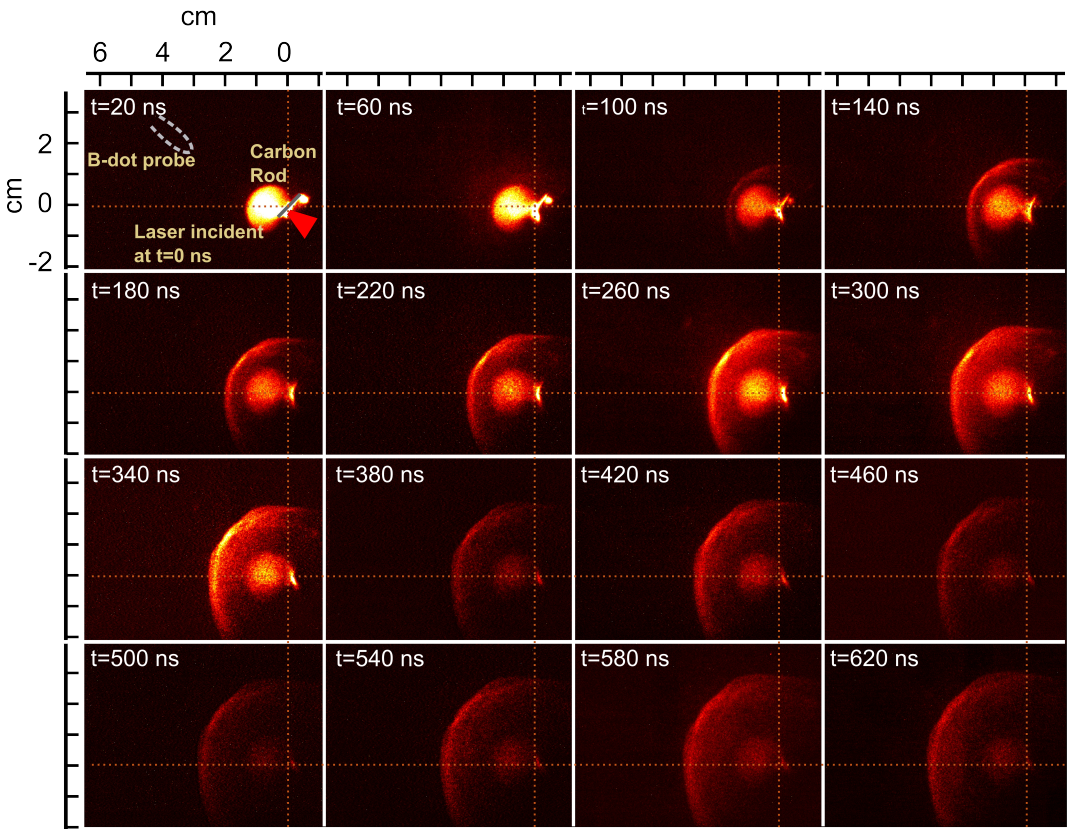

Figure 4.7: Images of the emission front emerging from a 500 µm carbon rod target, in a 0.7 mbar argon background gas. Images are all taken with a 5 ns exposure, separated by 40 ns.

required to build up a time sequence to help understand the evolution of the blast wave. The interferometry images show the shock front from the shift in the interference lines. These images are analysed using similar methods to the SIM16 images, as detailed in Section 4.3.2, to record the shock front's propagation distance with time.

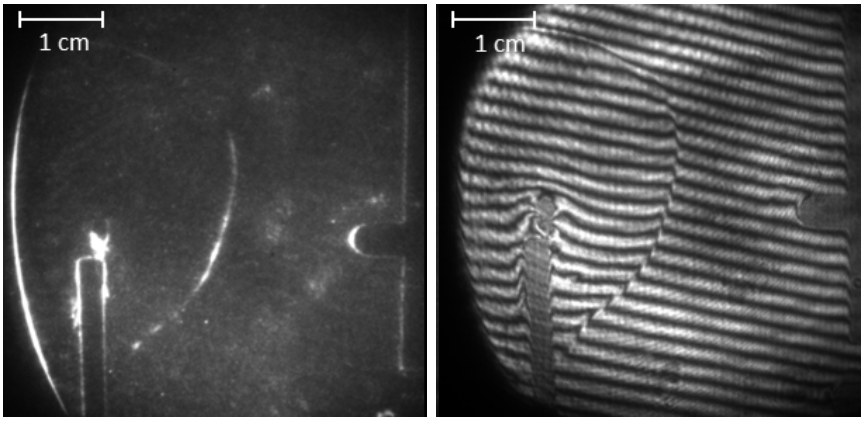

(a) Schlieren image at 143 ns. **(b)** Interferometry image at 163 ns.

Figure 4.8: Images collected of a carbon rod target shock wave produced in 0.7 mbar of argon gas using the optical probe cameras.

4.7 Analysis of Sedov-Taylor Phase of Blast Waves

Of interest is the blast wave shape with time, so the distances from TCC to the emission front at angles were measured. The angles were measured with respect to the vertical (0°) in the image orientation. The direction directly opposite the laser is 51°. The different projection angles were taken from 0° to 105° as shown in Figure 4.9 and the distances plotted against the time for each of the 16 images.

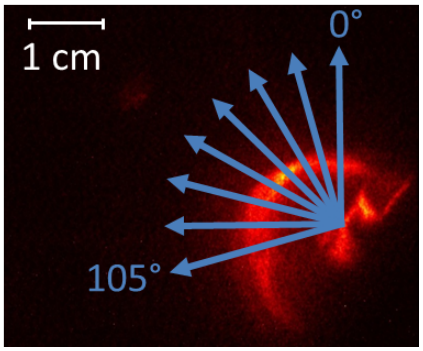

Figure 4.9: An image at t=220 ns showing the different angles the emission front points were measured at, where 0° corresponds to the vertical.

In Figure 4.10 the data taken at 60° is compared to a Sedov-Taylor fit with $\alpha E/\rho$ as the only free parameter (green dashed line). It is seen that this Sedov-Taylor fit does not match the data well at early times. This is expected as the early time expansion will be ballistic. To account for this we add the terms t_0 and R_0, for the initial time and radius, respectively, as shown in Equation (4.1) as additional free parameters, effectively defining the time and position at which the Sedov-Taylor phase starts. The result is shown in Figure 4.10 as the red line and fits the data well. This has assumed that the peak emission point is close to the shock front, which we will investigate the validity of shortly.

$$R(t) = R_0 + A\left(\frac{\alpha E}{\rho}\right)^{\frac{1}{5}}(t - t_0)^{\frac{2}{5}} \tag{4.1}$$

The Sedov-Taylor fits are then applied to each angle using Equation (4.1), where A is the dimensionless term ($A = 1.15167$) [53] solved from exact solutions for an ideal gas. The results of the fits are shown in the graph 4.11 and the numerical fit parameters are given in Table 4.1.

From the results for R_0 and t_0 it is possible to extract crude estimates for the ballistic velocity, u_B and the mass swept up by the blast wave. The initial radius

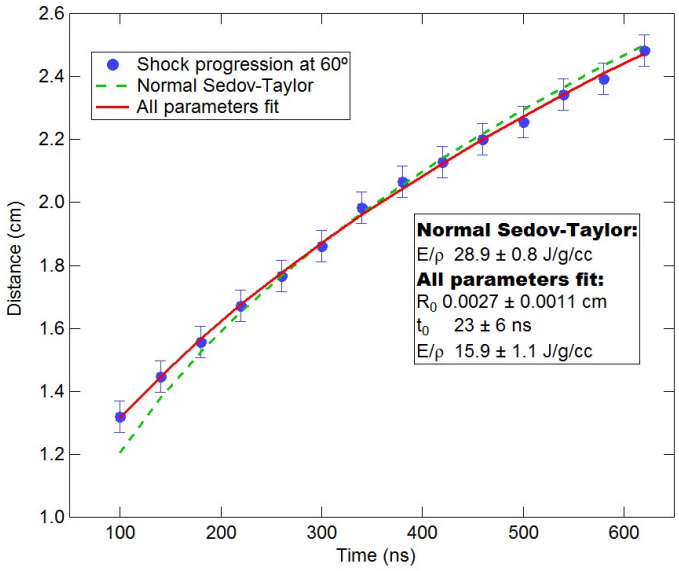

Figure 4.10: Different Sedov-Taylor equation fits applied to the experimental data. The data are shown by crosses. The green line shows the Sedov-Taylor equation fitted using just E/ρ as a free parameter and the red allows R_0, t_0 and E/ρ to be fitted to.

and time for the Sedov-Taylor fit, where the ballistic phase has ended, correspond to ballistic velocities of ~100 km/s. The early ballistic phase is harder to be observe in the self-emission as the emission front is close to the initial interaction point and saturates the signal. The overall trend in the table shows that the shock travels

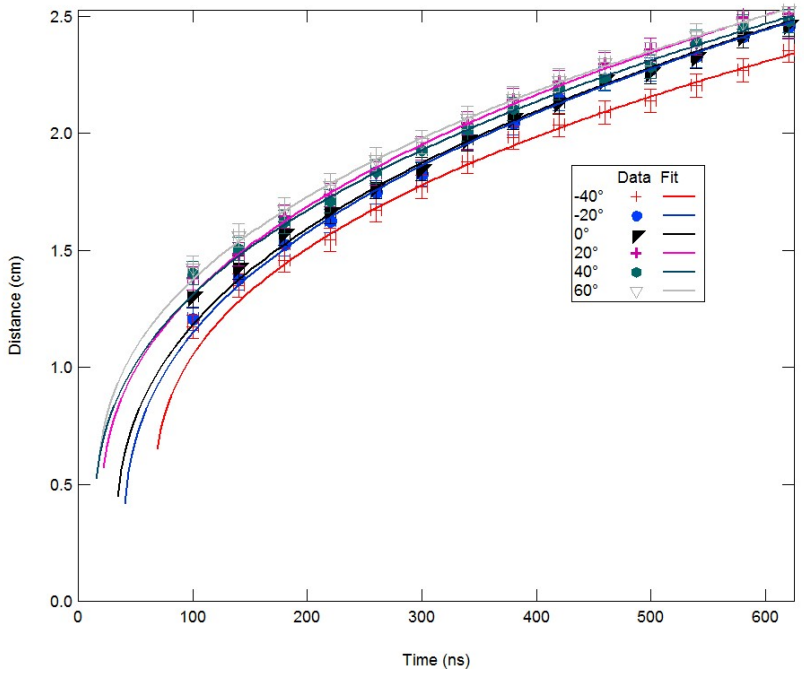

Figure 4.11: Sedov-Taylor fits to blast wave propagation distance at different directions around the emission front with a 0.7 mbar argon background gas and 500 µm carbon rod target.

Angle	−40°	−20°	0°	20°	40°	60°	Mean
R_0 (cm)	0.43	0.25	0.22	0.32	0.30	0.40	0.32
t_0 (ns)	66	40	30	19	14	17	31
E (J)	8	16	17	15	14	12	14
α	0.005	0.011	0.012	0.010	0.009	0.008	0.009
u_B (km/s)	65	64	73	168	214	235	134

Table 4.1: A table of the fitted parameters using a 500 μm carbon target in a 0.7 mbar argon background gas with a laser energy of 1500 J.

furthest in the directions towards the sides of the shock than opposite the laser axis initially. However it seems it is only towards the open ends of the target at 60°that the front also has a larger velocity.

The results for the energy and ballistic velocity, as well as the assumed radius at which the ballistic phase ends, can be used in two separate calculations to work out the mass swept up by the blast wave. The results from 60° yield a mass of 4 ± 1 ng using the energy and ballistic velocity to calculate the mass swept up. If the radius, R_0 of the blast wave is used with the initial background gas density, then a mass of 10 ng is calculated.

These fits also show that about 0.7-1.5% of the laser energy is absorbed into the blast wave. This is the trend seen across the different shots, with most fits corresponding to a maximum energy absorbed of 1-2% from the laser. The rest of the laser energy will be lost in heating of the target or be carried away in the ablated material. There is also a variation in the emission front propagation distance and, therefore, energy absorbed from the laser at each direction plotted along the emission front. The differences seen here are further investigated in Section 4.8.

The general fit to the points suggests that the blast wave does evolve and match a Sedov-Taylor phase progression, albeit with different trajectories at various points along the front.

4.7.1 Helios Simulations of a Sedov-Taylor Blast Wave

These fits to the data can be compared to simulations run using Helios[111] in a 1D spherical geometry. The trajectory of the blast wave at 60° is overlaid on top of a plot mapping the electron temperature with time, as shown in Figure 4.12.

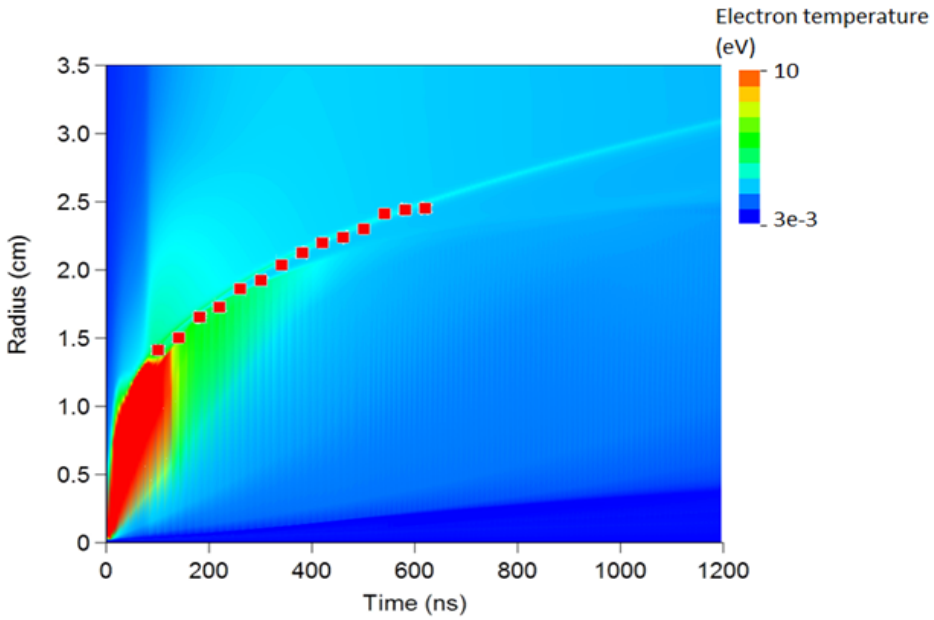

Figure 4.12: A 1D spherical simulation in Helios of a carbon rod expanding out into a 0.7 mbar background argon gas. This plot shows a map of the electron temperature and is overlaid with experimental data points of the blast wave progression at 60° to the vertical axis of the images.

The simulations also fit a Sedov-Taylor trajectory after an initial ballistic phase. This shows the blast wave's expansion is adiabatic. Tuning of the Helios simulations was carried out by varying the value of the input energy. We find that the simulation is consistent with the experimental results at 60° when 5% of the laser energy is included in the simulation. This is roughly 7× the energy coupled to the blast wave in the experimental results. The increase in the energy needed is most likely due to the simulation also taking into account either energy lost in the target from heating, energy not transferred directly into the blast wave or only a small mass of the initial target becoming the 'pusher' for the blast wave. The energy will actually be even higher than used currently, as the emission front, which is being matched here, is shown in Section 4.9, to be slightly behind where the shock front actually occurs. The Helios simulations calculate a shock temperature of 2-4 eV which is what has been estimated from the spectroscopy collected on the experiment.

The ballistic phase of the shock can also be measured from the simulation. The different zones of material are plotted using Helios in Figure 4.13. The expansion of the ballistic phase lasts for ~20 ns and expands to ~6 mm. This then gives a velocity of ~ 300 km/s. This velocity is larger than the ballistic velocity extracted from the

experiment. The experimental value for the ballistic velocity varies to that from simulation as it is not from a point explosion and only calculated from using the time and radius at which the Sedov-Taylor phase begins at. The simulation simplifies the experiment and in doing so a front side expansion and rear side expansion are more complicated to understand in this spherical geometry.

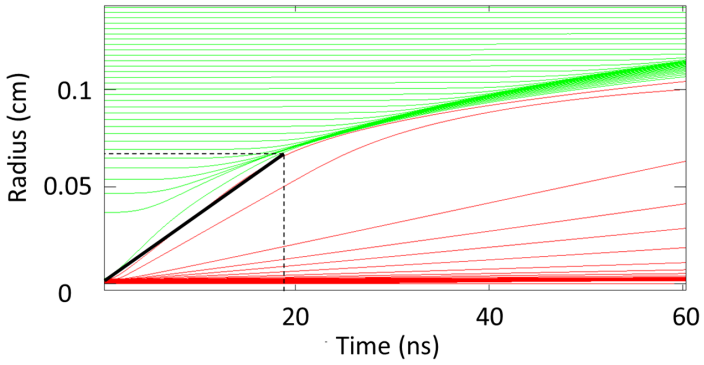

Figure 4.13: The initial ballistic expansion of a carbon rod. Zone boundaries shown from a Helios simulation. The green lines represent the argon background gas and the red lines are the carbon rod target material.

4.8 Analysis of the Blast Wave's Symmetry

The images were further analysed to monitor the blast wave shape with time as the emission front travels different distances in various directions. The asymmetric blast wave shape is important as it results in non-parallel pressure and density gradients, so the Biermann battery effect can generate magnetic fields.

The simplest method to capture information about the asymmetric shape of the emission front is to fit an ellipse to the points of peak emission. An ellipse function with a tilt can be overlaid to the points across the emission front, with the function as shown in Equation (4.2)

$$1 = \frac{(x\cos\phi + y\sin\phi)^2}{R_a^2} + \frac{(x\cos\phi - y\sin\phi)^2}{R_b^2} \tag{4.2}$$

where ϕ is the tilt angle, R_a is the major radius, R_b is minor radius and y and x are the coordinate locations of the emission front. We use an ellipse function with a tilt as the axes of the ellipse may move. Figure 4.14 demonstrates how the ellipse was matched onto the images.

The ellipse fitting can accept a pre-defined ellipse centre or allow these to

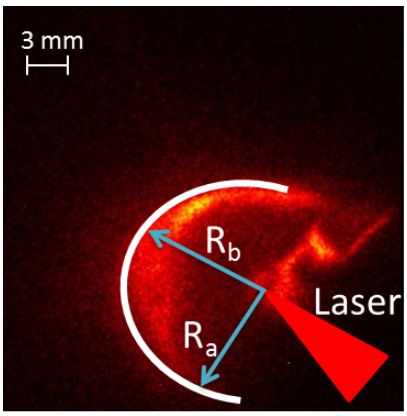

Figure 4.14: A diagram showing where the major and minor axis of the ellipse correspond to. The major axis, R_a, is initially aligned approximately perpendicular to the laser axis, and the minor axis, R_b, is opposite the incoming laser direction.

be another fitting parameter. The result from taking the TCC point to be the centre of the ellipse, (0,0), was compared with the result from allowing these as free parameters. The results of these fits are shown in Figure 4.15 and found to vary only a small amount in observed goodness of fit. However, the values for the fitted position of central x and y values ranged widely, so the pre-defined origin, (0,0), will be used in fitting an ellipse to the data.

After fitting the ellipse, the ratio of R_a/R_b was plotted with time, where R_b is the axis closest to that of the laser direction which, after analysis, is found to be the minor axis. The major axis R_a is perpendicular to this, in the direction closest to

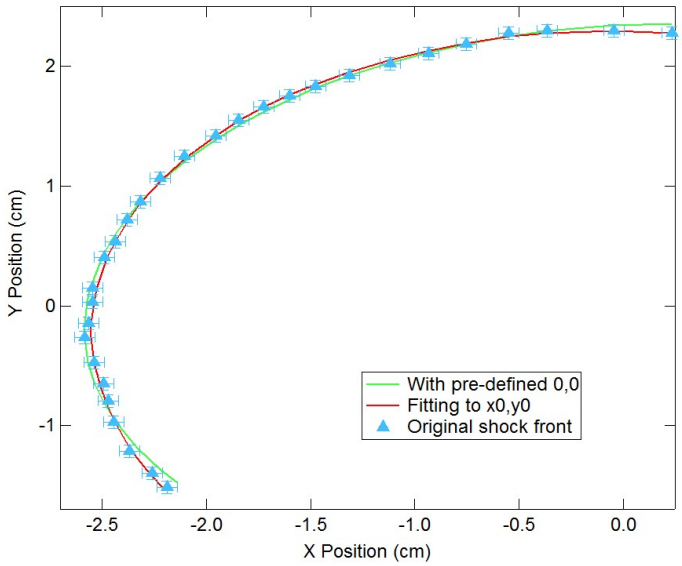

Figure 4.15: A graph of the original emission front location and two ellipse fits to this data. One fit uses a pre-defined (0,0) location (TCC) for the ellipse and another allows this to be also fitted by the function.

the target stalk axis. The ratio $\frac{R_a}{R_b}$ is useful in describing the global asymmetry of the blast wave. A spherical blast wave would have a ratio of 1, a blast wave which propagates furthest in the axis parallel to the laser would have a ratio <1 and a blast wave propagating furthest in the axis perpendicular to the laser will have a ratio >1.

4.8.1 Fast Framing Camera Images

A plot of the ellipse ratio over time for different shots is shown in Figure 4.16. From this ratio we can see the blast wave has a ratio >1, meaning we do have larger expansion of the blast wave in the direction perpendicular to the laser axis. This ratio changes with time for all shots, tending towards 1. The ratio calculated is independent of calibration errors, due to any error applied to both axes being cancelling out.

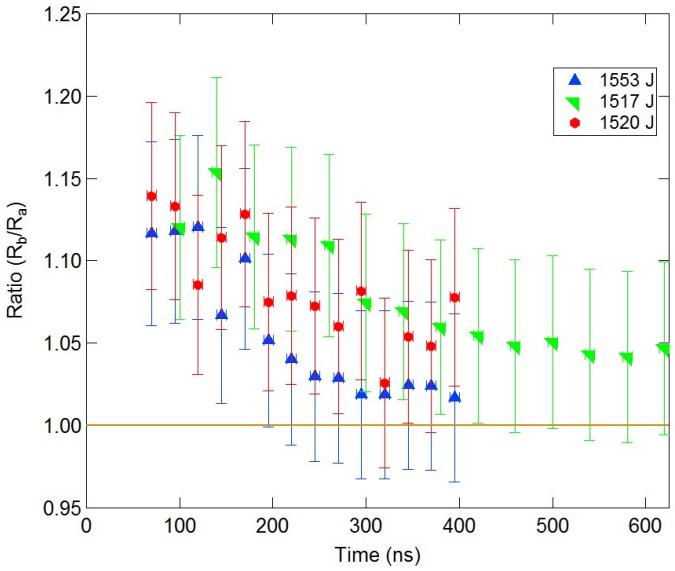

Figure 4.16: A graph showing the evolution of the ratio of the major to minor axis of the fitted ellipse over time. The ratio is observed to decrease and tend towards a symmetric blast wave shape (R_a/R_b = 1).

We can also monitor the tilt, ϕ, and find this to be approximately constant with time. The tilt has an average of 23±5° over the duration of the shot. The ellipse was expected to have a tilt, with a minor or major axis lying along the direction of the laser, i.e. 51±3° (0.89 ± 0.05 rad). There are larger differences in the tilt when comparing different shots to each other, likely due to the initial target angle and position at which the laser hits the target. The further up the target stalk, towards the open end, the laser is pointed the more the shock will be able to expand in the

direction directly opposite to the laser, as there will be little target material in front of the shock to impose on its expansion.

The minor axis length (i.e. the axis closest to opposite the laser) for a number of shots is plotted in Figure 4.17a. The data shows that this length for different shots of nominally the same conditions has little deviation from each other, progressing with similar trends. This highlights that the differences in ratio between shots is due to expansion in the axis perpendicular to the laser direction, as shown in Figure 4.17b, which would be due to laser pointing and target alignment.

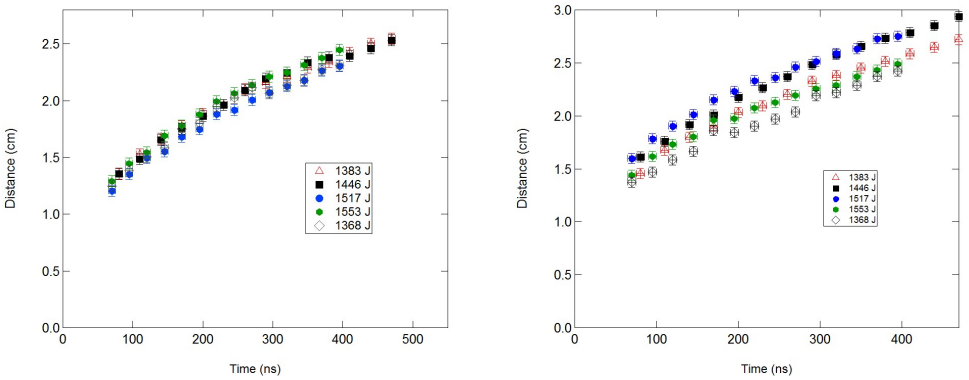

(a) Minor axis of ellipse **(b)** Major axis of ellipse

Figure 4.17: A graph showing the minor and major axes distance for shots of energies between 1.36-1.6 kJ.

The conclusions that can be drawn from this analysis are that the angle of the tilt of the blast wave ellipse is constant with time, although the value varies from shot to shot, as expected from the positioning and angling of the targets. The ratio decreases from about 1.12 ± 0.01 to 1.05 ± 0.01 at about 400 ns, when the blast waves slow down. The evolution of the shape of the blast wave also slows down and plateaus.

4.8.2 Schlieren and Interferometry Images

Figure 4.18 shows the ratio of the major to minor axis of the blast wave, measured from the interferometry, schlieren and SIM16 images. There are small variations in the ratios of the interferometry and schlieren due to the data being collected from different shots. However the general trend shows a decreasing ratio over time, tending to a more symmetric blast wave. This supports the observed trend from the SIM16, which approaches a ratio value of 1 over time for the carbon rod targets.

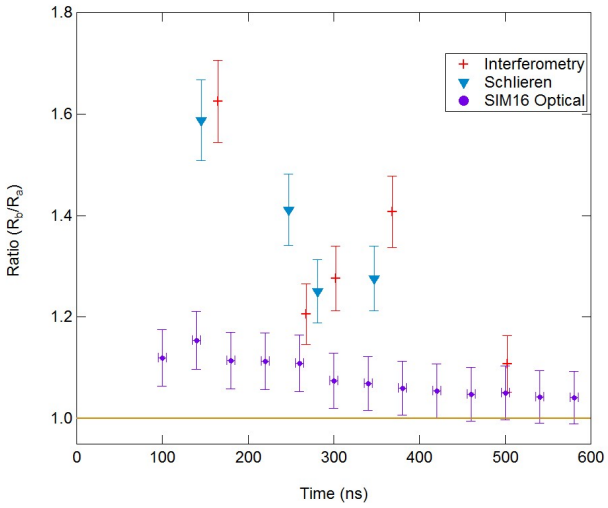

Figure 4.18: Graph of the ratio of the interferometry and schlieren imaging compared with that of the SIM16 for a carbon Rod target in a 0.7 mbar argon background gas.

The initial ratio from the schlieren and interferometry is much larger than that of the SIM16 (R_a/R_b= 1.6 compared to 1.2). This is due to several contributing factors. The imaging of the interaction for the two different systems comes from two mirrors after the target; one for the optical probe and one for imaging the optical emission. These mirrors are both mounted directly above the experiment, however the SIM16's first mirror after TCC is slightly displaced, at 10°, from being directly above the interaction. This may have some influence on the measurements being made of the shock front, but due to the 3D nature of the shock this will only affect the results by a small amount. It has been noted from the individual measurements of the major and minor axis, that the minor axis, i.e. close to the laser direction, is in generally good agreement with the minor axis measurements from the optical probe data. This means it is the major axis which varies the most, i.e. the direction perpendicular to the laser. The other reason that the optical probe images do not match to the SIM16 data is due to where the optical emission and the strongest density gradients occur. These two points do not have to occur at the same place, as the steepest density gradient occurs at the shock front, and if the shock is optically dense or emitting in a different range to that being imaged, the emission front will not occur in the same place. We can look at simulations to support these assumptions.

4.9 Simulations of a Blast Wave using FLASH

Simulations are run in 2-dimensions using FLASH [112]. In the simulations a cylindrical symmetry was assumed, modelling the carbon rod as an infinitely extended, circular disc along the rod axis, z, resolving the plasma dynamics in x and y. The laser is incident at (0,r_0), where r_0 is the radius of the rod (250 μm). The laser comes in from below the x-axis, parallel to the y-axis, driving the shock out. The carbon target had a density of 2.26 g/cc and propagates out into an argon background gas of 1×10^{-6} g/cc (i.e. 0.7 mbar). All other conditions were the same as for the experiment, using a 2 ns top-hat laser profile.

The simulation uses a grid of boxes which are 2500×2500 μm in size and with adaptive mesh refinement (AMR). This means that the resolution can be increased where gradients in density and temperature exist. The smallest computation element is 25 μm.

The simulations, shown in Figure 4.19, display density profiles on the LHS and emission on the RHS for the blast wave. The shock front is shown as the region of higher density which travels ahead of the following plasma. The emission plots show where the plasma most strongly emits in the 1-10 eV range.

The peak emission region is often behind the location of the shock front. The shock front can still be seen in the emission plots, but is a less strongly emitting region. The emission shows two 'fronts', most apparent at 231 ns and are separated by about 0.5 cm in the x-axis direction. By 361 ns these two fronts are less distinguishable and the emission front is closer in location to the shock front occurs. These plots show that the radiating regions are behind the shock front early in time in the x-axis direction but not in the y-axis, although the radiating region takes on a similar shape to the shock. The evolution of these shocks at early time expands out furthest in the direction perpendicular to the laser axis. The blast wave takes on the asymmetric shape which tends to a more symmetric shape over time.

The blast wave distance, continuing in the direction of the laser (parallel to the y-axis), also matches that measured from the experimental data and the brighter emitting regions are very close to the shock front. However, the direction perpendicular to the laser is turbulent and it is harder to estimate the edge of the shock

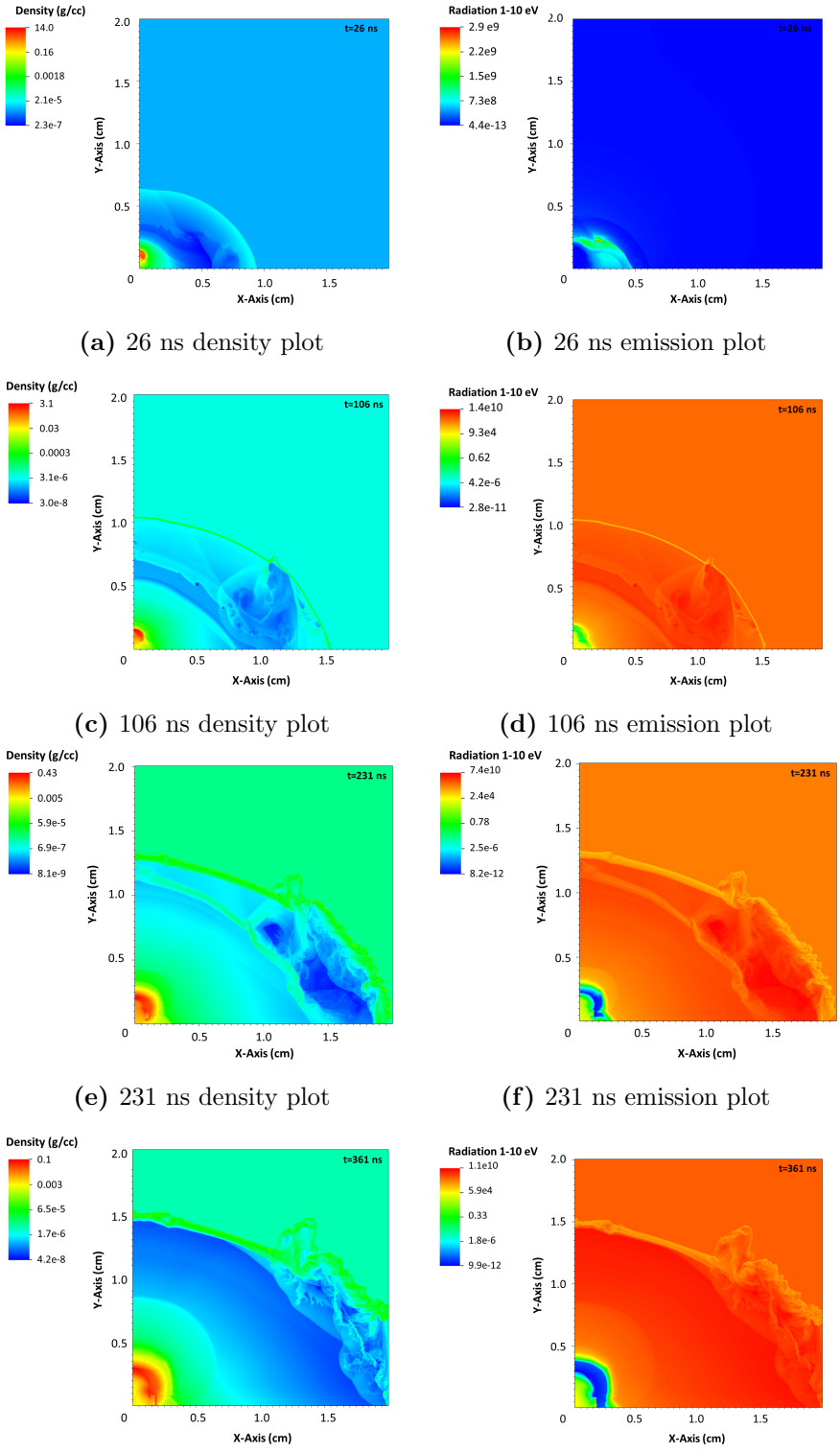

(a) 26 ns density plot **(b)** 26 ns emission plot

(c) 106 ns density plot **(d)** 106 ns emission plot

(e) 231 ns density plot **(f)** 231 ns emission plot

(g) 361 ns density plot **(h)** 361 ns emission plot

Figure 4.19: FLASH simulations of a carbon rod showing the 1-10 eV emission plots and the electron density at various times. The laser is incident on the rod in the direction parallel to the y-axis [113].

front at this point. This might explain why there are differences in the shock front obtained from the interferometry or schlieren and the SIM16. We also see in the

interferometry and schlieren data that the ratio of the major to minor axis at early time is large and evolves towards one more similar in value to that measured from the SIM16. This would support the shock front and emission front occurring at the same point later in time, which can be seen in the simulations plots at 361 ns where the density peak and emission peak are almost matched in location. The simulations are also able to simulate the conditions using a plastic sphere of 2 mm diameter, shown in Figure 4.20. In this simulation a second, slightly smaller bubble appears further ahead in the y-axis direction than the larger shock front. It can be seen very clearly from these results that they support the experimental data. At early times the blast waves expands equally in the parallel and perpendicular directions and show a second much faster shock progressing parallel to the laser direction compared to that perpendicular.

These simulations allow us to conclude that two shock are being produced in the interaction and the two shocks progress at different velocities. They also give insight into the behavioural differences between blast eaves driven by carbon rods and plastic spheres.

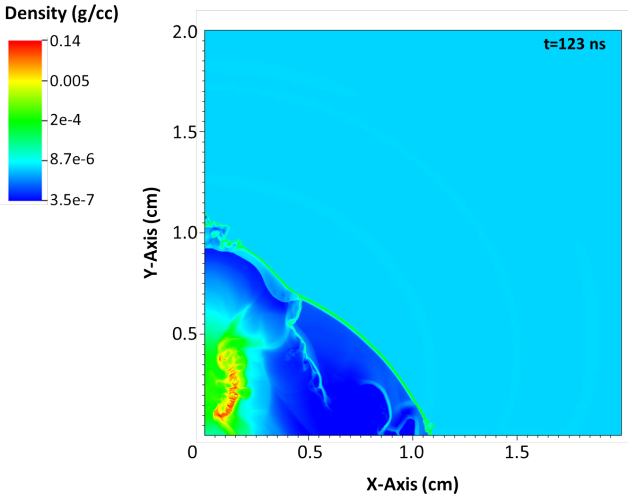

Figure 4.20: A FLASH simulation of the mass density of a 2 mm plastic sphere a t=123 ns after the laser had been switched on in a 0.7 mbar argon background gas. The second shock wave produced through the target is starting to expand further in the y-axis than in the x-axis.

4.10 Production of Two Shock Waves

The reason for having a decrease in the ellipticity like that shown in Figure 4.16, is due to having two shock waves being produced in the interaction, emerging from both around and through the target, as seen in Figure 4.21. The first shock wave is produced from material being ablated from the front side of the target and passes around the target, expanding out at the rear side. The target stalk inhibits the expansion of the ablated material, thus biasing the ellipse to be orientated towards the open end of the target, where the material can expand out more easily and in a direction more perpendicular to the laser direction.

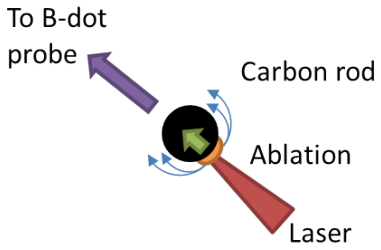

Figure 4.21: A diagram showing the production of two shocks from the carbon rod. The blue arrows shows the first shock produced from ablated material expanding around the end and sides of the target. The green arrow shows the second shock through the target. The purple arrow gives the direction to the B-dot probe.

The initial shock expands out around the target, but meanwhile a shock has been produced from the shock driven into the target by the laser. This shock appears later in time as it has to travel through the target, before breaking out from the rear side. It is a faster shock wave and, under the right conditions, catches up with the slower shock. In carbon rods it is observed that the shocks have slowed down and move together without changing the separation between the two. The second shock pushes the first shock out further in the direction of the laser axis, and so whilst the sides of the shock are slowing down even further, the front is able to expand more, and create a more symmetric shock. If, however, the second shock wave catches up with the first earlier in time, then it will break through the first and they will travel more independently. This latter situation occurs for the plastic sphere targets.

The production of these two features is more obvious using targets such as aluminium and plastic. The plastic spheres, produce two very distinct spherical shock- like structures. However, the shock waves do not seem to merge, like that

seen in carbon targets. Instead they progress even further to creating an asymmetric shock but with the minor and major axis flipped by 90°. The carbon rod shock evolution has already stalled before the second shock has caught up with the first, therefore the two shocks never cross and flip the ellipse's axes.

4.11 Conclusions

Blast wave experiments are single shot and obtaining a time series to develop an understanding of the plasma dynamics can take many shots when using single frame cameras. The temporal information that can be gained from fast framing images is instantaneously advantageous for noting how the laser-plasma interaction progressed, and to decide where regions of interest might be for other diagnostics to look at spatially or temporally during an experiment. Importantly, they also help define the next laser shot.

In the results gained on the experiment we can observe the production of two asymmetric blast waves from the self-emission in the ambient background gas. We can fit an ellipse to the shock front and the ratio of the major and minor axis decreases over time. This is due to a second shock wave being produced later in time as the piston emerges through the target. This shock pushes the overall blast wave shape to being more symmetric for carbon rod targets.

Different, narrow bandwidth filters could have been used in this experiment to assist in gaining local temperature measurements of the plasma, by using specific emission lines of argon, and calculating their relative intensities [110].

Chapter 5

Magnetic Reconnection

5.1 Introduction

Magnetic fields in astrophysical and laboratory plasmas have complex generation and interaction mechanisms. As these mechanisms are not well understood they are the focus of many research programmes. The study of magnetic fields generated around laser spots is applicable to ICF research, where multiple lasers are focussed onto a fuel capsule or into a hohlraum [65]. The interaction and possible dissipation of energy contained within the magnetic fields, rather than heating of the target may be at the detriment of achieving a high gain from fusion power [5].

This chapter contains an introduction to reconnection and presents the results of an experiment at the Orion facility, AWE. The aim was to study reconnection between two laser spots. The set-ups used in this experiment are explained as a number of target orientations relative to proton and optical probes are used. The results from the proton radiographs using one beam are shown first. Then proton radiographs using two beams in close proximity are presented. This is followed by a description of the results from a streaked interferometer, a gated X-ray detector and an X-ray spectrometer. Simulations using a hydrocode, NYM [114], and a VFP code, IMPACTA [38, 115], are outlined. Indeed the simulation results support the experimental observation. The discussion section of this chapter presents a semi-collisional reconnection model, which requires the inclusion of Nernst effects and anisotropic pressure terms. Finally a summary of the results and findings, with potential further work, is given.

5.2 Motivation

Opposing magnetic fields can lead to magnetic reconnection events where field lines rearrange and reconnect into new geometries, releasing stored magnetic energy as particle kinetic energy. The study of magnetic reconnection is an extremely broad field, due to its application to many processes and systems, such as within tokamaks [116, 117] and numerous astrophysical objects [118, 119]. There have been many theoretical and computational studies conducted into these areas, although there have been fewer supporting experimental papers. More detailed reviews of magnetic reconnection can be found by Yamada *et al.* [120, 121], Priest and Forbes [122], Biskamp [123], Birn and Priest [124], Zweibel *et al.* [61] and Lewis *et al.* [125]. This chapter will concentrate primarily on the experimental research being undertaken to reproduce magnetic reconnection in plasmas, using high power laser facilities.

In laser experiments, azimuthal magnetic fields are generated around the laser spots by gradients in the temperature and density, $\nabla T_e \times \nabla n_e$, at the edges of the heating region. An experiment by Yates *et al.* in 1982 [126] reported on various laser geometries of 2, 4 and 8 beam spots of 120 μm in diameter, separated by 1 mm onto planar and curved targets of nickel, gold and copper. The experiment was supported by simulations which predicted that, with a laser wavelength of 10.6 μm and intensity of 5×10^{13} W/cm^2 in a 60 μm spot, magnetic fields of up to 1 MG could be created. X-ray pinhole imaging supported simulations and showed a magnetic field null existed between the laser spots, where the fields opposed each other. An

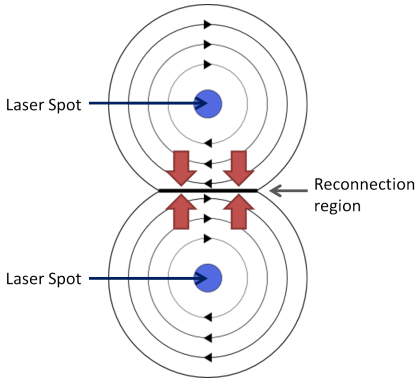

Figure 5.1: A diagram of the magnetic fields produced around laser spots and the region where reconnection occurs.

experiment was also conducted by Nilson *et al.* [28] at the RAL and used two 30-50 μm FWHM laser spots each of intensity 1×10^{15} W/cm^2 incident on a gold

or aluminium foil target. The plasma flows from the laser spots collided and the magnetic fields reconnected in the region between the spots. This is shown by Figure 5.1. A bi-directional plasma jet was observed from the reconnection layer [127]. The jets were diagnosed using shadowgrams, which mapped the electron density variations. Proton grid deflectometry [128], which experienced the magnetostatic and electrostatic fields, was also used to confirm the shapes of magnetic fields in the laser spot regions. The separation of the two laser spots was shown to have an effect on the interactions and 400 μm was the optimum separation for their reconnection to occur. The results were compared with the Sweet-Parker model, which predicts a slower rate of reconnection than that observed experimentally.

Li *et al.* [29] undertook an investigation into magnetic reconnection, using 2 and 4 laser spots of 800 μm diameter, giving an intensity of ~10^{14} W/cm^2 onto a plastic target. The fields created by these spots were diagnosed using proton deflectometry and the reconnection rates were found to be faster than the Sweet-Parker model. Steady-state reconnection models were also discussed, but due to the 3D nature of the experiment detailed analysis of the results was not carried out.

Zhong *et al.* [129] used the SG II laser facility at the National Laboratory on High Power Lasers and Physics, Shanghai in 2012. They used 8 beams to form 4 laser spots of 50 μm diameter, separated by 100-600 μm. The beams of intensity $\sim 5 \times 10^{15}$ W/cm^2 were focussed onto an aluminium foil target, with four beams on one side of the target and four on the other, in two spots. The aim of this experiment was to produce jets from the reconnection region, like those produced in the Nilson *et al.* experiment [28], but with a different geometry. Two types of jets were observed in this experiment using pinhole X-ray imaging. There were no large differences noted to the jets produced from focussing the beams in two spots on one side to having two spots on both sides of the target. The experiment similarly observed that changing the spot separation affected the reconnection region and jets produced [130]. There has been further work done on this experiment by the group. They are now looking into the detail of the geometry of reconnection and the existence of a secondary current sheet. The current sheet is connected to a plasmoid or magnetic island which has been ejected from the primary current sheet. The plasmoid disrupts surrounding reconnecting fields, which results in a secondary

current sheet and flare loops, similar to solar flares [131].

Most recently, work by Rosenberg *et al.* [30] has been published showing results from a two-beam magnetic reconnection experiment onto a 12 μm plastic target. Each laser beam had an intensity of 1.85×10^{14} W/cm^2 for a 1 ns duration. The two beams were focussed 1.4 mm away from each other, and by 0.9 ns the magnetic fields generated had interacted and produced electron jets. These jets emerged from the reconnection region at velocities of 1300 μm/ns. The observations were made using proton radiography and these results are similar to those presented in the following sections, except with the absence of jets in this chapter. The proton radiographs presented by Rosenberg have been taken by probing from the same direction as the main interaction laser beams, leading to protons being deflected in opposite directions to when probing from the opposite side to the main interaction beams, as is the case in our experiment. The dependence of the deflections on the proton probing direction relative to the lasers is shown in Figure 5.2. There are also differences in our experiment in the mechanisms via which the reconnection process is occurring, which will be discussed towards the end of this chapter.

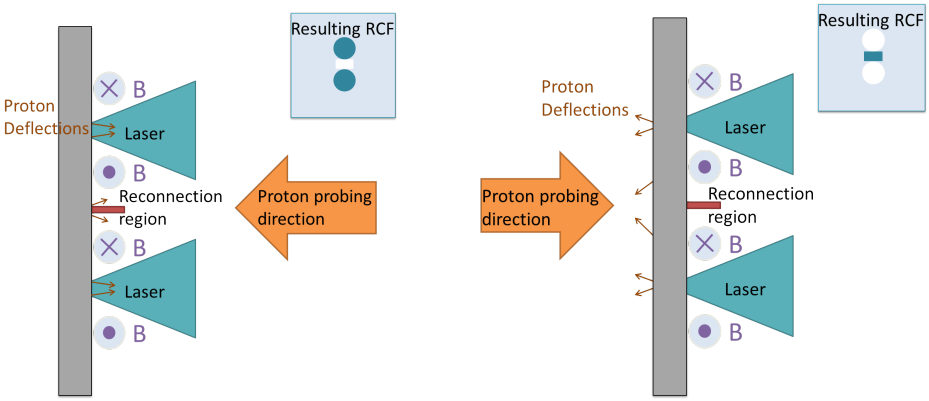

(a) Proton probing from the same side as the main interaction lasers.

(b) Proton probing from the opposite side to the main interaction lasers.

Figure 5.2: Proton probing effects due to probing from the same or opposite side to the main interaction lasers. The protons are either focussed or defocussed by magnetic fields experienced.

Theoretical and computer simulations have been developed to model magnetic reconnection, such as Zhang *et al.* in 2012 [132] who used a particle in cell simulation to model fast reconnection, Liu [133] who theoretically supports recent experimental results with a faster reconnection model, Biskamp [134] who focussed on reconnection via current sheets, discussing and developing theories by Petschek and Syrovatsky

[60, 135] and Joglekar *et al.* [65] who used a 2D VFP code to show the importance of considering heat flows in hohlraum relevant conditions.

There are still questions to be answered about reconnection such as what determines the rate of energy conversion, fluctuations in electron diffusion regions, application to large scale systems and Hall effects which have not been mentioned here, but can be found in review literature [61].

It is also beneficial, in trying to understand a reconnection geometry, to observe the field generations in a single spot without any additional effects. In 2014 Gao *et al.* [136] completed an experiment looking at singles spots, furthering work by Lancia *et al.* [137] and originally, in 1971, by Stamper *et al.* [138]. These experiments investigated the magnetic fields that are produced across the target surface. The primary diagnostic used by Gao and Lancia was also proton radiography. Lancia used a 25 μm mylar target and a 200 J laser in 4 ns whereas Gao used 50 μm plastic foils with 4 kJ energy lasers in 2.5 ns pulses, forming laser spots of similar intensity to that used in the experiment described in this chapter. Both observed a two ring structure on the proton radiographs. These rings are due to the production of fields surrounding the laser spot and at the edge of the coronal plasma. The inner fields expand with speeds of less than the sound speed. When modelling these fields in simulations, terms are needed to account for the Nernst effect, resistive magnetic diffusion and the Righi-Leduc heat flow contributing to the magnetic field growth, as given by Equation (2.58) and considered for the simulations shown in this chapter.

This chapter will address the kinetic processes that occur when two lasers are focussed in close proximity and the advection of the generated magnetic fields into a reconnection region. This experiment was designed with the principal application to high energy density scenarios created in indirect drive ICF, such as at the hohlraum wall.

5.3 The Experiment

These experiments were conducted at the Orion laser facility, AWE in two parts; one in February and one in October 2015. The experiment changed in October from using two proton probing beams at the same time to just one proton beam with the

addition of an optical probe. The ability to probe the interaction in two directions simultaneously was an attractive feature of the Orion facility and a new development on previous reconnection experiments.

The main interaction was driven by two long pulse laser beams which were focussed into two separate, smooth elliptical spots of 150 μm by 220 μm in diameter, orientated so that the major axis of each spot is horizontal and parallel to the other. A typical intensity profile across the spots is shown in Figure 5.3. The difference in the minor and major axes of the focal spot are small and these are the diameters for which 90% of the energy was contained within. The spots were separated vertically by 800 μm from centre-to-centre. This separation was determined from investigations completed in the February experiment for the optimum spot separation. Shots were also taken using just one of the beams on target, to help understand the evolution of the plasma and the effects of adding a second beam in close proximity.

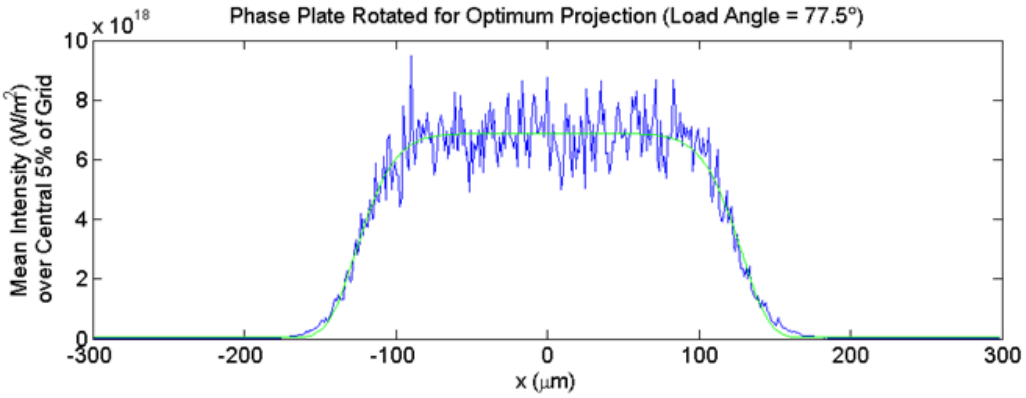

Figure 5.3: The intensity profile across the laser spot with a 300 μm phase plate.

The lasers each contained 400 J in a 1.5 ns stepped pulse, a profile of which is shown in Figure 5.4. 10% of the energy was contained within the first 500 ps resulting in an intensity of 1.5×10^{14} W/cm^2, followed by 4.5×10^{14} W/cm^2 for the remaining 1 ns. This stepped pulse shape was motivated by the high-foot/low-foot laser profiles used at the NIF [139] designed to give a long length scale plasma.

Various target types, of different materials and sizes, were used. The main target materials were thin foils of copper and parylene-D ($C_8H_6Cl_2$). The copper targets were of 5 μm thickness and the plastic targets were 25 μm in thickness, ensuring a thin enough target to minimise scattering of the proton radiography

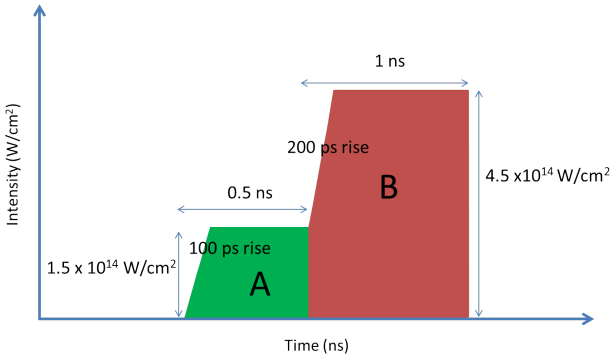

Figure 5.4: A shape of the stepped pulse used in the Orion experiment with 10 % of the energy contained within region A and the remaining energy region B.

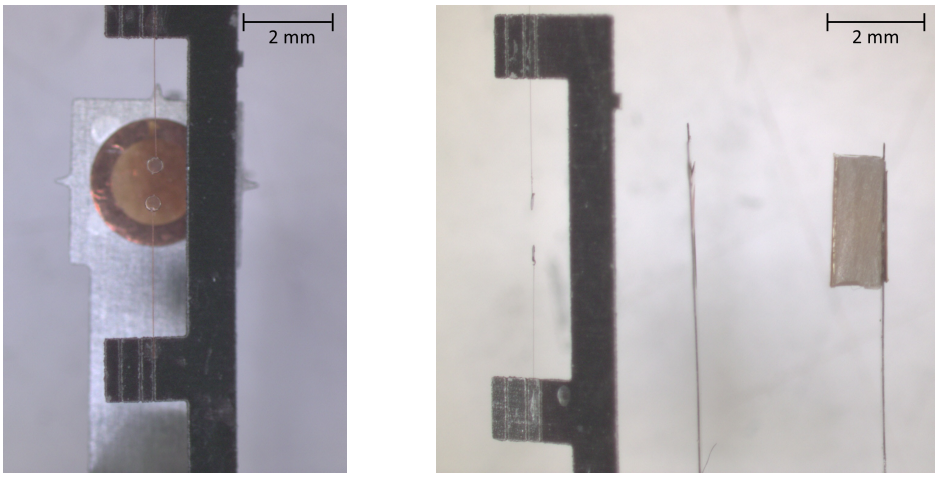

(a) Face-on image of the target. **(b)** Side-on image of the target.

Figure 5.5: Pictures of the novel target consisting of two smaller discs, suspended from an 'F' mount.

diagnostic, but thick enough to prevent the laser beams breaking through early in time. The targets were made into either single 3 mm diameter discs or two smaller 400 µm discs suspended in between an 'F' mount, as shown in Figure 5.5. The two smaller disc targets were designed to allow an optical probe to pass through the interaction in a direction orthogonal to the target surface plane, in addition to probing parallel to the target surface. The target components, including the proton targets, were all pre-mounted onto a solid block to ease the alignment procedure and were metrologised individually for future reference. The plasma and fields produced by the lasers were then diagnosed with proton radiography, an optical probe, GXDs fitted with pinholes and an X-ray spectrometer, some of which have been described in Chapter 3.

The protons were produced from a 1ω wavelength, short pulse beam, focussed

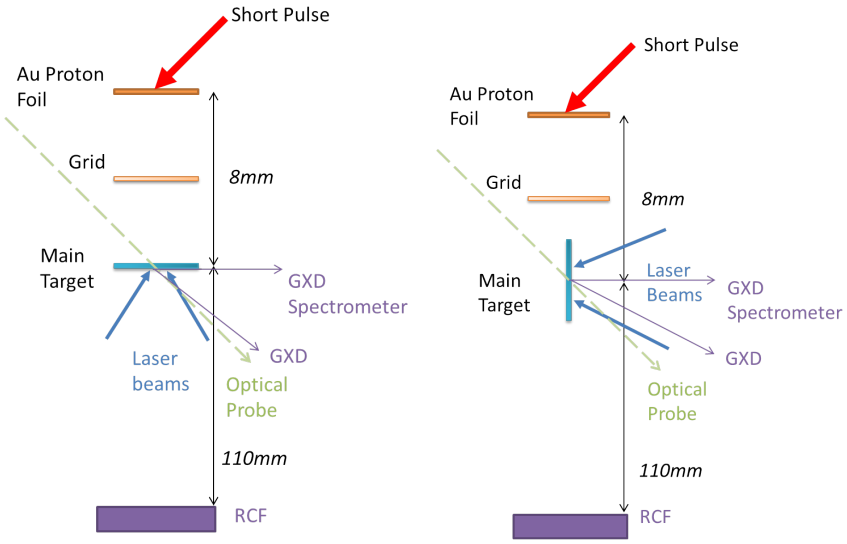

(a) Face-on proton radiography. **(b)** Side-on proton radiography.

Figure 5.6: A diagram of the set-up of the experiment, using one short pulse beam focussed onto a proton target and two long pulse beams focussed onto a main target, which is probed by the protons both in face-on (left) and side-on (right) orientations.

in a 15 µm spot onto a 25 µm thick Au target, containing 200 J in 1 ps. The protons were then passed through a 600 LPI grid which has 35.0±0.2 µm square apertures. The grid was located 4 mm from the proton target, and 4 mm from the main targets. This produced protons up to ~ 45 MeV, although the proton radiographs of greatest interest tended to be around 15-30 MeV. The protons were used to probe the interaction at various times during the main interaction, primarily whilst the long laser pulses were switched on. Timings of the proton radiographs in the subsequent sections are given relative to the start of the long pulses. The RCF was positioned 110 mm from the main interaction target, giving a magnification of 14.75 and 29.5 of the main target and the grid, respectively.

The configuration of the set-up is shown in Figure 5.6, where the main target is rotated on shots to be either face-on or side-on to the proton beam. Due to the layout of the Orion chamber, the optical probe came across the proton beam at an angle of 45°. This meant there were another two orientations of the target for when it was rotated to be either face-on or side-on to the optical probe and 45° to the protons.

The optical probe was 2 cm in diameter and at a wavelength of 532 nm (2ω). The probe beam was 50 ns duration and configured to give 2-dimensional, streaked interferometry, 2-dimensional gated self-emission and streaked polarimetry. The

streaked interferometry was gated to record data over 10 ns.

X-ray diagnostics included the GXDs configured as a pinhole camera or spectrometer. These measured the spot shape, size and separations, and allowed temperatures to be calculated. One GXD had a 16 pinhole array attached to the front, so that 16 images are projected onto the detector. The other GXD, a spectrometer, recorded the chlorine K-shell and continuum emission, as described in Chapter 3.

5.4 Proton Probing of Reconnection Region

The protons produced from the 25 μm thick Au foil were generated by the TNSA mechanism. They were then passed through an additional 2 μm Au filter foil which acted to protect the TNSA target. The protons finally went through a 600 LPI grid to imprint onto the beam and help measure deflections from the fields.

The proton beam has a half divergence angle of ~ 18°, which expands up to 5.1 mm diameter at the main interaction target, encompassing most of the regions of interest. The RCF was made to be 6.2×9.9 cm in size to capture all of the proton beam. Due to the TOF spread in the proton beam and the non-linear stopping power of the RCF stack, high temporal resolution proton deflectometry was able to reveal the evolution of the magnetic fields around the target. The RCF stack is described in Chapter 3.

The set-up of the Orion chamber enables the use of 10 long pulse beams available, 5 from each side of the chamber. Beams could have been brought onto the target from either side, allowing the protons to probe through from the same side as the lasers or opposite to them. The latter was chosen for this experiment, therefore the protons are defocussed and deflected out into the expanded plasma.

When processing the results from the RCF several steps were taken. Firstly the images were enhanced using ImageJ's bandpass filter, where a fast Fourier transform is applied to the raw image to enhance the mesh and features within the image. These images are then analysed by observing the deflection of the grid lines, or width of darkened regions on the RCF. The deflections are used to calculate the magnetic or electric field strengths from Equations (3.4) and (3.5) respectively.

The nature of the Orion facility and the ability to have an average of 4 shots

per day meant that shots were not repeated. However, as a consistency check, we did repeat one shot and are able to show these shots give reproduceable data.

5.4.1 Single Spot Dynamics

Single spot dynamics were observed using proton radiography when a single laser of 400 J was focussed onto a 3 mm diameter, 5 μm thick copper disc. The proton radiographs are shown in Figure 5.7.

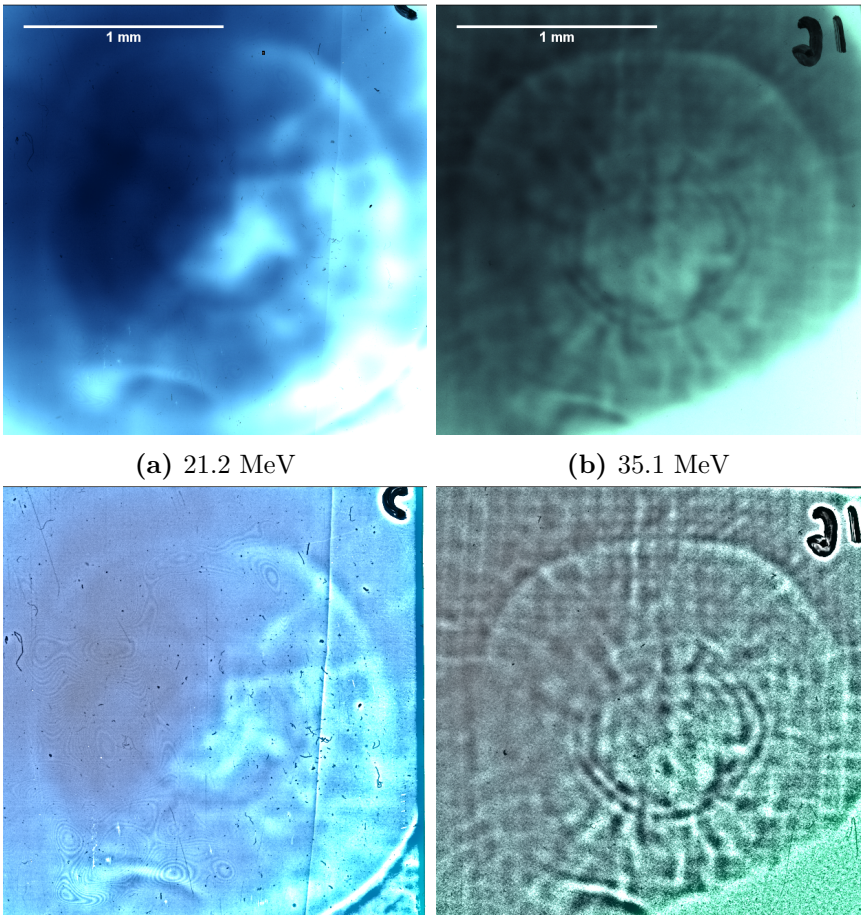

(a) 21.2 MeV **(b)** 35.1 MeV

(c) 21.2 MeV, enhanced image. **(d)** 35.1 MeV, enhanced image.

Figure 5.7: Single spot proton radiographs at 1 ns for two different RCF layers. The top row of radiographs are before any image analysis, and bottom row of radiographs after image enhancements have been made. The scales shown are those at TCC.

Surrounding the laser spot are two noticeably darker rings of increased proton dose. The ring structures are measured to be of approximately (730×710)±30 μm and (1720×1640)±30 μm in diameter (at TCC) for the inner and outer rings, respectively. The inner ring diameter in Gao's experiment was seen to vary with the proton energy, however from our single spot results and the difficulty in determining the inner ring diameter outline at lower proton energies, we cannot confirm this same

trend. Gao's probing direction was also opposite to that used at Orion, therefore magnetic fields created around the laser spot have a defocussing effect and emptying of the laser spot region instead of the observed focussing, and darkening of spots, perhaps enabling this observation.

Gao observed that the inner ring changed very little with time, something we also observed within our experiments for both single and double laser spots on target. Measuring the ring sizes at 1 ns for a double spot becomes a lot harder due to the appearance of several curved lines in between the two spots. However, the inner ring can be measured from the single spot radiographs as 800±30 μm in diameter, fairly similar to that observed in the double spot radiographs. The deflection of the protons being dependent on $1/\sqrt{E_p}$ means the magnetic field is the most dominant field affecting the protons in this region. The inner ring for the higher proton energies is 750±30 μm in diameter, which is almost 4 times that of the focal spot of the laser (220 μm). We are able to use this to calculate that the magnetic fields on the edges of a laser spot are 160±30 T. The shape of the rings are also close to circular, with vertical and horizontal diameters across being within ±50 μm, even though the laser focal spot was elliptical.

Diameter of ring at TCC	10.1 MeV	21.1 MeV	28 MeV	35.1 MeV	41 MeV
Inner Ring (μm)	/	/	(630×600) ±30	(690×670) ±30	(740×740) ±30
Outer Ring (μm)	(1800×1700) ±30	(1700×1700) ±30	(1700×1600) ±30	(1700×1600) ±30	(1700×1600) ±30

Table 5.1: A table of the dimensions of the rings observed within the single spots. The measurements are taken at TCC.

The outer ring sizes are more clearly defined and constant in diameter across the different proton energy radiographs, and are double the size of the rings formed when there is a second laser beam on the target (Figure 5.8). The constant diameter across radiographs shows that the deflection is a combination of the electric and magnetic fields. Within the central laser spot region the deflections are dominated by the strong magnetic fields, and it is only outside this region, closer to the edges

of the plasma that the electric fields have noticeable effects on the structures that the protons map. When electric fields deflect the protons it is in the same direction as the magnetic fields, out towards the edges of the spot, resulting in a larger net flux of protons being deflected.

The addition of a second laser beam does show that the expansion of the magnetic fields is affected and the outer ring expansion seems to be much smaller than with a single beam. The regions of the laser spots away from the colliding material in between the two is also affected suggesting that perhaps there is some transfer of information or net change to the overall dynamics of the magnetic field expansion with the addition of the second spot.

Using our results and those presented in published literature we are able to draw several conclusions on what generates the ring structure. Initially, fields will be created around the laser spot by the Biermann battery effect, due to temperature and density gradients. These fields surround the spots in an azimuthal orientation and grow with time, expanding across the target surface within the plasma [140]. Fields will also be created at the edge of the bulk plasma, where gradients exist. At the edge of the laser spots, the fields are carried to higher density regions by hot electrons and towards low density regions by bulk plasma. These two flows concentrate the magnetic fields at the boundaries and can create multiple rings within the outer ring.

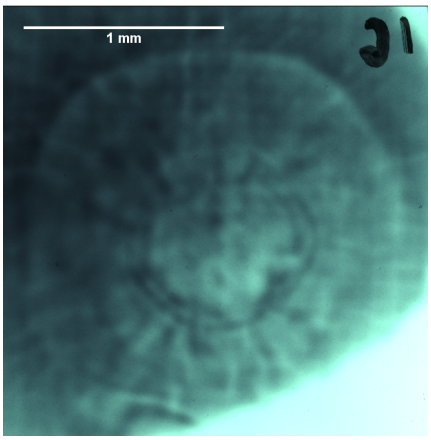

(a) A single laser spot for 41 MeV protons.

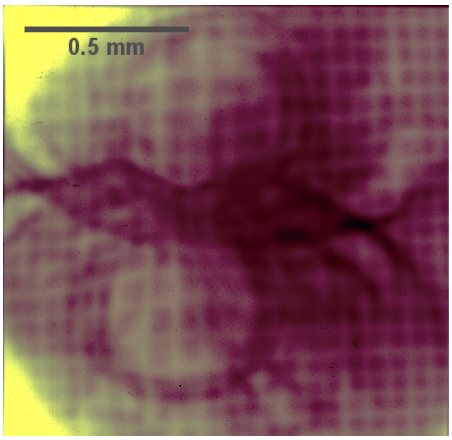

(b) A double laser spot for 38.8 MeV protons.

Figure 5.8: Proton probing of a single spot and double spot on a 5 μm copper target at 1 ns, demonstrating the differences in adding a second laser beam.

5.4.2 Proton Radiography Face-on

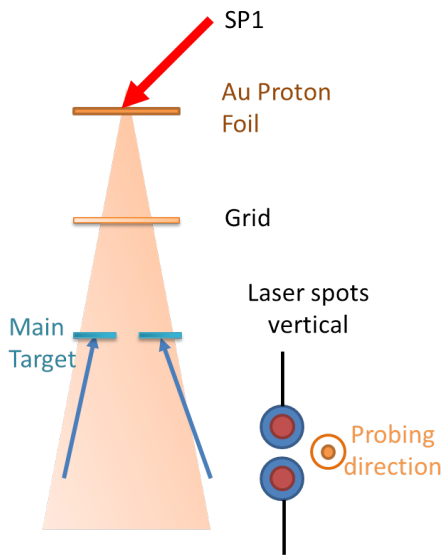

Figure 5.9: A diagram of the set-up for the protons probing through two discs face-on. The probing direction across the two vertically separated discs is seen in the smaller insert.

When the laser beams are focussed onto two parylene-D, 400 μm diameter discs using the configuration shown in Figure 5.9, results, as shown in Figure 5.10, are obtained. Marked on to the radiographs are the axes, which will help to put together a 3-dimensional understanding of the different orientations and measurements of plasma movements. The z and x direction are in the plane of the targets, where x is horizontal and z is vertical across the targets. The y-axis is the direction perpendicular to the target's surface.

The radiographs were taken at 0.2-0.5 ns intervals to show the development of the magnetic fields around the spots and also the movement of an early-time electric field. Figure 5.10 shows the two targets suspended by thin carbon rod stalks 0.2 ns after the start of the long pulses. There are nodules where the target stalks meet the discs, due to the presence of glue. It is also possible to see a shadow from the F mount in the data, which holds the discs in place. Around the laser spot are magnetic fields which will cause protons to be deflected radially outwards, away from this region, causing the two inner, white discs with darker rings. The fields within the focal spot also act like a lens, magnifying the grid at early times. Surrounding the two darker rings is a much wider, white ring region, where protons have been deflected, and the grid squares are magnified in this region. This could be due to hotter electrons streaming ahead of the bulk plasma. These hotter electrons will

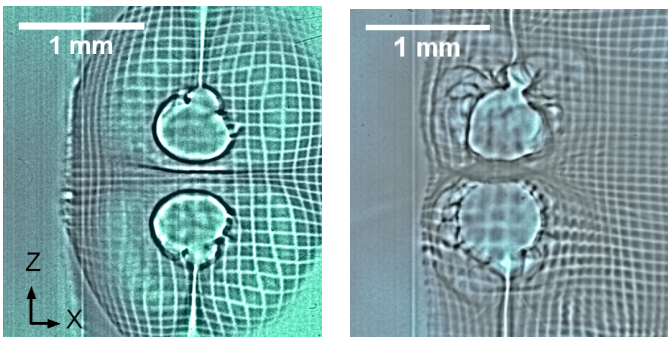

(a) 0.2 ns

(b) 0.5 ns

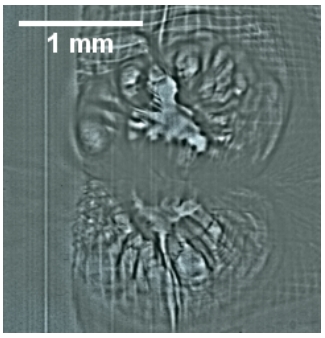

(c) 1 ns

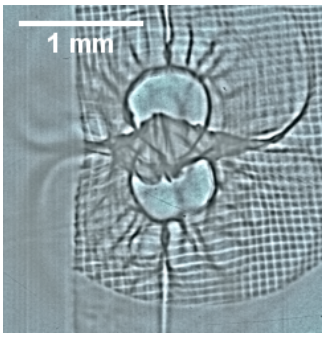

(d) 1.5 ns

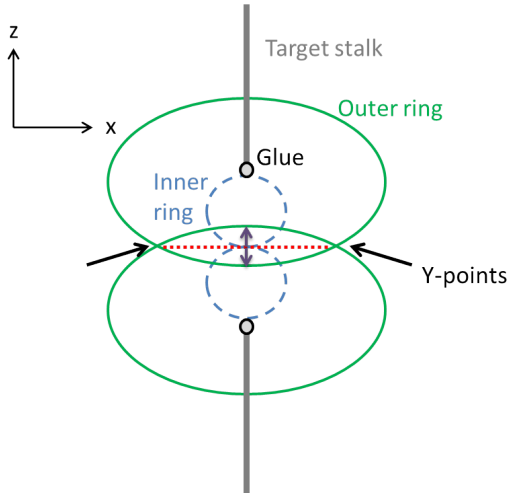

(e)

Figure 5.10: Proton radiography face-on to the main interaction taken on 4 separate shots with 17.4 MeV protons. Figure 5.10e highlights key features observed in the radiographs.

carry with them a magnetic and electric field, and so the deflection of the protons will be due to both fields. It is challenging to fully deconvolve the electric and magnetic field contributions at this time. The plasmas have not collided between the two spots yet, although there is some darkening of the region between them.

By 0.5 ns the two plasmas have started to come closer together and overlapping circle outlines are seen in the central region. However, the overlapping of the features does not indicate the fields and plasma have collided, as the expansion of the protons,

once they are slightly deflected, will continue on their trajectory at an angle beyond the interaction region and can still overlap and create this image. The protons in this region are also fairly smoothed, apart from the overall outlines, which further supports the fact the protons are overlapping beyond the target. The grid appears to be further magnified within the inner discs as well, suggesting increasing fields.

By 1 ns the plasma and fields have collided, as can be seen from the joining of the two spots in the image, and small features appearing within the central region and not being smoothed out as happened at 0.5 ns. In between the two spots is a wider, darker region where protons are being deflected into. The length across the colliding central region between the spots, in the x-axis direction as shown by the red line in Figure 5.10e, is consistently measured as 1.4±0.1 mm across the different proton energy radiographs. This gives us an estimate for the current sheet length which can be used in later calculations. At the edges of this region the outer bubbles from the two spots also seem much clearer with darker edges, creating 'Y' points, suggesting that the field is also strengthening in these regions as the plasma stagnates. More structure is developing near the outer edges of the plasma, possibly due to turbulence or an instability. The grid features within the disc are smeared out now due to turbulent plasma expansion.

At 1.5 ns we still have a colliding plasma in the centre, however the central region is decreasing in width towards the outer edges and takes on a more diamond-like shape. The structures within the outer rings of the spots also are becoming more uniform and darker spokes around each spot run radially outwards. There are some darker spokes that exist in the central region as well. We also find at > 1 ns that the Y points of the central region are further pronounced. The length, in the x-axis, of the central region has also expanded to 2±0.1 mm.

5.4.3 Proton Radiography at 45°

The results from probing at 45° use the set-up shown in Figure 5.11. Protons deflection is by both the electric and magnetic fields. Figures 5.12a and 5.12b show the results from using the set-up when the protons and the lasers are incident on the targets from the same side (Figure 5.11a) and the protons are deflected out of the laser spots by the magnetic fields. The 2.5 ns proton radiograph shows a longer,

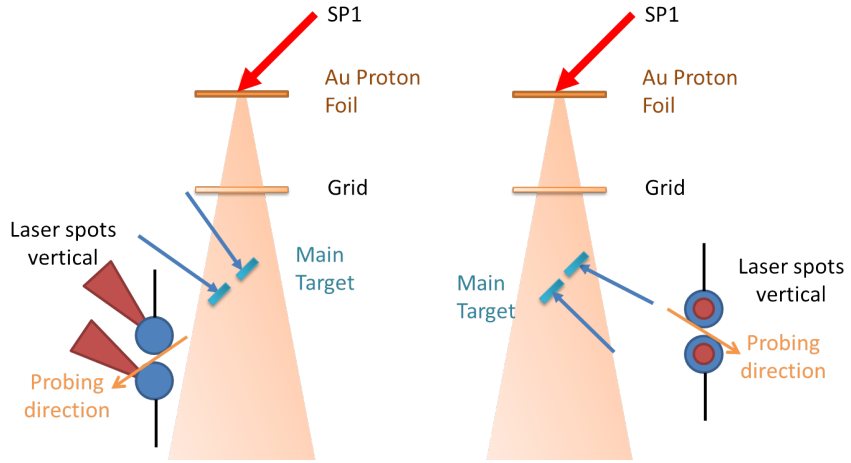

(a) Protons and lasers are incident from the same side.

(b) Protons and lasers are incident from the opposite side.

Figure 5.11: Set-up for the proton probing when the target is at a 45° angle to the proton beam. The inserts show the probe direction across the two, vertically separated discs.

dark region in between the two spots. This confirms that the fields are still present and deflecting the protons after the lasers are switched off. It is also possible to see a vertical line through the central dark region, similar to the dark spoke lines seen in Figure 5.10d. When we reverse the direction of the protons through the interaction, the radiograph shows that the protons are deflected out of the central region, and into the laser spots, shown in the radiograph in Figure 5.12c. This confirms that magnetic fields are the dominant field in the central region, due to the deflection direction being dependent on the direction of the protons. There is very little other quantitative information we are able to extract from the radiographs in this orientation due to the complexity of the images.

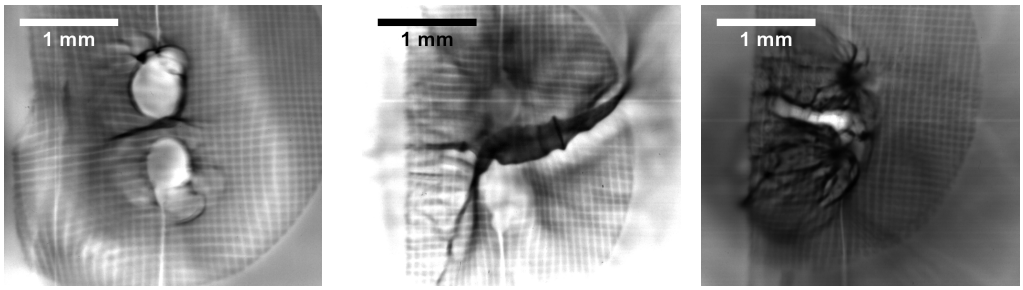

(a) 1 ns, protons and lasers are incident from the same (right) side.

(b) 2.5 ns, protons and lasers are incident from the same (right) side.

(c) 1 ns, lasers are incident from the left and the protons probe through from the opposite side.

Figure 5.12: Proton radiography images, where the proton beam is probing at 45° to the target surface. These proton radiographs are with protons of 17.4 MeV for 5.12a and 16.2 MeV for 5.12b and 5.12c.

5.4.4 Proton Radiography Side-on

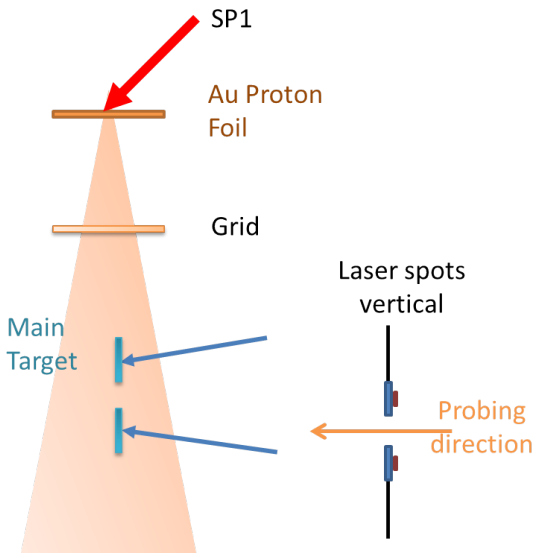

Figure 5.13: Set-up for proton probing side-on to the two, vertically separated target discs.

Side-on proton radiographs of a reconnection region were recorded using the set-up shown in Figure 5.6b where two lasers were aligned in the vertical direction. In this orientation we anticipate that the electric fields will be the dominant cause of proton deflections due to the small $\mathbf{v} \times \mathbf{B}$ component in this direction compared to the $q\mathbf{E}$ deflection.

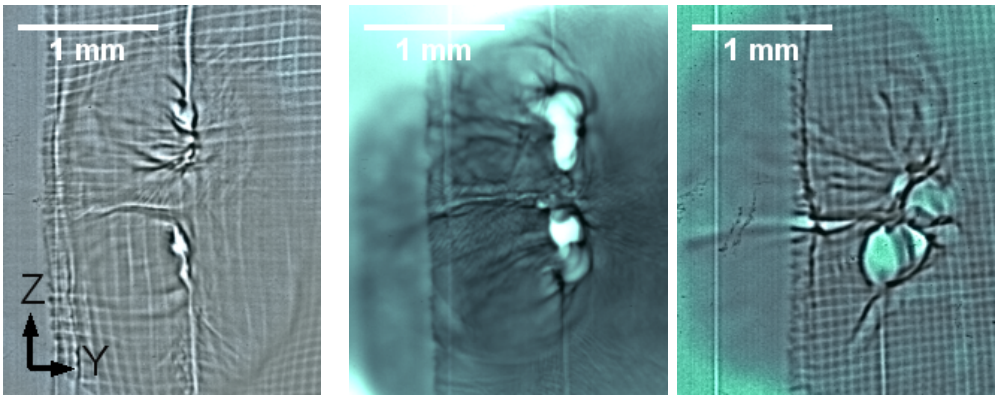

(a) 0.5 ns **(b)** 1 ns **(c)** 1.5 ns

Figure 5.14: Proton radiography images, side-on to the main interaction probed with protons of 15.6 MeV. In the radiographs the laser is incident from the left side. The grid is also absent in Figure 5.14b.

At early times (0.5 ns) the radiograph shows that the two plasmas and fields have not yet collided. However by 1 ns the two have started colliding and a narrow feature between the two spots empties of protons due to the electric field deflections. Protons are also deflected out of the region of the targets, due to the electric fields

creating voids which are larger (210 μm in width) than the actual width of the targets (25 μm). However the outline of the targets at 1.5 ns in Figure 5.14c suggests that one of the targets was rotated on its axis by a small angle, as the top and bottom targets do not have the same target width devoid of protons. This increases the uncertainty of electric fields measured from this radiograph.

5.4.5 Proton Radiography of Horizontal Spots Side-on

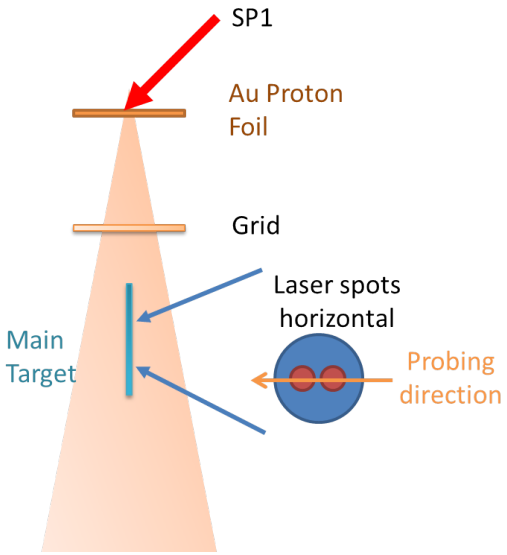

Figure 5.15: A digram of the set-up for proton probing across a single 3 mm target disc where the laser spots are separated horizontally.

A side-on projection of the target was also probed, similar to that in Section 5.4.4. The two laser spots were aligned horizontally on to a single 3 mm disc. In the proton radiograph the spots appear from the side as just one spot, one behind the other. This configuration, shown in Figure 5.15, is used to observe jets which, if present, would propagate in the vertical direction. Data taken between 1 and 1.5 ns is shown in Figure 5.16. At 1 ns it is possible to see the clear expansion of the plasma from the front side of the target. By 1.25 ns there is also expansion from the rear side of the target. The front side of the target also now has fields which are lifting from the target surface and curving at the ends. These fields would be expected, as shown by Gao [136], to form along the edge of the laser spot and the edge of the plasma expansion, lifting slightly from the target surface as the plasma expands out. At 1.5 ns the target appears to be curving even further and the expansion from the rear side is growing. The field of view from this radiograph, however, is limited by

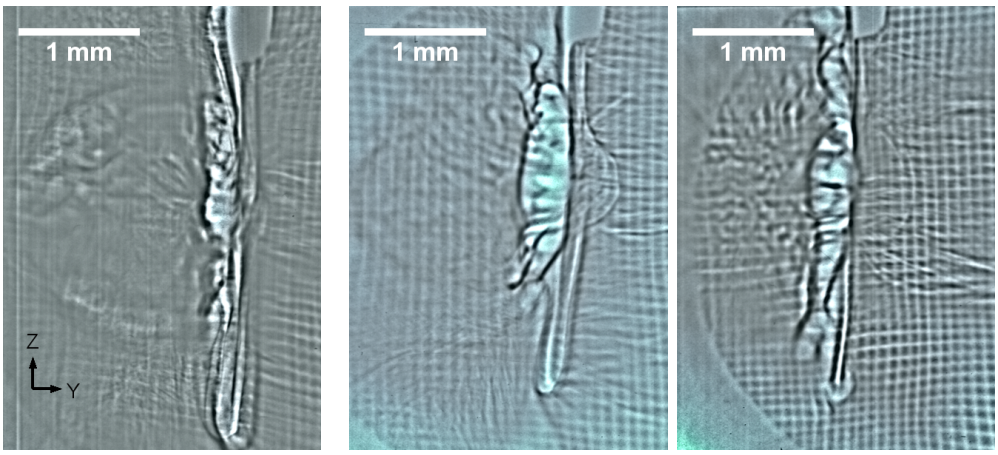

(a) 1.0 ns **(b)** 1.25 ns **(c)** 1.5 ns

Figure 5.16: Proton radiography images, side-on to the main interaction with two laser beams aligned side by side horizontally. The lasers are incident from the left side of the radiographs. The proton energies are 17.4 MeV for radiographs 5.16a and 5.16c and 16.7 MeV for radiograph 5.16c.

clipping of the circular proton grid. Jets are not observed from these radiographs either.

5.4.6 Measurements from Proton Radiographs

The different layers of the RCF can be used to see how the deflection varies with energy and therefore work out which field is the major contributor to the deflection. Equations (3.4) and (3.5) are used for calculating the magnetic and electric fields, respectively, and integrates the path a proton takes through them. This is approximated by using some scale length relevant to the fields in the plasma. The scale lengths assumed for each time are given in Table 5.2. The scale lengths were extracted using $L_B = n_e/\nabla n_e$ from simulations for magnetic fields and from the observed expansion of the plasma for the electric fields.

Firstly, the face-on radiographs, shown in Figure 5.10, can be analysed to extract magnetic fields. The magnification of the grid squares at the sides of the spots at 0.2 ns give the magnetic fields to be 20-30±5 T. In between the two spots we can also see deflection of the grid squares into each other. This would suggest higher fields in this region, however electric field effects are likely to be also adding to the deflections due to a build up of the electrons colliding between the spots. For this reason the grid deflections at the sides are used to give an estimate of the fields.

At 0.5 ns due to the magnification of the grids, especially within the laser

spot, the fields are estimated to have grown to 45±5 T.

By 1 ns the plasmas from the two spots have advected further outwards with a flow velocity of 1200±200 km/s in the z-axis direction and collided, creating a central, darker region between the two spots. The width of this darker region allows us to calculate the magnetic field as 55±5 T. This is generally in good agreement across the different energy proton radiographs, where the width becomes narrower with higher the proton energy. These magnetic fields strengths are calculated from half the width of the darkened region in between the two spots, rather than the grid magnification, because the grid is more difficult to see at this time. The central feature can be used to measure magnetic field strengths as protons are likely being deflected from the edges of the spots, which have expanded and are approximately located in the centre of the darker region. This is a similar method for extracting the fields as that used by Rosenberg *et al.* [30] and also matches the fields measured from measuring the deflection of the grids when using this method on earlier time radiographs [141]. This means a proton deflected out from this edge, would be deflected into the region of the other spot, creating the slightly curved outer edges of the darker region. It is at 1 ns when we expect the fields to reconnect, as the fields and plasma collide and the fields reorganise.

At 1.5 ns the protons are still being deflected into the central region although the magnetic fields are approximately constant with 50±5 T measured at the widest part of the central, diamond feature. The plasma flow velocity is still high at 1000±200 km/s in the z direction, as noted in the radiographs. We are also able to see dark, spoke-like lines within the central region, similar to what would be expected from a plasmoid, which are magnetic islands that can form in the current

Time	0.2 ns	0.5 ns	1 ns	1.5 ns
B (T)	25 ±5	45±5	55±5	50±5
dl_B (μm)	100±25	150±25	350±25	450±25
E (V/m)	/	/	(9.4±1.5) $\times 10^7$	(9.2±1.5) $\times 10^7$
dl_E (mm)	/	/	1±0.25	2±0.25

Table 5.2: A table of the different magnetic field (B) and electric fields (E) measured at various times, using appropriate scale lengths.

sheet [142]. There are other filaments observed surrounding the spots, potentially due to Weibel [143] or the magnetothermal [144] instability which could also generate the spokes, so without further analysis no conclusions can be made about this feature.

The side-on proton radiographs shown in Figure 5.14 suggest electric field strengths of (9.4±1.5) × 10^7 V/m calculated from the width of the central, thin void between the two discs. This grows in width and length and by 1.5 ns it is 1.90±0.25 mm long and of approximately the same magnitude of field strength to that measured at 1 ns.

The size of the plasma bubble and, therefore, the distance electric fields are experienced over can be measured from the plasma expansion in both the face-on and side-on radiographs. The electric field strengths are of a similar order to that calculated in other side-on proton probing experiments [145, 140]. In Figure 5.14a, at 0.5 ns, the plasma has expanded to 1.10±0.25 mm from the targets. It is harder to see at later time how far the plasma has expanded due to the 'F' mount shadow, however an estimate of 1.80±0.25 mm can be made from 1 ns. This suggests that the plasma is moving away from the target surface at a velocity of 2200±200 km/s at 500 ps, decreasing to 1600±200 km/s by 1 ns.

We can also observe, from Figure 5.14, using horizontally separated spots, and probing side-on, that the plasma is also expanding at 1500±200 km/s at 1 ns which is close to the 1600±200 km/s measured from the vertically separated spots in a side-on projection, shown in Section 5.4.4. At 1.5 ns, seen in Figure 5.16c, we are unable to distinguish the outer edge of the expanding plasma.

These velocities of the plasma movement from radiographs of similar energies (~15-17 MeV) are summarised in Table 5.3. The velocities, in general, are in close agreement. There are differences due to different laser energies on shot as well as the measurements made from some radiographs being more difficult to extract than others. The expansion for the z-axis direction is calculated from the free expansion of the plasma out along the target stalk direction (i.e upwards for the top disc and downwards for the bottom disc), not from the middle of the spots where the two plasmas collide. The velocities will enable comparisons with both interferometry data and simulations. Calculations can also be made of parameters dependent on

Time	x-axis velocity (km/s)	y-axis velocity (km/s)	z-axis velocity (km/s)
Face-on			
0.5 ns	1600±200	/	1600±200
1 ns	1100±200	/	1200±200
1.5 ns	800±200	/	1000±200
Vertical spots side-on			
0.5 ns	/	2200±200	1400±200
1 ns	/	1600±200	1000±200
1.5 ns	/	1400±200	950±200
Horizontal spots side-on			
1 ns	/	1500±200	1000±200
1.25 ns	/	1300±200	700±200
1.5 ns	/	/	700±200

Table 5.3: A table of the approximate velocities of the plasma movement measured from the proton radiographs in different directions, given by the axes drawn onto the proton radiographs.

plasma flows, such as the plasma-β.

5.4.7 2D Interferometry Results

The optical probe had several cameras collecting data images. Gated, optical cameras took single frame images at 4 different intervals on a single shot and were primarily used for calibrating the fringes per mm on the streaked interferometry. The streaked interferometry camera was used for inferring plasma velocities after the main beams were switched off.

The interferometry started before the main lasers were switched on and the interference lines at this early time are used as a reference. Light from the main lasers affected the streaked interferometry up to 1.5 ns after the main lasers were switched on. This is seen from the bright streak of light running through the data. After the lasers are switched off plasma material is seen moving by the shifts in the interference lines. The streak camera is aligned to have the spatial view horizontally, between the two discs. The camera measures the plasma flow across this region, as shown in Figure 5.17.

In the face-on interferometry (Figure 5.17a) there are several shifts in the lines

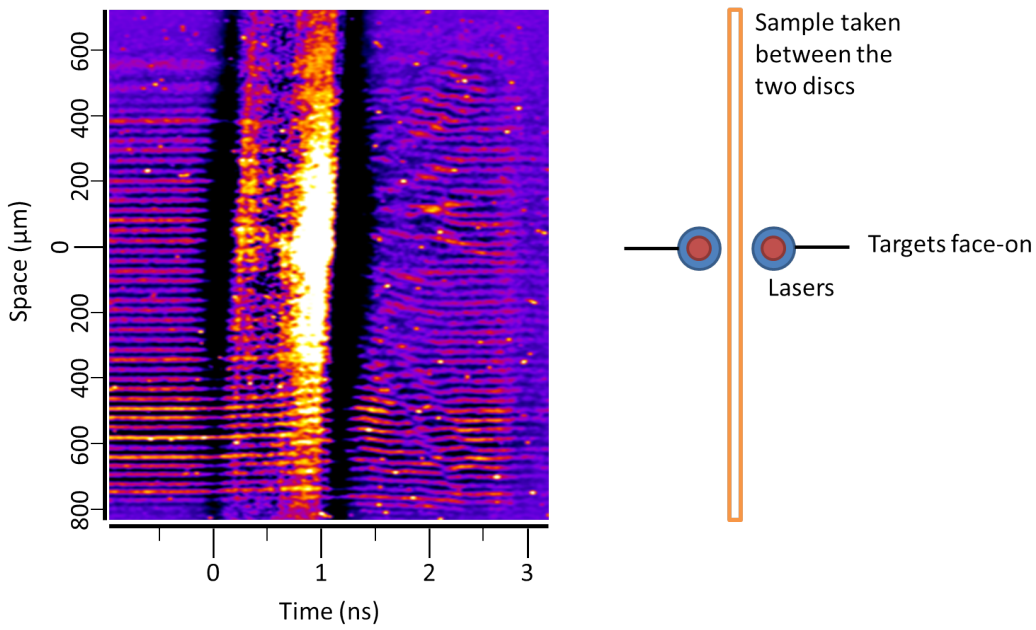

(a) Face-on interferometry.

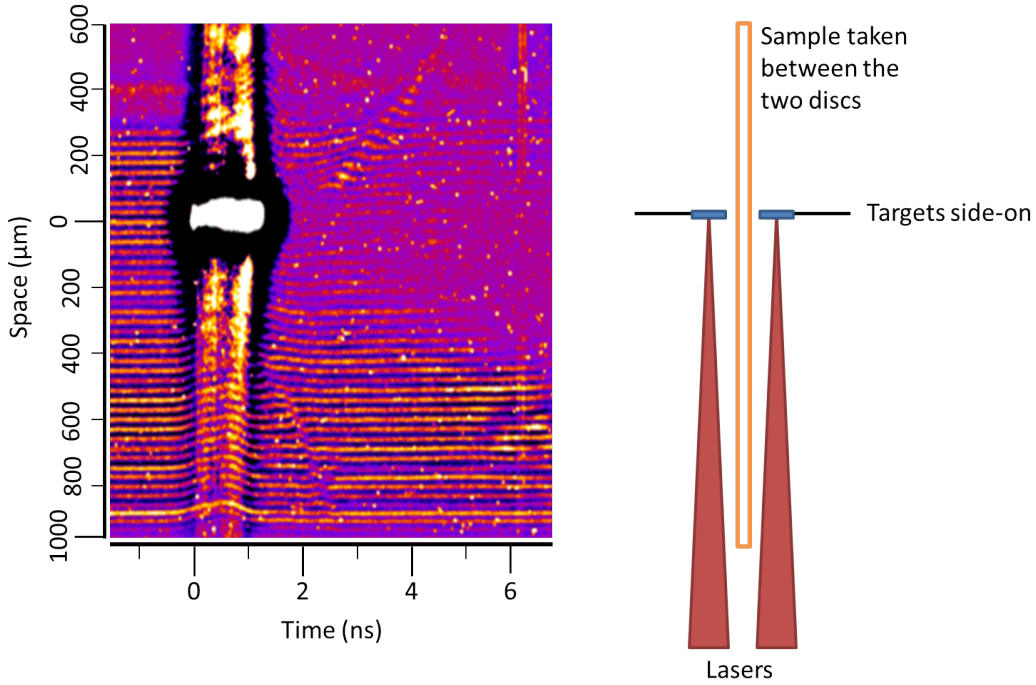

(b) Side-on interferometry.

Figure 5.17: 2D images from the streaked interferometry. The vertical axis gives the spatial direction and horizontal is the temporal axis. The spatial slit is aligned between the two discs, as shown by the orange box such that the light is spatially integrated across the width of the box.

after the main lasers are switched off. The origin of the spatial scale corresponds to the central point between the two discs. The different gradients of the lines moving outwards, away from the centre, mean that there are several plasma regions moving

with different velocities. It is the plasma at the outer edges in the interferometry image that are moving with the greatest velocity and are also some of the clearest shifts to measure.

The side-on interferometry (Figure 5.17b) shows just two distinct shifts to the fringes. There is one shift that moves outwards from close to the central point and upwards in the image of the interferometry. This direction corresponds to plasma movement behind the targets which has a shallower gradient, indicating a slower velocity than the shift located in the lower half of the image. The shift in the lower half of the image corresponds to plasma moving in front of the two targets. The early time movements from the front side move at 430±60 km/s and are visible almost immediately after the main lasers are switched off. The plasma movement in the top part of the image in 5.17b moves at a slower velocity of 280±60 km/s behind the two targets.

The outer shifts in the face-on interferometry are observed from 1.5 ns onwards and start at 0.7 mm from the centre of the discs, moving at velocities of approximately 400-600 km/s. There other small shifts of lines in between these two movements as well, although little information can be gained from these without additional enhancements of the images in this region.

The slight differences in the measurements of the velocity of the plasma out from the front and from the sides in the two interferometry images could be due to the plasma moving at an angle. When plasma is moving at an angle it results in lower velocities being recorded after being projected in either the face-on or side-on orientations. These plasma velocities agree with the late time velocities recorded from the radiographs.

5.5 Gated X-ray Detector Results

The GXD was used to check laser focal spot separation and the size of the spots. Figure 5.18 shows the image captured by the GXD. There are 16 images projected by the 16 pinholes situated on the front of the nose of the camera. These are recorded by the camera as it sweeps across the length of each of the 4 channels. It is seen from the GXD images that the spots appeared fairly uniform and circular in shape.

The spot separation was generally accurate to ±50 μm. The size of the emitting region was 424 × 400 μm.

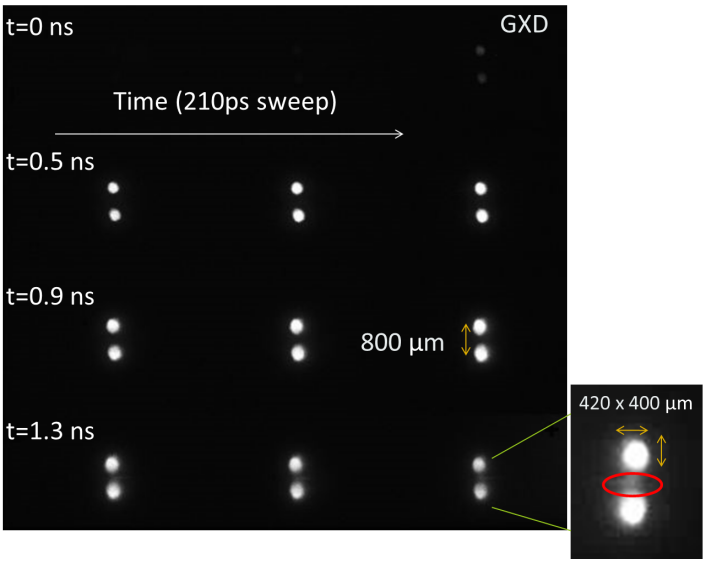

Figure 5.18: An image from the GXD of a copper target, with a dimmer emission line observed between the spots at times >1 ns.

The GXD also recorded a dim line of emission between the spots for copper targets at times >1 ns, as is shown in Figure 5.18. This rise in emission is assumed to be due to the temperature increasing during the collision of the plasmas.

5.6 Spectrometer Results

The spectrometer used on the experiment has been described in Section 3.6. The spectrometer records spectral lines emitted from the chlorine K-shell which the plastic targets were doped with. The spectra gives both spatial and temporal information about the temperature and density of the laser spots and an example of the data is given in Figure 5.19.

In Figure 5.19 two rows of spectral lines from the two vertically separated laser spots are seen. The width of each row gives spatial information. The width across each spot are also measured to be larger in size (~500 μm) than the laser spots, showing the plasma has expanded. The region between the two spots is where the reconnection is expected to occur.

Corrections, due to filtering etc., were applied to the lineouts taken across the spectra, as described in Section 3.6. The spectrometer collects spectral information

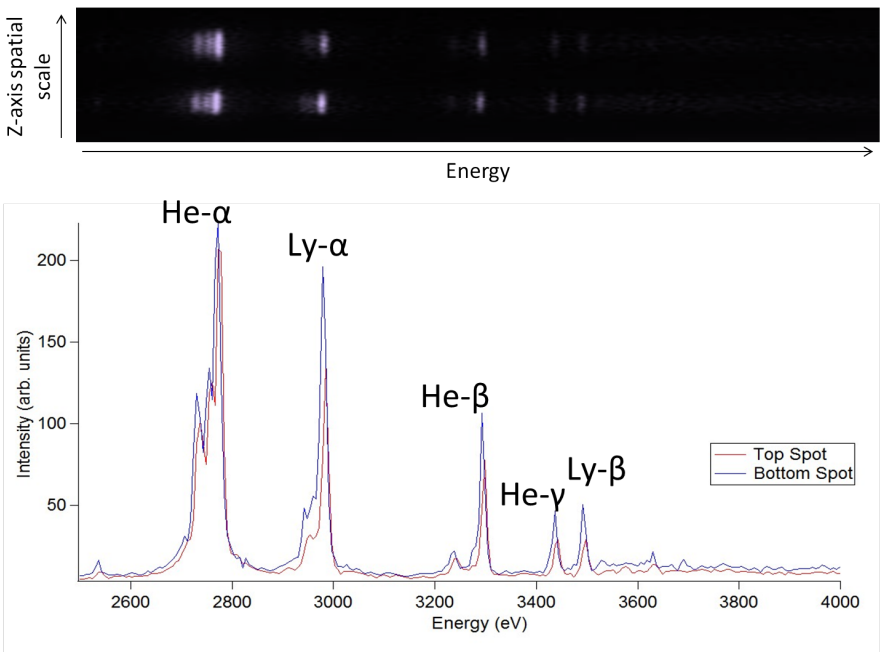

Figure 5.19: An example of the spectrometer data gained from the GXD spectrometer. The insert is what the spectral lines look like on one of the GXD strips. A lineout with a calibration applied gives rise to the spectral lines labelled on the graph.

Time (ns)	Temperature Measured (eV)	Laser Spot Energy (J)
0.3	282±70	230
0.75	920±70	330
1.1	1490±70	330

Table 5.4: A table of the temperature measurements at different times and laser energies on parylene-D targets.

at four different times on a single shot. Background X-rays from the short pulse are also collected by the spectrometer. As a result the useful spectral data is only gained for periods of time before the short pulse is used. Several shots have been analysed for the spectrometer data and the temperatures and times are shown in Table 5.4. The temperatures are taken using a 270 μm (18 pixel) sample spatially, over the centre of the spot. The emission between the spots is very weak and only a few lines are visible in this region, so we cannot infer a temperature for the reconnection region directly.

Using Equation (3.13) the temperature is extracted from the fit to the continuum emission at late time, as shown in Figure 5.20. Temperatures were measured for several different shots. For an energy laser of 230 J at early times the laser spots

are measured to have a temperature of 0.282±0.07 keV. For shot energies of 330 J at 1.1 ns the temperature increased to 1.49±0.07 keV. The measurements made from the spectrometer show a dependence of the temperature on the laser energy, as would be expected.

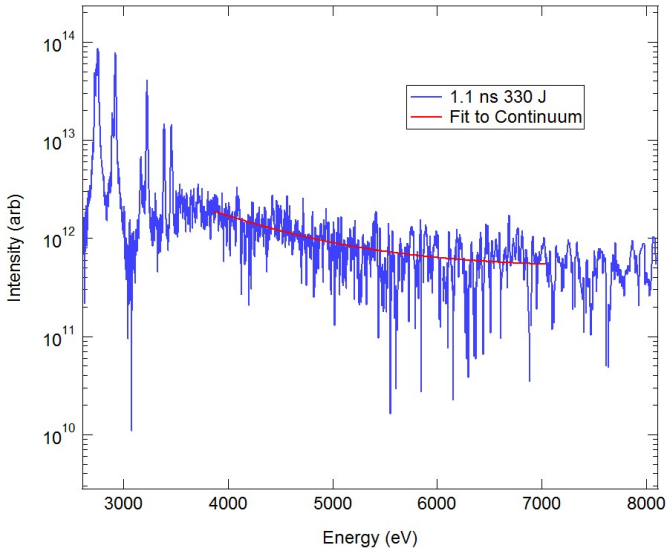

Figure 5.20: A graph of the signal after corrections have been made for the spectral response of the spectrometer components. A fit is applied to the continuum emission as shown by the red line, yielding a temperature measurement of 1490 eV.

These temperatures also support the electric fields measured by the side-on radiography given in Section 5.4.4 to within an order of magnitude. The electric field can be estimated from the temperature using Equations (5.1)-(5.2), which are found from the electron equation of motion [79],

$$P = n_e k_B T_e \tag{5.1}$$

$$n_e e E = -\frac{dP}{dx} \tag{5.2}$$

which approximates to

$$E = -\frac{k_B \nabla T_e}{e} \tag{5.3}$$

The temperature gradient within the plasma in the direction away from the target is small (~1 keV/mm), and so electric fields in this direction will be of the order 10^6 V/m compared to the order of 10^7 V/m measured from the radiographs.

5.7 Simulation Results

Simulations from IMPACTA [38, 115] model the field dynamics occurring under similar conditions to this experiment. IMPACTA is a 2D, Eulerian code based on the VFP equation and is an evolution of the IMPACT code [38]. IMPACTA adds the second order terms from the VFP equation, as well as magnetic fields, in a plane. The code has been shown to reproduce classical transport in the appropriate limits and has been modified to work with reconnection geometries [65].

The simulation is set-up using a box of 200×1500 μm with two Gaussian laser spots 200 μm apart. The simulation is modelled for a smaller spot separation than that used in the experiment to reduce the time and computer processing needed. However, the conditions that are generated by the simulation are still representative of those we observe in the experiment, with a ~1 keV electron temperature, and an electron density of $1{\times}10^{21}$ cm^{-3} in the laser spot region.

The results of the simulation are shown in Figure 5.21. These diagrams show the magnetic fields at various times, taken from ≈ 250 μm off from the target surface. As the plasma meets in the centre, between the two spots, the field strengths start to increase. The colliding region extends further out in the x-direction as time progresses, and the fields at the edges of the reconnection region also strengthen (at the 'Y' points). This is similar to that which we observe in the experiment.

Nernst effects and anisotropic pressure terms are also included in the simulations and the importance of both of these are demonstrated by the graph in Figure 5.22. The graph shows two lines of the magnetic fields measured in the central region from simulations which include anisotropic pressure effects (red line) and another which does not include these terms (blue line) [147]. The magnetic field without anisotropy is shown to increase rapidly to high magnetic fields, and then decrease after about 2 ns. The inclusion of the anisotropic term allows the magnetic fields to evolve to weaker strengths, similar to those measured in the experiment. This is due to not restricting the electrons to flow in the same direction out from the spots, such that they will not pile up in the central region.

Modelling using NYM, a 2D Lagrangian hydrocode [114] from AWE, shows the dependence of the plasma conditions on the laser energy. Some of these simulations

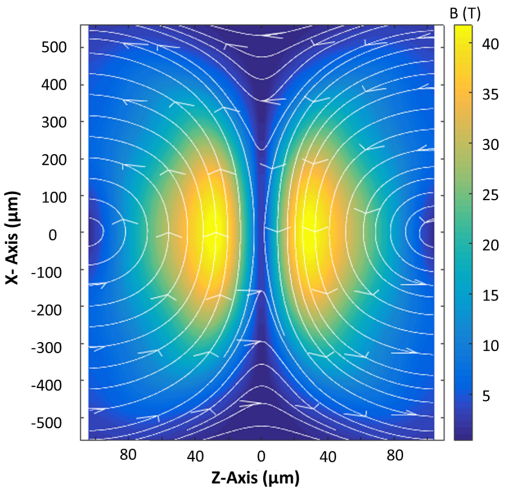

(a) 500 ps

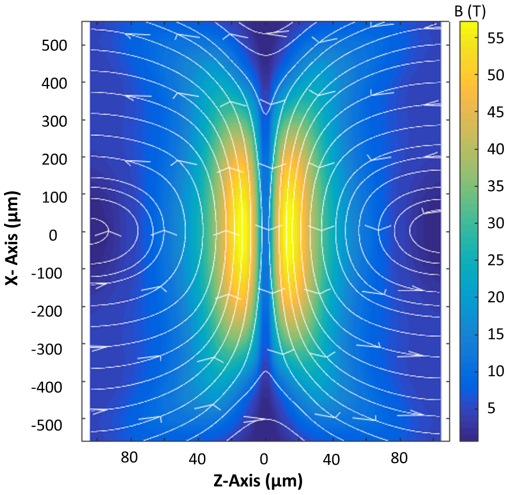

(b) 1 ns

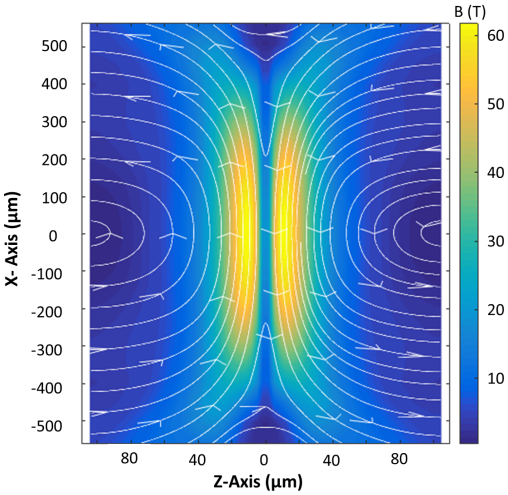

(c) 1.5 ns

Figure 5.21: Simulations of the magnetic fields produced from IMPACTA. Field strengths are taken at various times and at $y \approx 250$ µm [146].

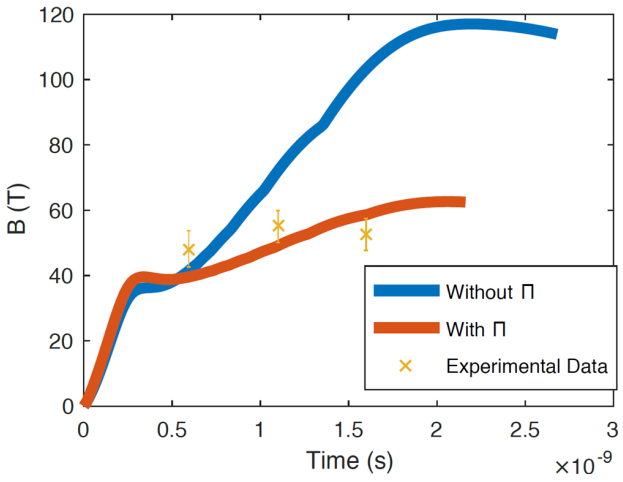

Figure 5.22: A graph of the magnetic field strength near the reconnection region when modelling with anisotropic pressure terms (red line) and without (blue line).

at 1 ns for the plasma density and temperature are shown in Figure 5.23. The NYM simulations help to interpret our data. The code is set-up to model a reconnecting plasma using a pseudo void of 1.4×10^{-5} g/cc of parylene-D between the foils, and 1500 µm in front of the target surface. Comparing the results of having single beam with no boundaries and the addition of a pseudo void show that there are not large

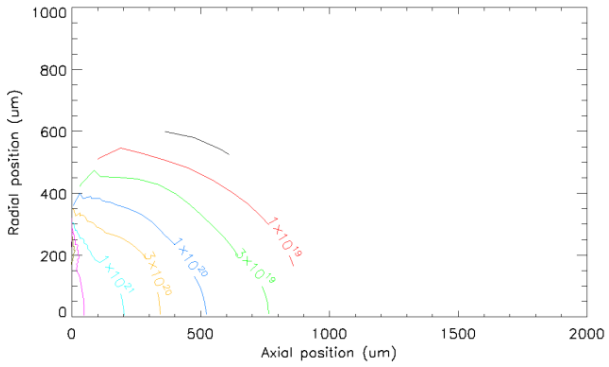

(a) Electron density (cm^{-3}).

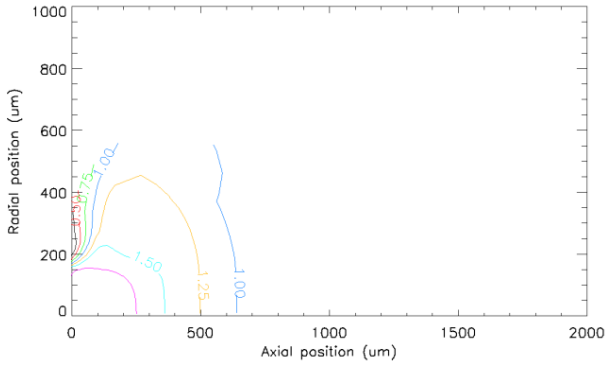

(b) Electron temperature (keV).

Figure 5.23: Simulations from NYM of conditions created by a single 400 J laser spot on a 25 µm parylene-D target at 1 ns [148].

differences in the conditions in the central region, so the single beam cases are shown in Figure 5.23.

The experiment used laser energies between 200-400 J. Modelling shows that for spots of 400 J on the plastic discs T_e would be 1.75 keV and n_e would be $3{\times}10^{21}$ cm^{-3} by 1 ns. For spots of 250 J the T_e would be 1.25 keV and n_e would be $3{\times}10^{21}$ cm^{-3}. The hydrodynamic simulations for the temperatures are a reasonable match to those measured in the experiment. The IMPACTA simulations, using the NYM parameters, also give good agreement with the magnetic field strengths generated by such a plasma.

5.8 Measurements from the Experiment

The simulations performed for this experiment using IMPACTA suggest under the conditions created by the laser and target magnetic reconnection should occur. In the proton radiographs we have observed the two plasmas colliding and strong (≈55 T) magnetic fields being created. The plasma has a β of 100 in the central laser spot and of ~20 nearer the reconnection region. The higher values of β are similar to those commonly created in ICF environments, for example in holhraums.

In astrophysical plasmas $\beta \ll 1$ and collisionless reconnection occurs. This is dominated by the magnetic pressure. When $\beta > 1$ the thermal pressure dominates. However, β depends on n_e and T_e and as the plasma moves away from the focal spot and expands, the density and temperature decrease and β also decreases. The magnetic pressure then becomes more important. When β and β_{RAM} (where $\beta_{RAM} = \frac{1}{2}\rho V^2 / \frac{B^2}{2\mu_0}$) are much larger, magnetic fields in the system are not important in altering the processes. The magnetic fields in these environments will be driven together faster than reconnection can occur, and cannot break or reorganise so pile-up occurs instead. At plasma inflow velocities of 600±200 km/s plasma-β_{RAM} is ~50 near the reconnection region.

Various parameters relevant for a reconnecting plasma can be calculated, using both experimental and simulation data. The values quoted in the following sections are taken at 1 ns after the lasers were switched on, with ranges in their values depending on position either at the laser spot or in the coronal plasma between the

spots near the reconnection. These parameters are sensitive to the laser energy of each spot. The electron number density was $3{\times}10^{21}$ cm^{-3} at the centre of the spot and decreased to $1{\times}10^{20}$ cm^{-3} at the coronal regions. The electron temperature was measured on experiment to be 1.5 keV at the laser spot, which approximately matches simulation data for that same time (1 ns).

The flow velocities created on other experiments, with similar targetary and laser parameters to this experiment, are usually a few times the ion sound speed. The ion sound speed, as shown in Equation (5.4), is calculated as 101 km/s.

$$c_s = \sqrt{\frac{Zk_BT_e}{m_i}} \tag{5.4}$$

The plasma in between the two spots, is travelling at speeds of 6 times c_s, however this flow velocity is still less than the electron thermal velocity, Equation (2.10), calculated to be 1600 km/s.

It is possible that the Nernst effect is also advecting magnetic fields, especially at the start of the interaction when the bulk plasma expansion is slower. The Nernst velocity is estimated by Equation (2.33) using the temperature gradient across the spot as ~ 1 keV/200 μm and the thermal conductivity in the radial direction, $\kappa_\perp^c$, as 1, which is the case when $\omega_{ce}\tau_{ei} = 1$, as shown by Epperlein *et al.* [49]. This velocity is lower than that observed in the experiment, although very similar to the Alfvén velocity (89 km/s). However in early time, when the plasma expands quickly, the Nernst effect could be contributing to the advection of fields. Later in time it is the thermal electrons which move the fields together. The distance the spots are set apart (800 μm from centre to centre) would also be covered by electrons flowing at the Nernst velocity during the first 1 ns. We believe the reconnection to be taking place by 1 ns.

The electron-ion collision time, τ_{ei}, has also been used in the equation for the Nernst velocity, with this approximated as

$$\tau_{ei} = \frac{3}{4}\frac{\sqrt{m_e}T_e^{3/2}}{\sqrt{2\pi}n_eZ^2e^4\ln\Lambda} \tag{5.5}$$

The electron-ion collision time is ~$5.8{\times}10^{-12}$ s. In this equation the Coulomb loga-

rithm is taken as [33]

$$\ln \Lambda = 24 - \ln(T_e^{-4} n_e^{1/2}) \tag{5.6}$$

The Coulomb logarithm typically lies in the range 10-20 for weakly coupled plasmas and in our conditions it averages at ~ 8.

Unlike other reconnection experiments [28, 30], we do not see the production of jets as a signature of the reconnection event. We are able infer a reconnection event from the matching of experimental conditions to simulations and also the features observed around the colliding plasmas. If we did have jets being generated from the reconnection region the energy lost from the magnetic field energy, $B^2/2\mu_0$, would give rise to ions having an increase in energy of $0.5nm_iv^2$ = 89 km/s, which is much less than the expansion velocity of the bulk plasma. Therefore the jets would be difficult to observe while they are travelling within the wider plasma region. The exception would be for an electron jet produced which would have a much higher velocity.

5.8.1 Reconnection Evidence

When the two plasmas collide together, there are several different scenarios that could exist. The first of which is that the plasma will just build up in the centre and form a much denser central region, with perhaps some outflows to less dense areas. Another is that the field lines will rearrange, reconnect and redistribute both the fields and the plasma, and in some cases surplus energy will be released in a particle jet from the reconnection region. The plasma will start slowing down as it approaches the other, due to electric fields associated with collisions. The plasma will become more collisional in the central region where the two meet, as the flow speed drops and the density increases. The resistivity can increase and magnetic field lines diffuse across the central region and reconnect. As reconnection takes place, plasma is guided along 'outflow' regions, the plasma density will not keep increasing and the plasma-β reduces. Collisions increase the temperature in between the two plasmas, as observed from some GXD images where a bright line in between the two colliding plasmas is observed.

If it is magnetic energy being transferred into thermal energy, this would sug-

Parameter	Equation	Value
Average ion charge, $\bar{Z}$		4.3
Average ion mass, m_i		1.36×10^{-26} kg
Mass density, ρ		0.0003 g/cm^3
Ion density, n_i	$\rho/m_i = n_i$	2.21×10^{19} cm^{-3}
Electron density, n_e		1×10^{20} cm^{-3}
Magnetic field, B		55 T
Ion temperature, T_i		0.2 keV
Electron temperature, T_e		1.5 keV
Ion thermal velocity, v_{Ti}	$v_{Ti} = \left(\frac{k_B T_i}{m_i}\right)^{1/2}$	49 km/s
Electron thermal velocity, v_{Te}	$v_{Te} = \left(\frac{k_B T_e}{m_e}\right)^{1/2}$	1600 km/s
Ion gyrofrequency, ω_{ci}	$\omega_{ci} = \frac{ZeB}{m_i c}$	2.8×10^9 rad/s
Electron gyrofrequency, ω_{ce}	$\omega_{ce} = \frac{eB}{m_e c}$	9.7×10^{12} rad/s
Ion gyroradius, r_i	$r_i = v_{Ti}/\omega_{ci}$	17 µm
Electron gyroradius, r_e	$r_e = v_{Te}/\omega_{ce}$	0.16 µm
Ion plasma frequency, ω_{pi}	$\omega_{pi} = \sqrt{\frac{Z^2 e^2 n_i}{m_i \epsilon_0}}$	9.3×10^{12} rad/s
Electron plasma frequency, ω_{pe}	$\omega_{pe} = \sqrt{\frac{e^2 n_e}{m_e \epsilon_0}}$	5.6×10^{14} rad/s
Ion skin (inertial) depth, d_i	$d_i = c/\omega_{pi}$	30 µm
Electron skin (inertial) depth, d_e	$d_i = c/\omega_{pe}$	0.54 µm
Electron-ion collision time, τ_{ei}	$\tau_{ei} = \frac{3}{4}\frac{\sqrt{m_e}T_e^{3/2}}{\sqrt{2\pi} n_e e^4 Z^2 \ln\Lambda}$	5.8×10^{-12} s
Ion sound speed, c_s	$c_s = \sqrt{\frac{Z k_B T_i}{m_i}}$	101 km/s
Alfvén velocity, v_A	$v_A = \sqrt{\frac{B^2}{\mu_0 m_i n_i}}$	89 km/s
Nernst velocity, v_N	$v_N \approx \frac{2\tau_{ei}\kappa_\perp^c \nabla T_e}{5 m_e}$	90 km/s
Flow velocity, V		600 km/s
Current sheet length, L		700 µm
Coulomb logarithm, $\ln\Lambda$	$\ln\Lambda = 24 - \ln(T_e^{-1} n_e^{1/2})$	8.4
Spitzer resistivity, η	$\eta = 1.03 \times 10^{-}2 Z \ln\Lambda T^{-3/2}$	6.4×10^{-6} Ωcm
Lundquist number, S	$S = \frac{\mu_o L v_A}{\eta}$	1227
Magnetic Reynolds number, R_m	$R_m = \frac{\mu_o L V}{\eta}$	8268
Sweet-Parker width, δ_{SP}	$\delta_{SP} = \frac{L}{\sqrt{S}}$	20 µm
Electron plasma-β, β	$\beta = \frac{n_e k_B T_e}{B^2/2\mu_0}$	20
Plasma pressure-β, β_{RAM}	$\beta_{RAM} = \frac{\frac{1}{2}\rho V^2}{B^2/2\mu_0}$	44
Haines Number, H_N	$\frac{1}{5}\kappa_\perp^c \omega_c \tau_{ei} \beta$	≥ 10

Table 5.5: Various parameters for this experiment calculated in the region near the reconnection at 1 ns for parylene-D discs.

gest reconnection and this is expected to occur on the timescales of this experiment.

The Sweet-Parker timescales, by comparison, would give a time for the reconnection

to occur on the Alfvénic timescales (Equation (2.56)) $\tau_A \approx 8$ ns and on diffusive timescales (Equation (2.55)) of $\tau_{Diff} \approx 100$ ns. Even the shorter of these, from the Alfvénic timescales, predicts a timescale of much longer than the 1 ns we see the reconnection taking place on.

The width of the current sheet formed in the reconnection is determined by the resistivity, and therefore the collisionality of the plasma. Assuming the resistivity is described by Spitzer resistivity, (5.7),

$$\eta = 1.03 \times 10^{-4} T_e^{3/2} Z \ln \Lambda \ \Omega\text{m} \tag{5.7}$$

as might be expected for plasmas where $T_e \geq 10Z^2$ [33]. The resistivity, therefore, is $\eta = 6.4 \times 10^{-8}\ \Omega m$. This resistivity within the plasma allows the magnetic field to decouple from the electrons and ions. The lengths over which this occurs is given by the gyroradius of the electrons and ions, Equation (5.8) and (5.9).

$$r_e = v_{Te}/\omega_{ce} \tag{5.8}$$

$$r_i = v_{Ti}/\omega_{ci} \tag{5.9}$$

For the plastic targets the ion gyroradius is $\omega_{ci} = 2.8 \times 10^9$ rad/s and the gyrofrequency is $r_i = 17$ μm, and for electrons $\omega_{ce} = 9.7 \times 10^{12} \times 10^6$ rad/s and $r_e = 0.16$ μm. The gyroradius for the ions is larger than that for the electrons which is why they decouple sooner than the electrons. There is also the ion skin depth, which is given as

$$d_i = \frac{c}{\omega_{pi}} \tag{5.10}$$

and is approximately 30 μm.

The Lundquist number for astrophysical systems, such as the magnetosphere and in solar corona, is very large ($> 10^{13}$), whereas in this experiment the Lundquist number is ~10^3. It is much higher in astrophysical systems due to their long scale lengths and low resistivity. Here the scale length, L, is calculated from the length of the current sheet measured in the face-on proton radiographs, L= 700 μm at 1 ns. When systems have large Lundquist numbers they are more prone to breaking into magnetic islands due to the reconnection region becoming unstable, forming

plasmoids [149, 150]. This would create a similar signature to the lines in the reconnection region, seen in some radiographs. As yet this is not confirmed for these experiments and further analysis is needed. At the Lundquist numbers we have within the experiment, the reconnection event is expected to be stable. The magnetic Reynolds number is ≥5000 (the ratio of the resistive to flow pressures), which is higher than the Lundquist number, due to the flow velocity being ~3 times the Alfvén velocity and the magnetic fields being driven together faster by thermal flows.

Using the Lundquist number and the scale length of the plasma we can also predict a current sheet width from the Sweet-Parker model.

$$\delta = LS^{-1/2} \tag{5.11}$$

to give 20 μm. When the width of the reconnection region is larger than the ion gyroradius then the ions remain bound to the field within the reconnection and the reconnection event can be considered as a single-fluid reconnection process. However if the reconnection width is smaller than the ion gyroradius (17 μm), then two-fluid reconnection is considered. The reconnection width and the ion gyroradius are very similar in value and the electron gyroradius (0.16 μm) is much smaller. Therefore it is appropriate to also consider two-fluid reconnection for this experiment as the electrons will remain coupled to the magnetic field longer than the ions. Normally it is only when $\delta_{SP} \ll r_i$ that the single-fluid approximations are used, although this rarely occurs for a reconnection event.

In these experiments the Nernst effect transports the fields in early time, and therefore the Nernst-Lundquist number can also be calculated where, instead of the Alfvén velocity being used, we substitute the Nernst velocity, $S_N = v_N \mu_0 L/\eta$. Due to the Nernst velocity and Alfvén velocity being so similar, the Lundquist number for the two is the same. When this Nernst-Lundquist number is large, the resistive effects are small.

Overall the experiment has demonstrated that, with ICF relevant conditions and targets, the focussing of the laser spots in close proximity can have an effect on the generation and interaction of magnetic fields. Various experiments have

shown the need for the inclusion of terms, such as the Nernst effect, in simulations for accurate modelling of both electric and magnetic fields. In two or more laser spot configurations the magnetic fields can reconnect and reorganise. The magnetic field strengths generated are lower than predicted by VFP codes, unless anisotropic pressure effects are taken into account. The rates of the reconnection also mean that a semi-collisional reconnection model is required and that original models such as those from Sweet-Parker predict rates which are too slow.

5.9 Further Work

The investigations completed within this experiment still leave some areas unanswered. The appearance of lines in the proton radiographs through the reconnection region cannot be fully explained or modelled. This is an interesting area to study further, with the potential of explaining them via the creation of plasmoids.

Dimmer emission lines seen between the laser spots on the GXD images also could be investigated further. Future experiments could look at ways of designing a target or diagnostic to try to capture better information about this detail and to see what temperatures might be required for this to appear.

Finally, if other experiments were to be conducted using reconnection geometries, it would be interesting to see, with the same conditions, what the proton radiographs would look like when probing from the opposite direction. This would confirm the magnetic fields strengths measured here and see if any more details in this region can be observed. Late time proton radiographs could be taken so that field structures are recorded after the main laser pulses have been switched off.

Chapter 6

Laser-Driven Currents around Loop Targets

6.1 Motivation

Magnetic fields are produced in laser-plasma interactions around the laser spots and can be of up to very high values (~ 340 MG [151]). Targets with loops attached can be used to produce fields by driving currents through the loop and create quasi-static magnetic fields at the centre of the loop. However, the driving mechanisms for generating this field is unclear.

The magnetic fields created around loop targets could, potentially, assist in confining charged particles, such as in ICF experiments where confinement of electrons would help reduce the heat transport out of the hot spot and contain alpha particles. These type of loop targets have been used in collisionless shock experiments [152] where, due to their smaller size than permanent magnets, the diagnostics have easier access to the interaction.

The use of the loop targets was initially demonstrated by Daido *et al.* in 1986 [153] where, with the use of a CO_2 laser, he drove hot (>10 keV) electrons between two plates. This produced a 100 kA current and 60 T magnetic field around a 2 mm diameter loop. Since this experiment similar configurations have been utilised by many others[154, 155, 156, 152, 157, 158]. The magnetic fields have been measured using either B-dot probes, Faraday rotation or proton deflectometry.

The most recent, published experimental work in this area has been done

by Gao *et al.* [157]. They investigated the magnetic fields produced using proton radiography. Two copper foils were placed 600 μm apart and connected by a copper wire. Two lasers were focussed onto the rear plate, through two holes. These delivered 1.25 kJ of energy in a 1 ns pulse. The current between the two plates was inferred from the 200-250 T magnetic field measurements, giving results of 18-22 kA. An additional loop was added to the foils and the magnetic field around each wire was found to be the same as that with just a single loop, suggesting that the current is voltage driven rather than from a current source.

Zhu *et al.* [158] used a different approach. They used a single wire loop, as shown in Figure 6.1. This target did not have two parallel plates opposite each other, so the plasma from the back plate was not trapped by the front plate. Using this target they explain that the current being driven through the loop is a cold current from the background electrons, rather than the hot electron current that is driven away from the target by the laser. They also describe how by having such a large current travelling through the wire, the properties of the wire (e.g. resistivity) will also change, as the wire becomes ionised. They suggest that an expanding plasma will be formed from the wire itself and increase cross-section the current flows through. They were able to show that the current induced in the wire is a function of $I\lambda^2$ as has been thought previously, also supporting a voltage source for the magnetic field generated.

These experiments have a strong dependence on the $I\lambda^2$, due to the absorp-

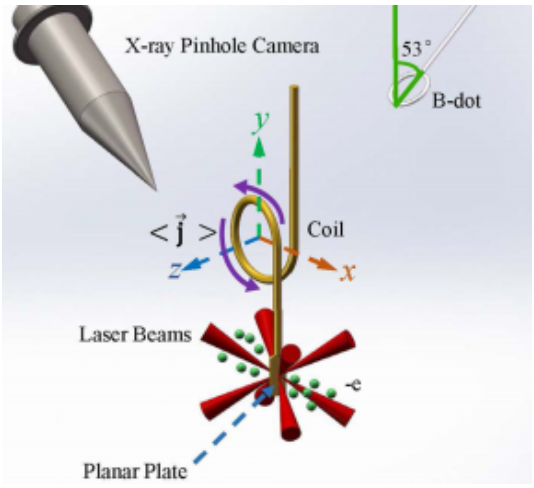

Figure 6.1: A diagram of the target set-up used in the experiment conducted by Zhu *et al.* [158] and the current generated through the coil, measured by a B-dot probe.

tion of the laser energy improving with higher $I\lambda^2$ values. Experiments previously conducted used intensities of $I\lambda^2 \geq 10^{16}$ W/cm$^2\mu$m^2, rather than the lower $I\lambda^2$ (10^{13} W/cm$^2\mu$m^2) discussed in this chapter.

Even with the research being done into the understanding of the generation of these magnetic fields, there is still much to be understood. The experiment described in this chapter sets out to use a novel method of measuring the voltage produced between the two connected plates. It is hoped with these new targets and measurements of voltages that a better predictive capacity, and therefore optimisation, of these coil targets will be achieved. The method for how these results are collected will be explained followed by a presentation of results from the Thomson scattering and shadowgraphy diagnostics. The voltage measurements will be shown along with calculations of circuit relevant parameters, such as capacitance, inductance and resistance. The voltage traces will be compared and briefly discussed as to why the voltage evolves in the way that is observed. Finally the chapter will conclude with suggestions for steps to take this research further.

6.2 The Experiment

The results presented in this chapter are from experiments conducted at the JLF, using the Janus laser and produced the first measurements of voltages created across a loop target. The Janus target area allows two main interaction beams to propagate in to the target area, in addition to a third probe beam. The two main beams, East and West, were used in 1054 nm and 527 nm wavelengths, respectively. The East beam was used as the primary interaction beam and the West was used for Thomson scattering at a scattering angle of 90°, as shown in Figure 6.2. The beams energies and relative timings were changed during the experiment. The East beam had 100 J in a 1 ns pulse for the large energy shots and was reduced to 1 J and 1-10 ns in length when using the circuit loop targets. The West beam was changed from 50-250 J in a 1-5 ns pulse duration. The two beams were separated by 0-3 ns.

The targets varied in this experiment from single copper plates to two copper plates, with the front plate having a hole in its centre to shoot the laser through and onto the back plate. Loops were also added to the two plates, allowing charge to flow

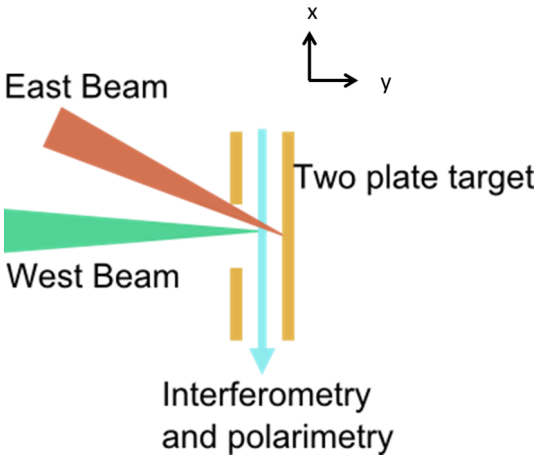

Figure 6.2: A diagram of the set-up for the experiment using two copper target plates with the East, primary interaction beam, West, Thomson scattering beam and an additional probe beam, where the x-axis and y-axis are in the horizontal viewing plane. The Thomson scattering is run without a loop on the target.

between the two. We also attached these loops to a stripline circuit board as can be seen in photograph of Figure 6.3. The stripline attaches to a SMA connection and high frequency co-axial cable into an oscilloscope. These were designed to measure the voltage produced across the two plates.

Figure 6.3: A photograph of the loop target attached to a circuit board with SMA connection.

The voltage measurements were made with low (1 J) energy laser pulse, so as not to destroy the target on each shot or damage the equipment measuring the voltage. The laser pulse length was varied from 1 ns to 10 ns. The shape of the laser pulses was not particularly smooth or consistent between longer pulse length shots, resulting in some variation within the results.

Thomson scattering, interferometry, shadowgraphy and polarimetry were used

to measure electron temperature, electron density and magnetic fields as well as oscilloscopes to measure the voltages produced. The temperature, density and plasma flow velocities extracted from these diagnostics for the higher energy laser shots are presented first. Then the results will primarily concentrate on those from the circuit loop target, shown in Figure 6.3.

6.3 Temperature, Density and Plasma Velocity Measurements

The results from the Thomson scattering and shadowgraphy allowed us to characterise the temperature inside a small volume between the two plates. A 1 ns and 100 J of laser energy in the East, main drive beam was focussed onto a copper plate, with or without an additional copper plate in front. At these higher energies we aimed to measure the plasma temperature, as well as understand the plasma filling the gap between the plates. This diagnostic was not run at lower energies due to the plasma density being too low.

6.3.1 Thomson Scattering Results

The Thomson scattering used the West beam to scatter from the plasma 1 mm from the back plate and collected by optics at 90°, vertically to the main beam, as seen in Figure 6.4.

The results collected from the EPW scattering are shown in Figure 6.5. A lineout can be taken across the image and fitted with a Thomson scattering calculation,

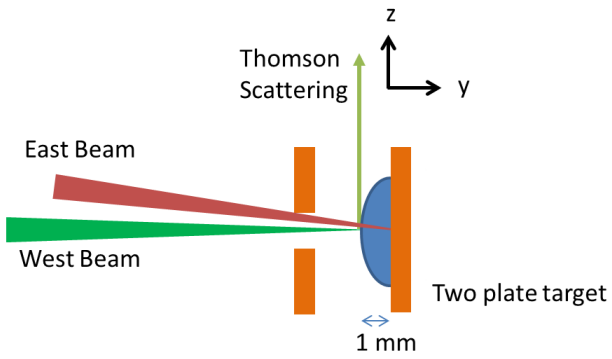

Figure 6.4: A diagram of the layout for the Thomson scattering where collection is from 90°above the target in the z-axis (vertical direction).

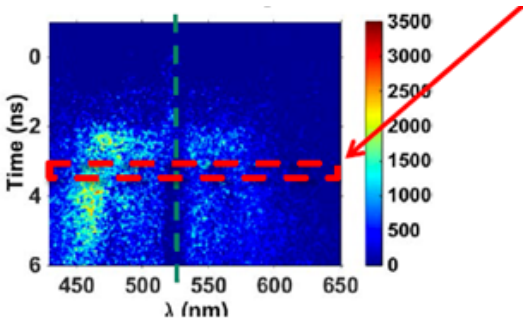

Figure 6.5: An image of the raw EPW data collected from Thomson scattering. The red box indicates the region over which a lineout is taken to extract a temperature measurement.

as described in Section 3.7, to extract the temperature and density measurements shown in Figure 6.6.

The first graph, 6.6a, is from a single copper plate and the T_e is measured to be approximately 200±20 eV and $n_e = 8.0 \pm 0.8 \times 10^{18}$ cm^{-3} at 3.5 ns after the main lasers were switched on. The results in Figure 6.6b, show similar measurements made at 3.5 ns, but with an additional copper foil 2 mm from the back plate, with a hole in front to shoot the laser through. The temperature increases to $T_e = 700 \pm 70$ eV and density $n_e = (3 \pm 0.3) \times 10^{19}$ cm^{-3}, which is three times larger than when the front plate is absent. This suggests that trapping the plasma between the plates enhances the plasma heating and density.

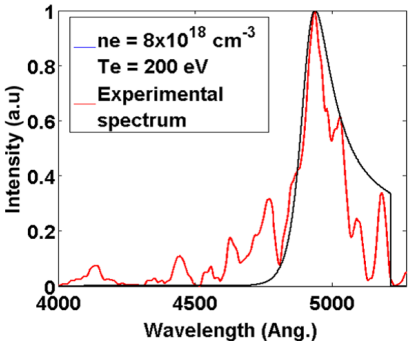

(a) Single copper foil

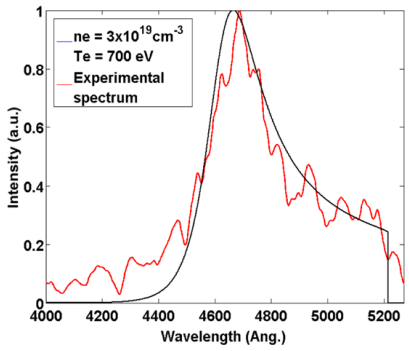

(b) Two copper foils separated by 2 mm

Figure 6.6: Graphs of the resulting EPW spectrum and the fit plotted to extract a measurement for the electron temperature, T_e, and density, n_e [159].

6.3.2 Shadowgraphy Results

The optical probe was used to create shadowgrams of the interaction. In Figure 6.7 we can see the results from using the probe with single and double foils.

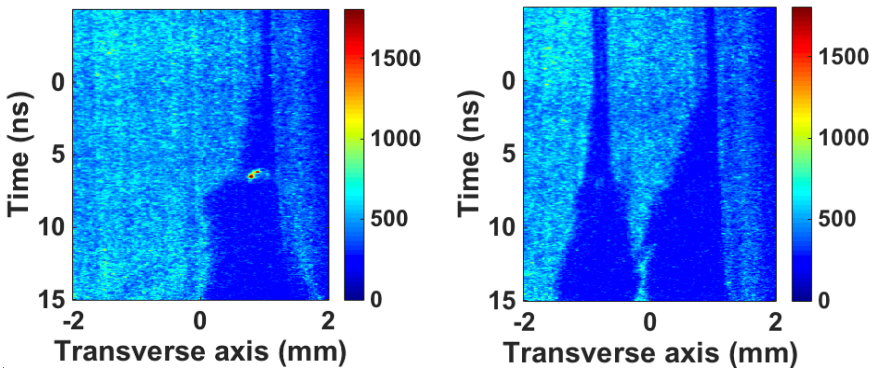

(a) Single copper foil

(b) Two copper foils separated by 2 mm

Figure 6.7: Images from the shadowgraphy of both single and double copper foils.

These images are streaked in time and show the expansion of the plasma. Figure 6.7a shows the plasma expansion from a single copper foil. The plasma is expanding with a velocity of approximately 10^7 cms^{-1}. The plasma from the back plate expands at approximately the same rate for the double foil case, Figure 6.7b. However it is seen that the front plate also expands. The front plate is not directly hit by the laser but may be heated by reflected and scattered laser light and X-rays being emitted from the rear plate.

These measurements show that the second plate affects the plasma, even before loops connect the two plates electrically. The gap between the plates closes up with plasma fairly rapidly and we wish to understand how this affects the current through the loop, by measuring the voltage between the plates.

6.4 Voltage Measurements

The measurements made and presented in Section 6.3 use a 1 ns, 100 J main interaction beam. For the following targets and measurements of the voltages, the energy of the laser was much smaller (1 J) and used circuit loop targets. The intensity on target was on the order of 10^{13} W/cm^2. The targets were attached to oscilloscopes to measure the voltage induced between the two plates when one plate is hit by a laser. The voltage signals were attenuated depending on the energy and pulse length requested of the laser. When analysing the signals, the attenuation factor was used to multiply the signals back to their original signal amplitude, although this also increased the noise levels.

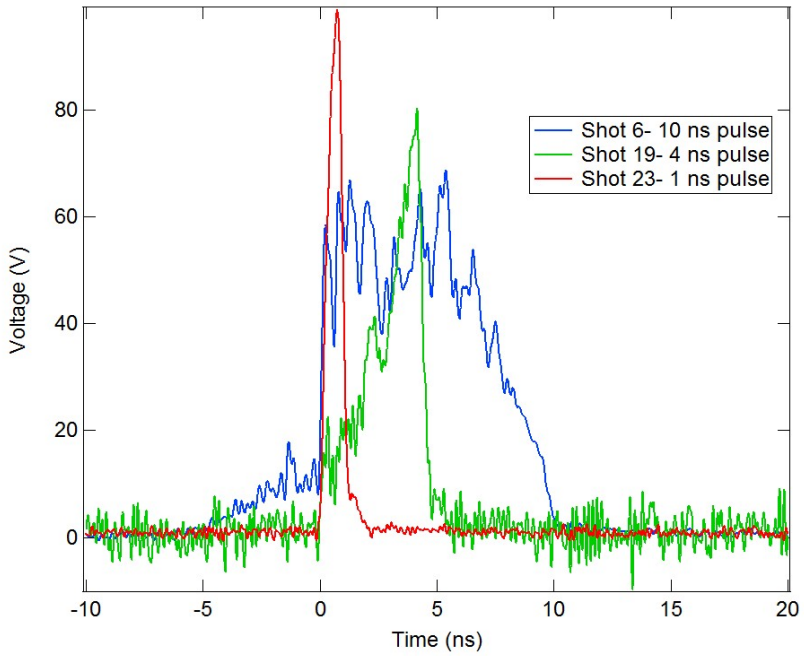

Figure 6.8: A graph of 3 laser traces of different pulse lengths showing the temporal structure of the laser pulses of durations of between 1 and 10 ns.

6.4.1 Errors in Calculations

Due to the nature of the facility and the uncommonly low energy, as well as the variety of laser pulses from 1 to 10 ns we were requesting, the laser energy and pulse shape varied from shot to shot. An energy calibration was taken to give an estimate of the energy on target. This was done by recording the laser energy on target and also from leakage off a final mirror as recorded by a time integrating diode. There will be error in estimating the integrated pulse shape for each shot and relating this to the final errors, although the energies calculated are found to be accurate to ±50 mJ. The laser shape was highly structured for the longer pulse lengths, as shown in Figure 6.8, making the determination of the pulse length more challenging.

6.4.2 Results from Voltage Traces

Voltage signals when using a 1±0.1 ns and 1300 ± 50 mJ laser pulse can be seen in Figure 6.9. Four different shots are shown and all exhibit fairly similar behaviour. There is an initial dip in the voltages to about -50 V, which is identified as being due to a pre-pulse on the laser. This dip is 5±0.1 ns in length until the main laser pulse hits the back plate, charging the plate up so that a much larger negative voltage is recorded. After a negative peak is reached in the voltage, approximately when the

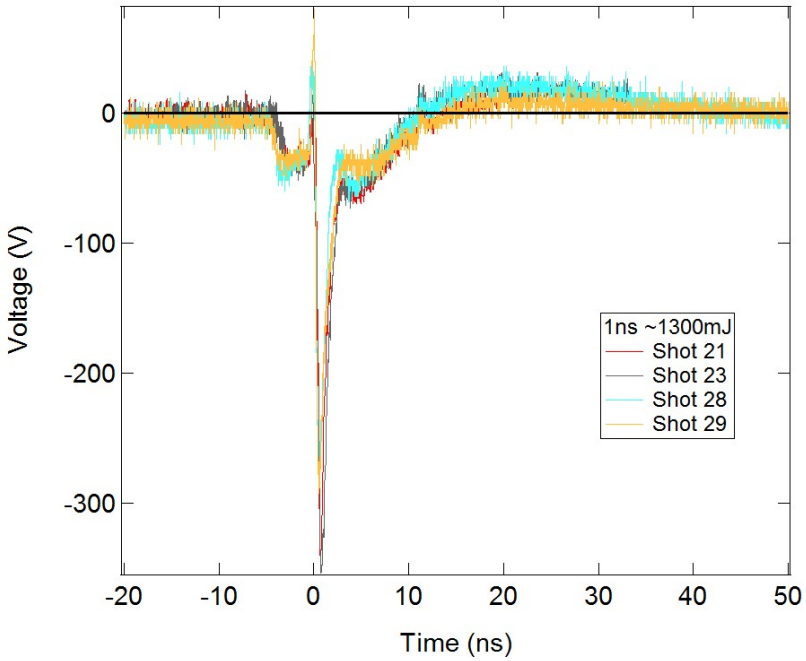

Figure 6.9: Voltage traces recorded from the loop target using 1 ns laser pulses of 1300±50 mJ.

main laser switches off, the voltage starts to decrease and tend towards 0 again. It reaches a smaller and broader peak of around -50 V at 28 ns. Then it appears to drop slightly again. Finally it increases smoothly and overshoots 0 V falling back over longer time-scales, in an exponential decay, as the charge redistributes again.

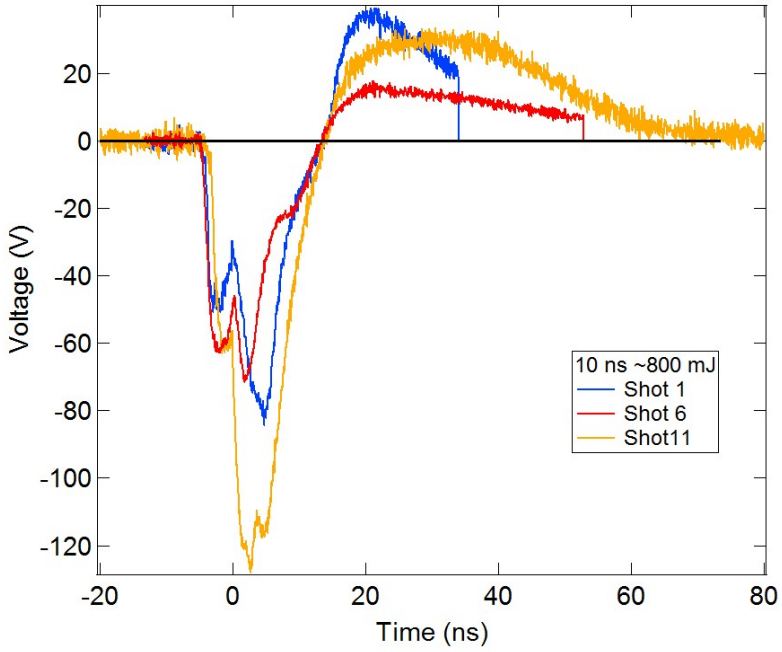

Figure 6.10: Voltage traces for 10 ns laser pulses of 800±50 mJ.

The laser pulse was also stretched out to 10±0.1 ns, with slightly lower energies of 800±50 mJ. The voltage traces for 3 shots are seen in Figure 6.10. These voltage traces, in comparison to the 1 ns pulse signals (Figure 6.9), reach much smaller voltages. There still exists the initial 5 ns dip from the inferred pre-pulse, before a second larger negative voltage reading is reached. The peak negative voltage is reached 1.6±0.1 ns after the pre-pulse, later than seen for the 1 ns pulse, but before the laser has been turned off. There is a small change in the slope of the decreasing voltage as it tends to 0, seen in the traces at about 6-7 ns after the pre-pulse ends. This change is unlike that for the 1 ns laser pulse shots, never tending to being more negative again, just slightly stalling in the rate that the voltage tends to 0 V. The voltage then overshoots the 0 V point by several 10s of volts, before returning to 0 V over longer timescales.

Shots using 1 ns duration pulses were also taken focussing the laser onto the front side of the loop target, driving a positive voltage between the two plates as seen in Figure 6.11. The voltage, after it reaches a peak, returns back to 0 V. This change happens very quickly and the FWHM of the voltage spikes seen in Figure 6.11 are 1.2±0.1 ns. The voltage doesn't go immediately back to being 0 V and reaches a slightly higher value. The front side traces do not show the initial pre-pulse observed

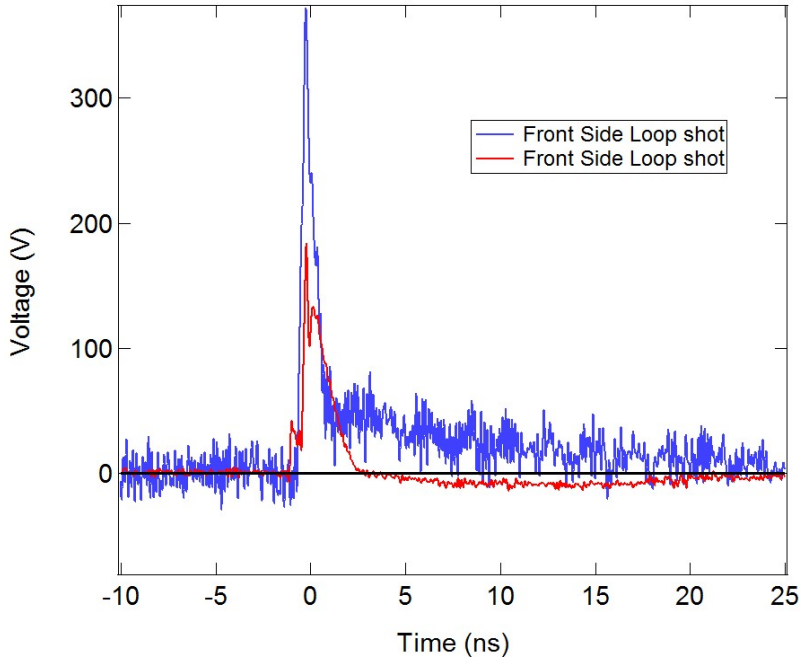

Figure 6.11: A plot of the voltage signals when focussing the laser onto the front side of the loop sing 1 ns laser pulses of 1300±50 mJ.

earlier, although the reason for this is not known.

Shots were taken where the loop was cut, removing the contribution to the voltage signals from current flowing through the loop. This shot is compared to an uncut loop of similar laser energy and pulse length (1300 ± 50 mJ and 1±0.1 ns) in Figure 6.12. The traces are alike in general trend, but there are significant differences. The main differences are a slower increase to the 0 V point, a higher peak negative voltage and the absence of any second small dip, for a cut loop, as the voltage decreases.

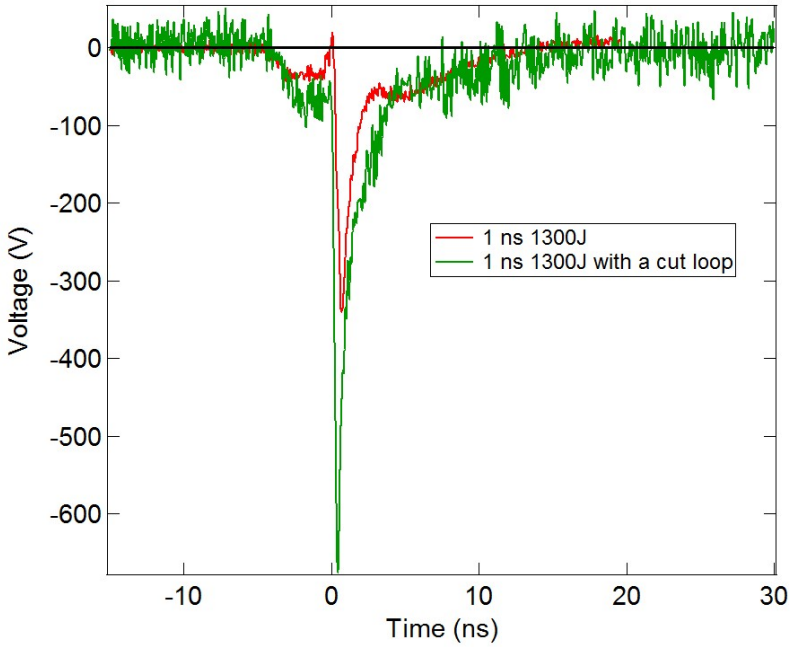

Figure 6.12: A plot of the voltage signals when using either a complete loop target, or one with a cut loop, preventing the flow of current through the loop between the plates. Both signals are from using a 1 ns, 1300 ± 50 mJ laser pulse.

The laser pulse shapes can be plotted with the voltage signals to compare when the laser is on and what the voltages respond with. These are shown in Figure 6.13. For the 1 ns pulses when the laser switches off the voltage stops increasing negatively and starts to return to 0 V. However, for the longer pulse lengths the laser is still on when the voltage starts to tend back to 0 V.

6.4.3 Parameters Relevant for a Circuit Model

When modelling this type of target it has been often approached by assuming the loop target to be represented by a capacitor, inductor and resistor [156, 157], as

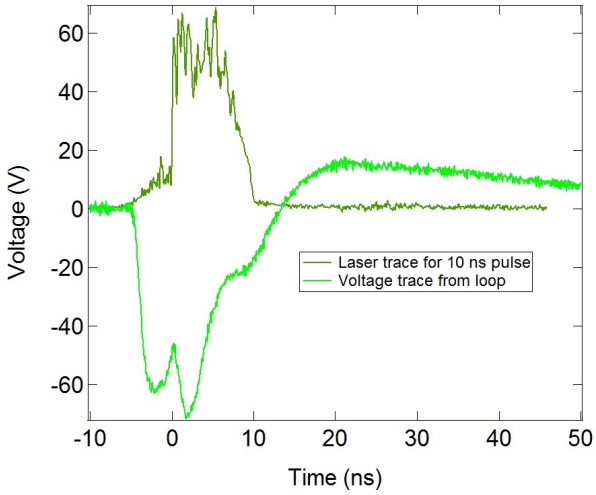

(a) A laser trace and voltage signal for a 10 ns pulse.

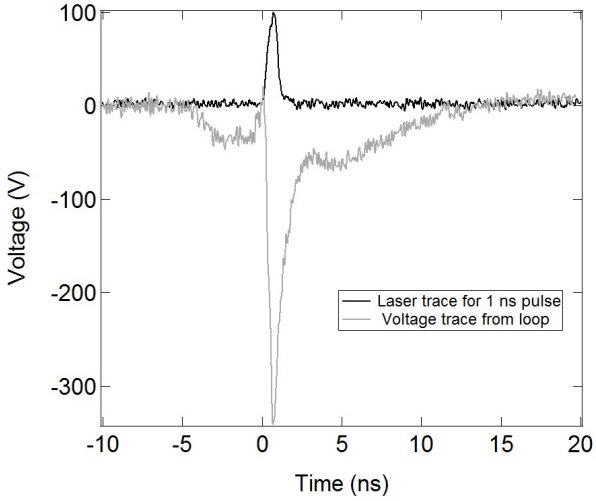

(b) A laser trace and voltage signal for a 1 ns pulse.

Figure 6.13: Graphs of two laser pulse traces of 1 ns 6.13b and 10 ns 6.13a, both of 1300±50 mJ and the resulting voltage signals recorded by the loop target.

shown in Figure 6.14. There are therefore several parameters, such as the capacitance, inductance and resistance, that can be calculated for each.

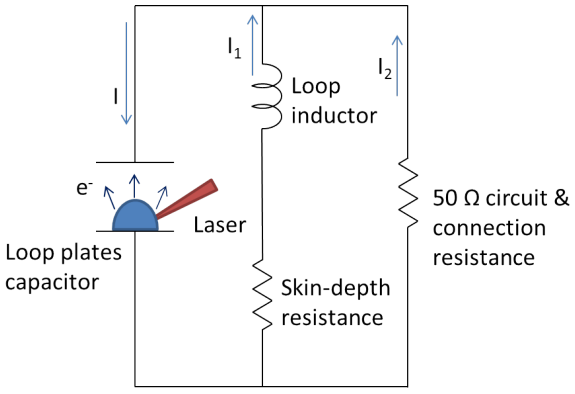

Figure 6.14: A diagram of the potential circuit that could represent the loop target and resistance of the circuit board measuring the voltage.

The plates of the loop targets are assumed to act like a capacitor, potentially storing a charge. The capacitance can be calculated using the Equation (6.1)

$$C = \frac{\epsilon A}{d} \tag{6.1}$$

where ϵ is the permittivity, which is taken to be a vacuum, ϵ_0, A is the area of the plate and d is the separation between the plates. The area of the plate is the most difficult parameter to estimate, as our capacitor is not an individual component connected to the loop, rather it is the loop as a whole. The area was assumed to be 2 mm^2. The distance between the plates is set by the width of the circuit board, which is 0.5 mm, giving a capacitance of 0.035 pF.

While current flows through the loop it will act like an inductor. The inductance for a loop is calculated using Equation (6.2), taken from Grover [160],

$$L = 2l\left[\ln\left(\frac{2l}{w_{th}+t}\right) + 0.5 + 0.2235\left(\frac{w_{th}+t}{l}\right)\right] \text{ nH} \tag{6.2}$$

where l is the length, 0.2 cm, w_{th} is the width, 0.1 cm and t is the thickness, ≤ 0.005 cm of the loop. This gives an inductance of 0.1 nH [160].

The material of the loop will also act to resist the flow of current. We take the resistance in the high frequency limit using Equation (6.3)

$$R = \frac{\rho l}{2 w_{th} \delta} \tag{6.3}$$

where ρ is the resistivity of the loop and δ is the skin depth of the loop. We assume there is a high frequency current running through the loop, due to the appearance of the temporal structure of the voltage traces. We calculate the area that the current passes through using the skin-depth, δ, which includes a factor of two, to account for current flow on the surface, inside and outside of the loop. The skin-depth is calculated using Equation (6.4) which reduces to (6.5) as $\omega \ll 1/\rho\epsilon$,

$$\delta = \sqrt{\frac{2\rho}{\omega\mu}}\sqrt{\sqrt{1+(\rho\omega\epsilon)^2}+\rho\omega\epsilon} \tag{6.4}$$

$$\delta = \sqrt{\frac{2\rho}{\omega\mu}} \tag{6.5}$$

where ω is the angular frequency of the current, $\mu = \mu_r\mu_0$ and $\mu_r = 1$ and μ_0 is the permeability of free space [161]. The current frequency is taken to be 1 GHz,

which will be due to the plasma frequency, Equation (2.23). The resistivity for copper is 1.68×10^{-8} Ωm and 2.44×10^{-8} Ωm for the gold circuit board. The skin-depth is 5.16 μm for copper and 6.22 μm for gold. This results in a resistance of 0.003 Ω for copper and 0.004 Ω for gold. However this does not account for the resistivity change as the copper and gold heat up with the flow of current through the loop. The effect of temperature on the resistivity of a material is one in which there are several models. Spitzer resistivity [162] is used to model electron transport in many simulations. However it does not predict the resistivity accurately for low temperatures such as those we expect in this experiment [163, 164]. The Lee-More model [165] can predict the resistivity for lower temperature plasmas more accurately by taking into account the melting temperatures and Fermi-Dirac degeneracy effects [166]. The resistivity dependence on the temperature using the Lee-More model for copper is shown in Figure 6.15. For the temperatures that we expect for the 1 J shots, the resistivity is expected to increase but not exceed 1 eV. This would increase the resistance of the loop and should be taken into account when looking at the voltage measurements.

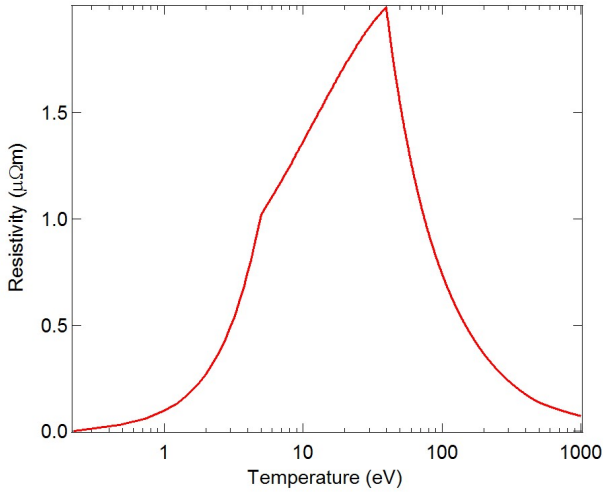

Figure 6.15: A plot showing the resistivity of copper with temperature, from the Lee-More model [166].

We can estimate a current flowing through the circuit loop by taking the following steps. Firstly we consider the effects of a temperature associated with the electrons, assuming a Boltzmann distribution for the electron density, given by Equation (6.6),

$$n_e(z) = n_{e0}e^{\beta} \tag{6.6}$$

where $\beta = e\varphi/kT_e$. The ions are assumed cold and are described by a step function for a cold temperature approximation, (6.7).

$$n_i(z) = n_{i0}[\theta(z + D/2) - \theta(z - D/2)] \tag{6.7}$$

where $D/2$ is half the width of the step function that is being described in the z direction. Poisson's equation, (6.8), describes the potential created by a division of the electrons and ions.

$$\nabla.\varphi = -\rho/\epsilon_0 \tag{6.8}$$

Then substituting in for φ and using the charge density, $\rho = Zen_i - en_e$ gives

$$\frac{\partial\beta^2}{\partial z^2} = -\frac{e}{T_e}\frac{Zen_{i0}[\theta(z + D/2) - \theta(z - D/2)] - en_{e0}\exp(\beta)}{\epsilon_0} \tag{6.9}$$

Finally assuming that there is quasi-neutrality, i.e. $n_{e0} = Zn_{i0}$,

$$\frac{\partial\beta^2}{\partial z^2} - \frac{\exp(\beta)}{\lambda_D^2} = -\frac{1}{\lambda_D}[\theta(z + D/2) - \theta(z - D/2)] \tag{6.10}$$

We can make the further approximation that β is small, and therefore $\exp(\beta) \approx 1 + \beta$ which gives the potential within the boundary conditions as

$$\frac{e\varphi}{T_e} = 1 - \frac{1}{2}\exp\left((|z| - D/2)/\lambda_D\right) \quad |z| \le D/2 \tag{6.11}$$

$$\frac{e\varphi}{T_e} = 1 - \frac{1}{2}\exp\left((D/2 - |z|)/\lambda_D\right) \quad |z| \ge D/2 \tag{6.12}$$

Adding all the voltage contributions together gives Equation (6.13), which can then be solved for the current, I, using Equations (6.11-6.12) and Laplace transforms, to give Equation (6.14) which is the coil current after integrating the oscilloscope voltage.

$$V_{scope} = R_2 I_2 = L\frac{dI_1}{dt} + R_1 I_1 \tag{6.13}$$

$$I_1(t) = \int_0^t \frac{V_{scope}(\tau)}{L}\exp(-(t - \tau)/t_0)d\tau \tag{6.14}$$

where $t_0 = L/R_1$.

6.4.4 Measuring the Capacitance

In the complete loop voltage traces we observe a late time overshoot of 0 V and an exponential decay to bring it back to 0. This feature is not present in the cut loop traces, so assuming this late time decay is due to a current flowing, and the loop acting like a discharging capacitor, we can calculate the capacitance. A discharging capacitor has a voltage decay across a resistor, of resistance R, which is given by Equation 6.15

$$V_{source} = A + V\exp(-(t - t_0)/RC) \tag{6.15}$$

By fitting an exponential to this late time region, as shown in Figure 6.16, an RC value of between $10 - 5000$ ΩnF depending on the shot is inferred. This is then converted to capacitance using the resistance of the SMA cable as 50 Ω to give 0.4-7.4 nF. There does seem to be quite some variance in the capacitance values calculated from the fits which might be due to the variability in the laser. Some of the fit parameters for these exponential decays are given in Table 6.1.

Comparing this capacitance to the predicted capacitance (~ 0.035 pF) from Equation (6.1), the measured value is higher by a factor of 10^4. This might be

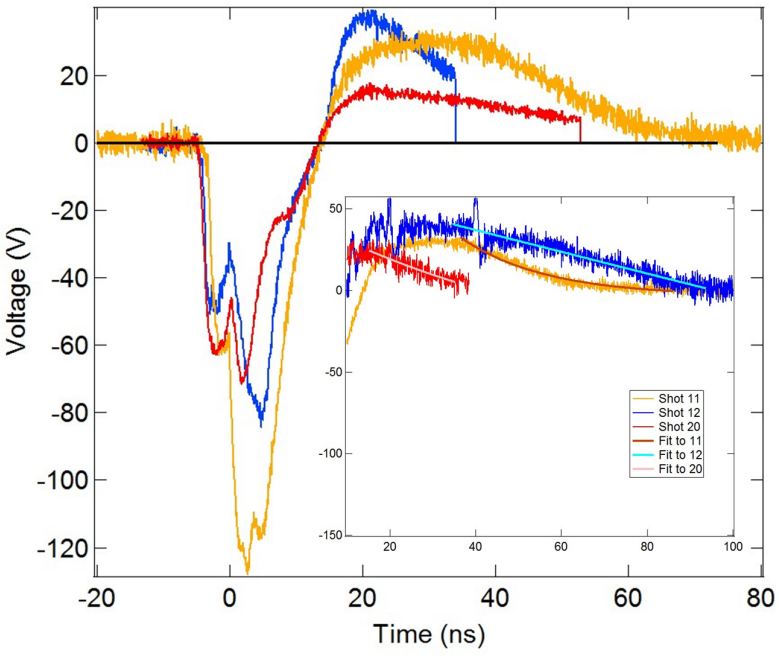

Figure 6.16: A graph of the voltage traces for the various loop targets. The insert shows the tail-end of the voltages in more detail, with exponential decay fits plotted to the data.

Shot Number	Laser Energy (mJ)	Pulse Length (ns)	t_0 (ns)	RC (ΩnF)	C (nF)
11	800±50	4±0.1	71	20 ±5	0.4±0.1
12	1100±50	1±0.1	84	230±40	4.6±0.8
20	880±50	1±0.1	47	30±15	0.6±0.3

Table 6.1: A table of the different RC and capacitance values calculated for different shots from matching an exponential fit to the late time voltage traces.

due to the permittivity being higher if plasma is still between the plates. However this would not give a factor 10^4 larger capacitance. If there is still movement of free electrons and ions between the plates, then this could lead to a changing voltage, but we would also expect this behaviour when the loop was cut, which is not observed.

The values of the time constant (RC) given for shots 11 and 20 are very close to the measured time constant given by Courtois [156] of 17±4 ns, even though their laser intensities were much higher. They assumed this decay to be from an L/R circuit, rather than a RC circuit. If we do ignore the capacitor component and instead model the circuit as just an inductor-resistor circuit, where the exponential decay is from and L/R circuit decay, as given by Equation (6.16),

$$I(t) = I_0(1 - e^{-\frac{R}{L}t}) \tag{6.16}$$

then the time constant from the graphs gives inductances of between 1000-11200 nH using R=50 Ω, which are high compared to the anticipated inductance of 0.1 nH calculated using Equation (6.2). The measured time constants vary by a factor of 10. These values are highly shot dependent and sensitive to where the exponential limits are taken on the data. The results would need to be repeated with better precision before any conclusions could be made.

6.4.5 Discussion of the Stages of Charging the Loops

Previous models suggest that when the laser is incident onto the back plate it is absorbed via inverse bremsstrahlung, heating both electrons and ions, and driving fast hot electrons ahead of the ablated material, which are then incident on the front plate. Figure 6.17 shows a diagram of what charge the front or back plates need to have for a negative voltage reading as observed at the start of some laser shots.

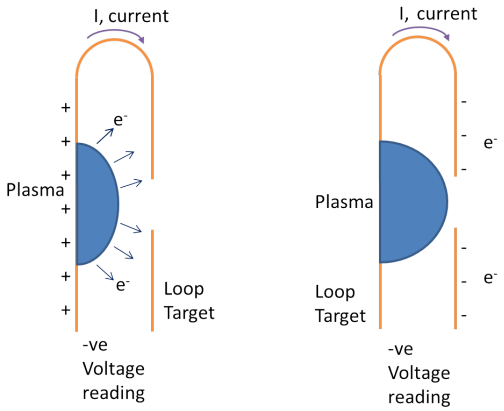

Figure 6.17: A diagram of the charges on the loop plates for the voltage reading to be negative. The opposite is true for a positive voltage to be recorded.

When we hit the back plate of the target with the laser we always drive a negative peak voltage, whereas if the front plate is hit then a positive voltage is driven. The negative voltage is driven from electrons being removed from the back plate first, leaving a net positive charge. The peak voltage is higher for shorter pulses (1 ns), by a factor of 4, than for the longer pulses where the voltage tends to 0 V before the laser is switched off. The reason for the voltages tending back to 0 V after these peak voltages is currently under discussion as there are several methods via which the plates would be brought back to equilibrium.

The loop targets also all seem to overshoot the 0 V later in time, resulting in an exponential decay of the voltage. The exception for this feature is when we have a cut loop target. This suggests that the overshoot is due to the current being allowed to flow through the loop, contributing to a charge distribution over the plates that encourages the voltages to become uneven at late time. At this late time, for the voltage to be decaying exponentially from a slightly positive value, the current would need to have reversed direction to that at the start of the signals, and be flowing from the front plate to the back. Using the cut loop targets we also observe that the peak voltages at early times are double that of the complete loop targets. This is likely to be due to the current that can flow through the loop of the complete targets reducing the voltage difference between the two plates.

When hitting the front plate of the target, compared to the back plate, we can also consider that any expanding plasma will not be trapped or incident onto a second plate in front. Some features that we observe in the shots onto the back

plate could be attributed to having this second plate in front, such as the longer time, after the peak voltages are reached, for the voltage to tend back to 0 V when the back plate is shot compared to the front plate.

These different shots are useful in starting to identify differences between the voltage traces and postulate ideas for what might be causing the signals. However, without additional shots and repeats of measurements it is difficult to confirm more details of the driving mechanisms.

6.5 Conclusions

Overall we have observed that the temperature and density increases when adding a plate in front of the back plate. This occurs from trapping the plasma into a confined area. The use of circuit loop targets proves to be a useful way to measure the voltage between the plates. However, there remain questions as to the dynamics occurring between the plates and explaining the voltage traces. The current flowing between the plates appears to start at early time, reducing the peak voltages reached by the targets. The current also seems to create an 'overshoot' at late time, of the voltage tending back to 0 V, resulting in the current flow direction reversing, and decaying exponentially, similar to an RC circuit. Simple circuit estimates result in unrealistically large capacitance and inductance measurements. This chapter has presented ideas for why the voltage signals evolve as seen, although this is still open to interpretation.

6.5.1 Further Work

It would be interesting as further work, to repeat several of the shots conducted using the Janus laser, and to explore the effect of pulse time and energies on the voltage traces. With higher energies it might also then be possible to use additional diagnostics to measure the plasma parameters. This could lead to understanding the threshold for each of the effects and the different processes going on.

Various target materials being used for the loop might lead to understanding about how the electrons and ions are released and accelerated from the targets. It would be especially interesting to use an insulating material, that would restrict

the current flow through the loop and see the effects of this. As well as this, if a second foil, unattached to the loop, was also shot within range of the loop, such that electrons or ions produced from it, could impact the loop target, this might help our understanding on whether the electrons do travel ahead of the ions in the plasma expansion.

Finally the cut loop targets comparison to the normal loops greatly aids the overall understanding of what the loop component and current flow changes in the experiment. This understanding would not only assist in being able to make informed decisions on how to maximise the current through the loop and the magnetic fields being generated, but also give a better understanding of a laser-plasma interaction.

Chapter 7

Conclusions

This thesis has presented research using high power lasers to investigate magnetic fields generated in several different laser-plasma environments. The generation of magnetic fields generated around laser spots has been utilised for creating reconnection events by placing two laser spots within close proximity. The magnetic fields, in the experiment described in this thesis, reconnect via a semi-collisional reconnection model, involving Nernst effects as well as anisotropic pressure. These additional effects are shown to allow reconnection whilst maintaining lower (~50 T) magnetic field strengths in the central colliding region. Proton and optical probing yielded results from 3 different target projections, something which has never previously been published for a reconnection experiment. The images from these diagnostics help to build a better representation of the fields and plasma movement as the interaction evolves. The spectrometer and GXDs give measurements of temperatures and these support those predicted by simulations. The use of the hydrocode simulations and VFP codes compliment each other and appear to better simulate the conditions observed. The understanding gained from this experiment will be able to assist in the research on dynamics occurring within hohlraum physics and also in high plasma-β reconnection events in astrophysics. This experiment has also opened up many routes of further investigation, from several unexplained features within the data, such as the bright line on the GXD images late in time between the laser spots, to the appearance of darker vertical lines through the reconnection region. Future experiments could be designed around trying to enhance and gain more knowledge into what these features are, as well as understanding how multi-

ple laser spots within a hohlraum will affect the plasma dynamics with potential reconnection events occurring.

The development of magnetic fields within SNRs has also been explored, via the creation of blast waves in a laboratory environment. These blast waves have been monitored using a fast framing camera, amongst other diagnostics, and detailed evolution measurements have been made. The shape of the blast waves is of most interest as it is due to the asymmetry that magnetic fields are generated at the fronts. These elliptical shapes have been measured as a ratio of their major to minor axis and found that over time the shape tends to a more symmetrical shape. However both using different targets and simulations this change in the shape is shown to be due to two shock waves produced in an interaction; one which travels around the target, and one which travels through it. The blast wave radius in one direction across the front has often been measured and observed over time in previous experiments, however the asymmetry has never been analysed before. Using this knowledge of how the asymmetry can be influenced by different targets, it might be that blast waves with varying or stronger magnetic field strengths can be generated and used in other applications.

Finally, magnetic fields are also produced using loop targets. In this experiment a novel method of measuring the voltage of the loop is shown and, via different target designs and laser shots taken, features in the signals were noted. These shots were taken using lower laser intensities (10^{13} W/cm^2) than have been present on other experiments but the knowledge gained and ideas of how to investigate and amplify the magnetic fields can still be tested. Parameters relevant to a circuit consisting of an inductor, capacitor and resistor were calculated as well as suggested ideas about how the current is driven, through comparison of different target shots. The use of these loop targets for measuring the voltage is one which should be able to help our understanding greatly for both applications of these magnetic fields and of developing clearer theories of how a laser-plasma interaction evolves.

Appendix A

Other Research

Over the course of this PhD the author has worked on several collaborations and publications which are not presented in this thesis. These were:

- J. E. Cross, G. Gregori, J. M. Foster, P. Graham, J. M. Bonnet-Bidaud, C. Busschaert, N. Charpentier, C. N. Danson, H. W. Doyle, R. P. Drake, J. Fyrth, E. T. Gumbrell, M. Koenig, C. Krauland, C. C. Kuranz, B. Loupias, C. Michaut, M. Mouchet, S. Patankar, J. Skidmore, C. Spindloe, E. R. Tubman, N. C. Woolsey, R. Yurchak, and E. Falize, *Laboratory analogue of a supersonic accretion column in a binary star system*, Nature Communications, **7**, 11899 (2016)

- D. Turnbull, P. Michel, T. Chapman, E. Tubman, B. B. Pollock, C. Y. Chen, C. Goyon, J. S. Ross, L. Duvil, N. C. Woolsey and J. D. Moody, *High Power Dynamic Polarization Control Using Plasma Photonics*, Physical Review Letters, **116**, 205001(2016)

- J. Colgan, A. Ya. Faenov, S. A. Pikuz, E. Tubman, N. M. H. Butler, J. Abdallah, Jr., R. J. Dance, T. A. Pikuz, I. Yu. Skobelev, M. A. Alkhimova, N. Booth, J. Green, C. Gregory, A. Andreev, R. Lstzsch, I. Uschmann, A. Zhidkov, R. Kodama, P. McKenna and N. C. Woolsey, *Evidence of high-n hollow ion emission from Si ions pumped by ultraintense X-rays from relativistic laser plasma*, Submitted to EPL.

- E. Oks, E. Dalimier, A. Faenov, P. Angelo, S. Pikuz, E. Tubman, N. Butler, R. Dance, T. Pikuz, I. Skobelev, M. Alkhimova, N. Booth, J. Green, C. Gregory,

A. Andreev, A. Zhidkov, R. Kodama, P. McKenna and N. C. Woolsey, *Modelling Parametric Decay Instabilities in Astrophysics Using X-ray Spectroscopy of Relativistic Laser Plasma Interaction*, Submitted to Scientific Reports.

List of Abbreviations

AWE	Atomic Weapons Establishment
CPA	Chirped Pulse Amplification
EPW	Electron Plasma Wave
FWHM	Full Width at Half Maximum
GXD	Gated X-Ray Detector
IAW	Ion Acoustic Wave
ICF	Inertial Confinement Fusion
JLF	Jupiter Laser Facility
LHS	Left-Hand Side
LPI	Lines Per Inch
LLNL	Lawrence Livermore National Laboratory
MCF	Magnetic Confinement Fusion
MCP	Micro-Channel Plate
NIF	National Ignition Facility
PAM	Pre-Amplifier Module
RAL	Rutherford Appleton Laboratory
RCF	Radiochromic Film
RHS	Right-Hand Side
SBS	Stimulated Brillouin Scattering
SIM16	Specialised Imaging
SRIM	Stopping Range In Matter
SNR	Supernova Remnant
SRS	Stimulated Raman Scattering
TAW	Target Area West
TCC	Target Chamber Centre

TIM	Ten-Inch Manipulator
TNSA	Target Normal Sheath Acceleration
TOF	Time-Of-Flight
TPD	Two Plasmon Decay
VFP	Vlasov-Fokker Planck

Bibliography

[1] R. Paul Drake. *High-Energy-Density Physics: Fundamentals, Inertial Fusion, and Experimental Astrophysics (Shock Wave and High Pressure Phenomena)*. Springer, 2006.

[2] John M. Dawson. On the production of plasma by giant pulse lasers. *Physics of Fluids*, 7(7):981, 1964.

[3] B. H. Ripin, C. K. Manka, T. A. Peyser, E. A. McLean, J. A. Stamper, A. N. Mostovych, J. Grun, K. Kearney, J. R. Crawford, and J. D. Huba. Laboratory laser-produced astrophysical-like plasmas. *Laser and Particle Beams*, 8(1-2):183, Jan 1990.

[4] S. J. Rose. High-power laser-produced plasmas and astrophysics. *Laser and Particle Beams*, 9(04):869, Dec 1991.

[5] Bruce A. Remington, R. Paul Drake, Hideaki Takabe, and David Arnett. A review of astrophysics experiments on intense lasers. *Physics of Plasmas*, 7(5):1641, 2000.

[6] H. Takabe. Astrophysics with intense and ultra-intense lasers: 'laser astrophysics'. *Prog.Theor.Phys.Suppl.*, 143:202–265, 2001.

[7] S. V. Bulanov, T. Zh. Esirkepov, D. Habs, F. Pegoraro, and T. Tajima. Relativistic laser-matter interaction and relativistic laboratory astrophysics. *The European Physical Journal D*, 55(2):483–507, Nov 2009.

[8] V. S. Belyaev, P. A. Batishchev, V. V. Bolshakov, K. S. Elkin, G. F. Karabadzhak, D. V. Kovkov, A. P. Matafonov, G. G. Raykunov, R. A. Yakhin,

S. A. Pikuz, and et al. Promising lines of investigations in the realms of laboratory astrophysics with the aid of powerful lasers. *Physics of Atomic Nuclei*, 76(4):404–422, Apr 2013.

[9] Edward I. Moses. National ignition facility: 1.8-mj 750-tw ultraviolet laser. *Optical Engineering at the Lawrence Livermore National Laboratory II: The National Ignition Facility*, May 2004.

[10] M. J. Norman, James E. Andrew, Thomas H. Bett, Roger K. Clifford, John E. England, Nicholas W. Hopps, Kenneth W. Parker, Kenneth Porter, and Mark Stevenson. Mutlipass reconfiguration of the helen nd:glass laser at the atomic weapons establishment. *Applied Optics*, 41:3497–3505, 2002.

[11] Michel L Andre. The french megajoule laser project (lmj). *Fusion Engineering and Design*, 44(1-4):43–49, Feb 1999.

[12] T.R Boehly, D.L Brown, R.S Craxton, R.L Keck, J.P Knauer, J.H Kelly, T.J Kessler, S.A Kumpan, S.J Loucks, S.A Letzring, and et al. Initial performance results of the omega laser system. *Optics Communications*, 133(1-6):495–506, Jan 1997.

[13] John M. Dawson. Computer modeling of plasma: Past, present, and future. *Physics of Plasmas*, 2(6):2189, 1995.

[14] J.W. Connor and J.B. Taylor. Scaling laws for plasma confinement. *Nuclear Fusion*, 17(5):1047–1055, Oct 1977.

[15] D. Ryutov, R. P. Drake, J. Kane, E. Liang, B. A. Remington, and W. M. Wood-Vasey. Similarity criteria for the laboratory simulation of supernova hydrodynamics. *The Astrophysical Journal*, 518(2):821–832, Jun 1999.

[16] D. D. Ryutov, B. A. Remington, H. F. Robey, and R. P. Drake. Magnetohydrodynamic scaling: From astrophysics to the laboratory. *Physics of Plasmas*, 8(5):1804, 2001.

[17] R. P. Drake. The design of laboratory experiments to produce collisionless shocks of cosmic relevance. *Physics of Plasmas*, 7(11):4690, 2000.

[18] E.. Falize, C. Michaut, and S. Bouquet. Similarity properties and scaling laws of radiation hydrodynamic flows in laboratory astrophysics. *The Astrophysical Journal*, 730(2):96, Apr 2011.

[19] L. Biermann. Uber den ursprung der magnetfelder auf sternen und im interstellaren raum. *Z. Naturforsch.*, 5a:65–71, 1950.

[20] J. Meinecke, H. W. Doyle, F. Miniati, A. R. Bell, R. Bingham, R. Crowston, R. P. Drake, M. Fatenejad, M. Koenig, Y. Kuramitsu, and et al. Turbulent amplification of magnetic fields in laboratory laser-produced shock waves. *Nat Phys*, Jun 2014.

[21] J. Grun, J. Stamper, C. Manka, J. Resnick, R. Burris, J. Crawford, and B. H. Ripin. Instability of taylor-sedov blast waves propagating through a uniform gas. *Physical Review Letters*, 66(21):2738–2741, May 1991.

[22] L. I. Sedov. *CR Acad. Sci. URSS*, 52:17, 1946.

[23] M. J. Edwards, A. J. MacKinnon, J. Zweiback, K. Shigemori, D. Ryutov, A. M. Rubenchik, K. A. Keilty, E. Liang, B. A. Remington, and T. Ditmire. Investigation of ultrafast laser-driven radiative blast waves. *Physical Review Letters*, 87(8), Aug 2001.

[24] G. Taylor. The dynamics of the combustion products behind plane and spherical detonation fronts in explosives. *Proceedings of the Royal Society A: Mathematical, Physical and Engineering Sciences*, 200(1061):235–247, Jan 1950.

[25] E. R. Priest. Magnetic reconnection at the sun. *Geophysical Monograph Series*, pages 63–78, 1984.

[26] G. Atkinson. Mechanism by which merging at x lines causes discrete auroral arcs. *Journal of Geophysical Research*, 97(A2):1337, 1992.

[27] M. Opher, J. F. Drake, M. Swisdak, K. M. Schoeffler, J. D. Richardson, R. B. Decker, and G. Toth. Is the magnetic field in the heliosheath laminar or a turbulent sea of bubbles? *The Astrophysical Journal*, 734(1):71, May 2011.

[28] P. Nilson, L. Willingale, M. Kaluza, C. Kamperidis, S. Minardi, M. Wei, P. Fernandes, M. Notley, S. Bandyopadhyay, M. Sherlock, and et al. Magnetic reconnection and plasma dynamics in two-beam laser-solid interactions. *Physical Review Letters*, 97(25), Dec 2006.

[29] C. K. Li, F. H. Seguin, J. A. Frenje, J. R. Rygg, R. D. Petrasso, R. P. J. Town, O. L. Landen, J. P. Knauer, and V. A. Smalyuk. Observation of megagauss-field topology changes due to magnetic reconnection in laser-produced plasmas. *Physical Review Letters*, 99(5):055001, August 2007.

[30] M. J. Rosenberg, C. K. Li, W. Fox, A. B. Zylstra, C. Stoeckl, F. H. Seguin, J. A. Frenje, and R. D. Petrasso. Slowing of magnetic reconnection concurrent with weakening plasma inflows and increasing collisionality in strongly driven laser-plasma experiments. *Physical Review Letters*, 114(20), May 2015.

[31] NIF. How inertial fusion energy works. https://lasers.llnl.gov/science/icf/how-icf-works, July 2013.

[32] Stefano Atzeni and Jargen Meyer ter Vehn. *The Physics of Inertial Fusion: Beam Plasma Interaction, Hydrodynamics, Hot Dense Matter (International Series of Monographs on Physics).* Oxford University Press, USA, 2004.

[33] D. L. Book. *NRL Plasma Formulary.* Naval Research Laboratory, Washington D.C., 2011.

[34] K Nishikawa and Masahiro Wakatani. *Plasma Physics: Basic Theory with Fusion Applications (Springer Series on Atomic, Optical, and Plasma Physics).* Spring, 2000.

[35] Paul M. Bellan. *Fundamentals of Plasma Physics.* Cambridge University Press, 2008.

[36] S Eliezer, A D Krumbein, and D Salzmann. A generalised validity condition for local thermodynamic equilibrium in a laser-produced plasma. *J. Phys. D: Appl. Phys.*, 11(12):1693–1701, Aug 1978.

[37] William Kruer. *The Physics Of Laser Plasma Interactions.* Westview Press, 2003.

[38] R.J. Kingham and A.R. Bell. An implicit vlasov-fokker-planck code to model non-local electron transport in 2-d with magnetic fields. *Journal of Computational Physics*, 194(1):1–34, Feb 2004.

[39] Marshall N. Rosenbluth, William M. MacDonald, and David L. Judd. Fokker-planck equation for an inverse-square force. *Physical Review*, 107(1):1–6, Jul 1957.

[40] Peter Mulser and Dieter Bauer. *High Power Laser-Matter Interaction (Springer Tracts in Modern Physics)*. Springer, 2010.

[41] S.C. Wilks and W.L. Kruer. Absorption of ultrashort, ultra-intense laser light by solids and overdense plasmas. *IEEE J. Quantum Electron.*, 33(11):1954–1968, 1997.

[42] N. G. Denisov. On a singularity of the field of an electromagnetic wave propagated in an inhomogenous plasma. *Soviet Physics JETP*, 4:544, 1957.

[43] Shalom Eliezer. *The Interaction of High-Power Lasers with Plasmas (Series in Plasma Physics)*. Taylor & Francis, 2002.

[44] R. A. Cairns and J. J. Sanderson, editors. *Laser Plasma Interactions*. SUSSP, 1979.

[45] Jun Li, Bin Zhao, Hong Li, and Jian Zheng. Study of flux limiter using fokker-planck and fluid simulations of planar laser-driven ablation. *Plasma Physics and Controlled Fusion*, 52(8):085008, Jun 2010.

[46] A. Nishiguchi, T. Yabe, and M. G. Haines. Nernst effect in laser-produced plasmas. *Phys. Fluids*, 28(12):3683, 1985.

[47] S. I. Braginskii. Transport properties in a plasma. *Review of Plasma Physics Vol. 1 (edited by M. A. Leontovish)*, page 205, 1966.

[48] M G Haines. Heat flux effects in ohm's law. *Plasma Physics and Controlled Fusion*, 28(11):1705–1716, Nov 1986.

[49] E. M. Epperlein and M. G. Haines. Plasma transport coefficients in a magnetic

field by direct numerical solution of the fokker-planck equation. *Physics of Fluids*, 29(4):1029, 1986.

[50] G. Gregori, A. Ravasio, C. D. Murphy, K. Schaar, A. Baird, A. R. Bell, A. Benuzzi-Mounaix, R. Bingham, C. Constantin, R. P. Drake, and et al. Generation of scaled protogalactic seed magnetic fields in laser-produced shock waves. *Nature*, 481(7382):480–483, Jan 2012.

[51] M. C. Anderson and L. Rudnick. The deceleration powering of synchrotron emission from ejecta components in supernova remnant cassiopeia a. *The Astrophysical Journal*, 441:307, Mar 1995.

[52] J. von Neumann. Blast wave. Technical report, Los Alamos Scientific Laboratory, 1947.

[53] Bruce T. Draine. *Physics of the interstellar and intergalactic medium.* 2011.

[54] Jeremiah P. Ostriker and Christopher F. McKee. Astrophysical blastwaves. *Rev. Mod. Phys.*, 60(1), Jan 1988.

[55] C. J. Clarke and R. F. Carswell. *Principles of Astrophysical Fluid Dynamics.* Cambridge University Press, 2007.

[56] Russell Kulsrud. *Plasma Physics for Astrophysics.* Princeton University Press, 2004.

[57] P. A. Sweet. The production of high energy particles in solar flares. *Il Nuovo Cimento*, 8(S2):188–196, Sep 1958.

[58] E. N. Parker. Dynamics of the interplanetary gas and magnetic fields. *The Astrophysical Journal*, 128:664, Sep 1958.

[59] Hantao Ji, Masaaki Yamada, Scott Hsu, and Russell Kulsrud. Experimental test of the sweet-parker model of magnetic reconnection. *Physical Review Letters*, 80(15):3256–3259, Apr 1998.

[60] H. E. Petschek. Magnetic field annihilation. *The Physics of Solar Flares (NASA Special Publication)*, 50:425, 1964.

[61] Ellen G. Zweibel and Masaaki Yamada. Magnetic reconnection in astrophysical and laboratory plasmas. *Annual Review of Astronomy and Astrophysics*, 47(1):291–332, Sep 2009.

[62] D. A. Uzdensky and R. M. Kulsrud. Two-dimensional numerical simulation of the resistive reconnection layer. *Phys. Plasmas*, 7(10):4018, 2000.

[63] M. E. Mandt, R. E. Denton, and J. F. Drake. Transition to whistler mediated magnetic reconnection. *Geophysical Research Letters*, 21(1):73–76, Jan 1994.

[64] M. A. Shay, J. F. Drake, R. E. Denton, and D. Biskamp. Structure of the dissipation region during collisionless magnetic reconnection. *Journal of Geophysical Research: Space Physics*, 103(A5):9165–9176, May 1998.

[65] A. S. Joglekar, A. G. R. Thomas, W. Fox, and A. Bhattacharjee. Magnetic reconnection in plasma under inertial confinement fusion conditions driven by heat flux effects in ohm's law. *Physical Review Letters*, 112(10), Mar 2014.

[66] Rudolf A. Treumann. Origin of resistivity in reconnection. *Earth Planet Sp*, 53(6):453–462, Jun 2001.

[67] Russell M. Kulsrud. Magnetic reconnection: Sweet-parker versus petschek. *Earth Planet Sp*, 53(6):417–422, Jun 2001.

[68] C.N Danson, P.A Brummitt, R.J Clarke, J.L Collier, B Fell, A.J Frackiewicz, S Hancock, S Hawkes, C Hernandez-Gomez, P Holligan, and et al. Vulcan petawatt- an ultra-high-intensity interaction facility. *Nuclear Fusion*, 44(12):S239–S246, Nov 2004.

[69] M. Galimberti, S. Bandyopadhyay, R. Bickerton, S. Blake, C. Burton, R. Clarke, J. ollier, V. Dubrovsky, M. Dunne, A. Frackiewicz, and et al. The new fast ignitor oriented target area in the vulcan laser at the clf. 2010.

[70] Nicholas Hopps, Kevin Oades, Jim Andrew, Colin Brown, Graham Cooper, Colin Danson, Simon Daykin, Stuart Duffield, Ray Edwards, David Egan, and et al. Comprehensive description of the orion laser facility. *Plasma Physics and Controlled Fusion*, 57(6):064002, Apr 2015.

[71] Kevin Oades, Andrew Evans, Gary Slark, John Foster, Richard Eagleton, and Eugene Clark. Target diagnostics for the future awe orion laser facility. *Review of scientific instruments*, 75(10):4222–4224, 2004.

[72] C.N. Danson, T.H. Bett, N. Cann, S.J. Duffield, R. Edwards, D.A. Egan, S.P. Elsmere, M.T. Girling, T. Goldsack, E.J. Harvey, D.I. Hillier, D.J. Hoarty, N.W. Hopps, S.F. James, M.J. Norman, K. Oades, S.J.F. Parker, P.D. Roberts, P.A. Treadwell, and D.N. Winter. Overview of project orion. AWE, Aldermaston, 38th EPS Conference on Plasma Physics, 2011.

[73] M Borghesi, A Schiavi, D H Campbell, M G Haines, O Willi, A J MacKinnon, L A Gizzi, M Galimberti, R J Clarke, and H Ruhl. Proton imaging: a diagnostic for inertial confinement fusion/fast ignitor studies. *Plasma Physics and Controlled Fusion*, 43(12A):A267–A276, Nov 2001.

[74] M. Roth, T. E. Cowan, M. H. Key, S. P. Hatchett, C. Brown, W. Fountain, J. Johnson, D. M. Pennington, R. A. Snavely, S. C. Wilks, and et al. Fast ignition by intense laser-accelerated proton beams. *Physical Review Letters*, 86(3):436–439, Jan 2001.

[75] M. Borghesi, S. Kar, R. Prasad, F. K. Kakolee, K. Quinn, H. Ahmed, G. Sarri, B. Ramakrishna, B. Qiao, M. Geissler, and et al. Ion source development and radiobiology applications within the libra project. *Laser Acceleration of Electrons, Protons, and Ions; and Medical Applications of Laser-Generated Secondary Sources of Radiation and Particles*, May 2011.

[76] Luis O. Silva, Michael Marti, Jonathan R. Davies, and Ricardo A. Fonseca. Proton shock acceleration in laser-plasma interactions. *Physical Review Letters*, 92(1), Jan 2004.

[77] V K Tripathi, C S Liu, X Shao, B Eliasson, and R Z Sagdeev. Laser acceleration of monoenergetic protons in a self-organized double layer from thin foil. *Plasma Physics and Controlled Fusion*, 51(2):024014, Jan 2009.

[78] Paul McKenna, David Neely, Robert Bingham, and Dino Jaroszynski. *Laser-plasma Interactions and Applications*. Springer, 2013.

[79] S. C. Wilks, A. B. Langdon, T. E. Cowan, M. Roth, M. Singh, S. Hatchett, M. H. Key, D. Pennington, A. MacKinnon, and R. A. Snavely. Energetic proton generation in ultra-intense laser solid interactions. *Phys. Plasmas*, 8(2):542, 2001.

[80] R. Snavely, M. Key, S. Hatchett, T. Cowan, M. Roth, T. Phillips, M. Stoyer, E. Henry, T. Sangster, and M. Singh. Intense high-energy proton beams from petawatt-laser irradiation of solids. *Physical Review Letters*, 85(14):2945–2948, Oct 2000.

[81] L. Romagnani, J. Fuchs, M. Borghesi, P. Antici, P. Audebert, F. Ceccherini, T. Cowan, T. Grismayer, S. Kar, and A. Macchi. Dynamics of electric fields driving the laser acceleration of multi-MeV protons. *Physical Review Letters*, 95(19), Oct 2005.

[82] Marco Borghesi, J. Fuchs, S.V. Bulanov, A.J. Mackinnon, P. Patel, and M. Roth. Fast ion generation by high-intensity laser irradiation of solid targets and applications. *Fusion Science And Technology*, 49:412–439, 2006.

[83] J. F. Ziegler. http://www.srim.org/, 2016.

[84] J. F.. Ziegler, J. P. Biersack, and M. D. Ziegler. *The stopping and range of ions in matter*. 2008.

[85] M. Borghesi, D.H. Campbell, A. Schiavi, O. Willi, A.J. Mackinnon, D. Hicks, P. Patel, L.A. Gizzi, M. Galimberti, and R.J. Clarke. Laser-produced protons and their application as a particle probe. *Laser Part. Beams*, 20(02), Apr 2002.

[86] T. E. Cowan, J. Fuchs, H. Ruhl, A. Kemp, P. Audebert, M. Roth, R. Stephens, I. Barton, A. Blazevic, E. Brambrink, and et al. Ultralow emittance, multi-MeV proton beams from a laser virtual-cathode plasma accelerator. *Physical Review Letters*, 92(20), May 2004.

[87] J. J. MacFarlane, I. E. Golovkin, P. R. Woodruff, D. R. Welch, B. V. Oliver, T. A. Mehlhorn, and R. B. Campbell. Simulation of the ionization dynamics

of aluminum irradiated by intense short-pulse lasers. *Proc. Inertial Fusion and Sciences Applications 2003. Amer. Nucl. Soc.*, pages 457–469, 2004.

[88] David Clark, Robert Aragonez, Thomas Archuleta, Valeria Fatherley, Albert Hsu, Justin Jorgenson, Danielle Mares, John Oertel, Kevin Oades, Paul Kemshall, Philip Thomas, Trevor Young, and Neal Pederson. A new gated x-ray detector for the orion laser facility. Technical report, Los Alamos National Laboratory, 2012.

[89] John Foster. Gxd spectrometer design for reconnection experiment (private communications). 2015.

[90] E. Baronova, B. Bucher, D. Haas, D. Fedin, A. Stepanenko, and F. N. Beg. Three-channel x-ray crystal spectrometer for diagnosing high energy density plasmas. *Review of Scientific Instruments*, 77(10):103104, 2006.

[91] L. N. Koppel and J. D. Eckels. High resolution x-ray crystal spectrographs. *Lawrence Livermore National Laboratory Report*, UCRL-79781, 1977.

[92] G.W. Fraser, M.T. Pain, J.E. Lees, C.R. Binns, J.F. Pearson, and P.R. Houghton. The characterisation of gold x-ray photocathodes. *Nuclear Instruments and Methods in Physics Research Section A: Accelerators, Spectrometers, Detectors and Associated Equipment*, 321(1-2):385–391, Sep 1992.

[93] B.L. Henke, E.M. Gullikson, and J.C. Davis. X-ray interactions: Photoabsorption, scattering, transmission, and reflection at e = 50-30,000 ev, z = 1-92. *Atomic Data and Nuclear Data Tables*, 54(2):181–342, Jul 1993.

[94] J. P. Singh and Surya Narayah Thakur, editors. *Laser Induced Breakdown Spectroscopy*. Elesvier Science, 2005.

[95] Hans R. Griem. Principles of plasma spectroscopy. 1997.

[96] D E Evans and J Katzenstein. Laser light scattering in laboratory plasmas. *Reports on Progress in Physics*, 32(1):207–271, Jan 1969.

[97] J S Ross, L Divol, C Sorce, D H Froula, and S H Glenzer. Ultraviolet thomson scattering measurements of the electron and ion features with an energetic 263 nm probe. *Journal of Instrumentation*, 6(08):P 08004, Aug 2011.

[98] D. H. Froula, S H Glenzer, N. C. Luhmann, Jr., and J. Sheffield. *Plasma scattering of electromagnetic radiation: theory and measurement techniques.* Academic Press, 2011.

[99] A. D. Edens, R. G. Adams, P. Rambo, L. Ruggles, I. C. Smith, J. L. Porter, and T. Ditmire. Study of high mach number laser driven blast waves in gases. *Phys. Plasmas*, 17(11):112104, 2010.

[100] C. F. Mckee and B. T. Draine. Interstellar shock waves. *Science*, 252(5004):397–403, Apr 1991.

[101] A. D. Edens, T. Ditmire, J. F. Hansen, M. J. Edwards, R. G. Adams, P. Rambo, L. Ruggles, I. C. Smith, and J. L. Porter. Study of high mach number laser driven blast waves. *Phys. Plasmas*, 11(11):4968, 2004.

[102] J. F. Hansen, M. J. Edwards, D. H. Froula, G. Gregori, A. D. Edens, and T. Ditmire. Laboratory observation of secondary shock formation ahead of a strongly radiative blast wave. *Phys. Plasmas*, 13(2):022105, 2006.

[103] I.S. Shklovskii. Supernova outbursts and the interstellar medium. *Soviet Astronomy*, 6:162, 1962.

[104] C. C. Kuranz, R. P. Drake, C. M. Krauland, D. C. Marion, M. J. Grosskopf, E. Rutter, B. Torralva, J. P. Holloway, D. Bingham, J. Goh, and et al. Initial conditions of radiative shock experiments. *Phys. Plasmas*, 20(5):056321, 2013.

[105] E. R. Tubman, R. Crowston, R. Alraddadi, H.W. Doyle, J. Meinecke, J.E. Cross, R. Bolis, D. Lamb, P. Tzeferacos, D. Doria, B. Reville, H. Ahmed, M. Borghesi, G. Gregori, and N.C. Woolsey. Nanosecond imaging of shock- and jet-like features. *IEEE Transactions on Plasma Science*, PP 99, 2014.

[106] Specialised Imaging. Framing cameras, 2016.

[107] Sony icx285al data sheet, 2013.

[108] L. G. Kam. Early evolution of laser produced blast wave in the laboratory. Master's thesis, Unviersity of York, 2015.

[109] E. R. Tubman, R. Crowston, R. Alraddadi, H. Doyle, J. Meinecke, J. Cross, R. Bolis, D. Lamb, P. Tzeferacos, D. Doria, B. Reville, H. Ahmed, M. Borghesi, G. Gregori, and N. Woolsey. The evolution of plasma shock waves on the sub-microsecond timescales. *CLF Annual Report 2013-14*, 2014.

[110] A. K. Rossall, G. J. Tallents, E. Wagenaars, and N. C. Woolsey. Enhancement of x-ray generation in a high-repetition-rate laser-plasma experiment. *IEEE Transactions on Plasma Science*, 39(11):2788–2789, Nov 2011.

[111] J.J. MacFarlane, I.E. Golovkin, and P.R. Woodruff. Helios-cr a 1-d radiation-magnetohydrodynamics code with inline atomic kinetics modeling. *Journal of Quantitative Spectroscopy and Radiative Transfer*, 99(1-3):381–397, May 2006.

[112] B. Fryxell, K. Olson, P. Ricker, F. X. Timmes, M. Zingale, D. Q. Lamb, P. MacNeice, R. Rosner, J. W. Truran, and H. Tufo. Flash: An adaptive mesh hydrodynamics code for modeling astrophysical thermonuclear flashes. *Astrophys J Suppl S*, 131(1):273–334, Nov 2000.

[113] R. H. H. Scott. Flash simulations (private communications). 2016.

[114] P D Roberts, S J Rose, P C Thompson, and R J Wright. The stability of multiple-shell icf targets. *J. Phys. D: Appl. Phys.*, 13(11):1957–1969, Nov 1980.

[115] A G R Thomas, R J Kingham, and C P Ridgers. Rapid self-magnetization of laser speckles in plasmas by nonlinear anisotropic instability. *New J. Phys.*, 11(3):033001, Mar 2009.

[116] H. K. Park, N. C. Luhmann, Jr., A. J. H. Donne, I. G. J. Classen, C. W. Domier, E. Mazzucato, T. Munsat, M. J. van de Pol, and Z. Xia. Observation of high-field-side crash and heat transfer during sawtooth oscillation in magnetically confined plasmas. *Physical Review Letters*, 96(19):195003, May 2006.

[117] T. Munsat, H. K. Park, I. G. J. Classen, C. W. Domier, A. J. H. Donne, N. C. Luhmann, Jr., E. Mazzucato, M. J. van de Pol, and TEXTOR Team.

Localization of the magnetic reconnection zone during sawtooth crashes in tokamak plasmas. *Nuclear Fusion*, 47:L31–L35, November 2007.

[118] Masaaki Yamada. Progress in understanding magnetic reconnection in laboratory and space astrophysical plasmas. *Physics of Plasmas*, 14(5):058102, 2007.

[119] J. Egedal, W. Fox, N. Katz, M. Porkolab, K. Reim, and E. Zhang. Laboratory observations of spontaneous magnetic reconnection. *Physical Review Letters*, 98(1), Jan 2007.

[120] Masaaki Yamada, Russell Kulsrud, and Hantao Ji. Magnetic reconnection. *Reviews of Modern Physics*, 82(1):603–664, Mar 2010.

[121] Masaaki Yamada. Review of controlled laboratory experiments on physics of magnetic reconnection. *Journal of Geophysical Research*, 104(A7):14529, 1999.

[122] Eric Priest and Terry Forbes. *Magnetic Reconnection: MHD Theory and Applications*. Cambridge University Press, 2000.

[123] Dieter Biskamp. *Magnetic Reconnection in Plasmas (Cambridge Monographs on Plasma Physics)*. Cambridge University Press, 2005.

[124] *Reconnection of Magnetic Fields: Magnetohydrodynamics and Collisionless Theory and Observations*. Cambridge University Press, 2007.

[125] William Lewis. *Magnetic Reconnection: Theoretical and Observational Perspectives*. Springer, 2012.

[126] M. Yates, D. van Hulsteyn, H. Rutkowski, G. Kyrala, and J. Brackbill. Experimental evidence for self-generated magnetic fields and remote energy deposition in laser-irradiated targets. *Physical Review Letters*, 49(23):1702–1704, Dec 1982.

[127] P. M. Nilson, L. Willingale, M. C. Kaluza, C. Kamperidis, S. Minardi, M. S. Wei, P. Fernandes, M. Notley, S. Bandyopadhyay, M. Sherlock, R. J. Kingham, M. Tatarakis, Z. Najmudin, W. Rozmus, R. G. Evans, M. G. Haines, A. E.

Dangor, and K. Krushelnick. Bidirectional jet formation during driven magnetic reconnection in two-beam laser-plasma interactions. *Physics of Plasmas*, 15(9):092701, September 2008.

[128] L. Willingale, P. M. Nilson, M. C. Kaluza, A. E. Dangor, R. G. Evans, P. Fernandes, M. G. Haines, C. Kamperidis, R. J. Kingham, C. P. Ridgers, and et al. Proton deflectometry of a magnetic reconnection geometry. *Physics of Plasmas*, 17(4):043104, 2010.

[129] Jiayong Zhong, Yutong Li, Xiaogang Wang, Jiaqi Wang, Quanli Dong, Chijie Xiao, Shoujun Wang, Xun Liu, Lei Zhang, Lin An, and et al. Modelling loop-top x-ray source and reconnection outflows in solar flares with intense lasers. *Nat Phys*, 6(12):984–987, Dec 2010.

[130] Xun Liu, Yutong Li, Jiayong Zhong, Quanli Dong, Shoujun Wang, Lei Zhang, Jianqiang Zhu, Gang Zhao, and Jie Zhang. Characteristics of plasma jets in laser-driven magnetic reconnection. *Plasma Science and Technology*, 14(2):97–101, Feb 2012.

[131] Quan-Li Dong, Shou-Jun Wang, Quan-Ming Lu, Can Huang, Da-Wei Yuan, Xun Liu, Xiao-Xuan Lin, Yu-Tong Li, Hui-Gang Wei, Jia-Yong Zhong, and et al. Plasmoid ejection and secondary current sheet generation from magnetic reconnection in laser-plasma interaction. *Physical Review Letters*, 108(21), May 2012.

[132] Ze-Chen Zhang, Quan-Ming Lu, Quan-Li Dong, San Lu, Can Huang, Ming-Yu Wu, Zheng-Ming Sheng, Shui Wang, and Jie Zhang. Particle-in-cell simulations of fast magnetic reconnection in laser-plasma interaction. *Chinese Physics Letters*, 30(4):045201, Apr 2013.

[133] San-Qiu Liu, Xiao-Song Yang, and Xiao-Qing Li. Fast magnetic reconnection driven by ponderomotive force in two-beam laser-solid interactions. *Phys. Plasmas*, 18(11):112109, 2011.

[134] D. Biskamp. Magnetic reconnection via current sheets. *Physics of Fluids*, 29(5):1520, 1986.

[135] S. I. Syrovatsky. Formation of current sheet in a pasma with a frozen-in strong magnetic field. *Sov. Phys. JETP*, 33:933, 1971.

[136] L. Gao, P. M. Nilson, I. V. Igumenshchev, M. G. Haines, D. H. Froula, R. Betti, and D. D. Meyerhofer. Precision mapping of laser-driven magnetic fields and their evolution in high-energy-density plasmas. *Physical Review Letters*, 114(21), May 2015.

[137] L. Lancia, B. Albertazzi, C. Boniface, A. Grisollet, R. Riquier, F. Chaland, K.-C. Le Thanh, Ph. Mellor, P. Antici, S. Buffechoux, and et al. Topology of megagauss magnetic fields and of heat-carrying electrons produced in a high-power laser-solid interaction. *Physical Review Letters*, 113(23), Dec 2014.

[138] J. A. Stamper, K. Papadopoulos, R. N. Sudan, S. O. Dean, E. A. McLean, and J. M. Dawson. Spontaneous magnetic fields in laser-produced plasmas. *Physical Review Letters*, 26(17):1012–1015, Apr 1971.

[139] S. W. Haan, J. D. Lindl, D. A. Callahan, D. S. Clark, J. D. Salmonson, B. A. Hammel, L. J. Atherton, R. C. Cook, M. J. Edwards, S. Glenzer, and et al. Point design targets, specifications, and requirements for the 2010 ignition campaign on the national ignition facility. *Phys. Plasmas*, 18(5):051001, 2011.

[140] C. K. Li, F. H. Seguin, J. A. Frenje, J. R. Rygg, R. D. Petrasso, R. P. J. Town, P. A. Amendt, S. P. Hatchett, O. L. Landen, A. J. Mackinnon, and et al. Measuring e and b fields in laser-produced plasmas with monoenergetic proton radiography. *Physical Review Letters*, 97(13), Sep 2006.

[141] M.J. Rosenberg, C.K. Li, W. Fox, I. Igumenshchev, F.H. Seguin, R.P.J. Town, J.A. Frenje, C. Stoeckl, V. Glebov, and R.D. Petrasso. A laboratory study of asymmetric magnetic reconnection in strongly driven plasmas. *Nature Communications*, 6:6190, Feb 2015.

[142] G. Fiksel, W. Fox, A. Bhattacharjee, D. H. Barnak, P.-Y. Chang, K. Germaschewski, S. X. Hu, and P. M. Nilson. Magnetic reconnection between colliding magnetized laser-produced plasma plumes. *Physical Review Letters*, 113(10), Sep 2014.

[143] Erich S. Weibel. Spontaneously growing transverse waves in a plasma due to an anisotropic velocity distribution. *Physical Review Letters*, 2(3):83–84, Feb 1959.

[144] M. J.-E. Manuel, C. K. Li, F. H. Seguin, N. Sinenian, J. A. Frenje, D. T. Casey, R. D. Petrasso, J. D. Hager, R. Betti, S. X. Hu, and et al. Instability-driven electromagnetic fields in coronal plasmas. *Phys. Plasmas*, 20(5):056301, 2013.

[145] Y. Kuramitsu, Y. Sakawa, S. Dono, C. D. Gregory, S. A. Pikuz, B. Loupias, M. Koenig, J. N. Waugh, N. Woolsey, T. Morita, and et al. Kelvin-helmholtz turbulence associated with collisionless shocks in laser produced plasmas. *Physical Review Letters*, 108(19), May 2012.

[146] A. S. Joglekar. Impacta simulations (private communications). 2016.

[147] Michael Hesse, Joachim Birn, and Masha Kuznetsova. Collisionless magnetic reconnection: Electron processes and transport modeling. *Journal of Geophysical Research: Space Physics*, 106(A3):3721–3735, Mar 2001.

[148] P. Graham. Nym simulations (private communications). 2015.

[149] W. Fox, A. Bhattacharjee, and K. Germaschewski. Magnetic reconnection in high-energy-density laser-produced plasmas. *Phys. Plasmas*, 19(5):056309, 2012.

[150] W. Fox, A. Bhattacharjee, and K. Germaschewski. Fast magnetic reconnection in laser-produced plasma bubbles. *Physical Review Letters*, 106(21), May 2011.

[151] M. Tatarakis, I. Watts, F. N. Beg, E. L. Clark, A. E. Dangor, A. Gopal, M. G. Haines, P. A. Norreys, U. Wagner, M.-S. Wei, and et al. Measuring huge magnetic fields. *Nature*, 415(6869):280, Jan 2002.

[152] N. C. Woolsey, Y. Abou Ali, R. G. Evans, R. A. D. Grundy, S. J. Pestehe, P. G. Carolan, N. J. Conway, R. O. Dendy, P. Helander, K. G. McClements, and et al. Collisionless shock and supernova remnant simulations on vulcan. *Phys. Plasmas*, 8(5):2439, 2001.

[153] H. Daido, F. Miki, K. Mima, M. Fujita, K. Sawai, H. Fujita, Y. Kitagawa, S. Nakai, and C. Yamanaka. Generation of a strong magnetic field by an intense co 2 laser pulse. *Physical Review Letters*, 56(8):846–849, Feb 1986.

[154] J J Santos, M Bailly-Grandvaux, L Giuffrida, P Forestier-Colleoni, S Fujioka, Z Zhang, P Korneev, R Bouillaud, S Dorard, D Batani, and et al. Laser-driven platform for generation and characterization of strong quasi-static magnetic fields. *New J. Phys.*, 17(8):083051, Aug 2015.

[155] Shinsuke Fujioka, Zhe Zhang, Kazuhiro Ishihara, Keisuke Shigemori, Youichiro Hironaka, Tomoyuki Johzaki, Atsushi Sunahara, Naoji Yamamoto, Hideki Nakashima, Tsuguhiro Watanabe, and et al. Kilotesla magnetic field due to a capacitor-coil target driven by high power laser. *Scientific Reports*, 3, Jan 2013.

[156] C. Courtois, A. D. Ash, D. M. Chambers, R. A. D. Grundy, and N. C. Woolsey. Creation of a uniform high magnetic-field strength environment for laser-driven experiments. *Journal of Applied Physics*, 98(5):054913, 2005.

[157] Lan Gao, Hantao Ji, Gennady Fiksel, William Fox, Michelle Evans, and Noel Alfonso. Ultrafast proton radiography of the magnetic fields generated by a laser-driven coil current. *Phys. Plasmas*, 23(4):043106, Apr 2016.

[158] B. J. Zhu, Y. T. Li, D. W. Yuan, Y. F. Li, F. Li, G. Q. Liao, J. R. Zhao, J. Y. Zhong, F. B. Xue, S. K. He, and et al. Strong magnetic fields generated with a simple open-ended coil irradiated by high power laser pulses. *Applied Physics Letters*, 107(26):261903, Dec 2015.

[159] C. Goyon and B. B. Pollock. Thomson scattering (private communications). 2016.

[160] Frederick W. Grover. *Inductance Calculations: Working Formulas and Tables*. Dover Books on Electrical Engineering, 2009.

[161] Andre Vander Vorst, Arye Rosen, and Youji Kotsuka. *RF/Microwave Interaction with Biological Tissues*. Wiley-Blackwell, Dec 2005.

[162] Lyman Spitzer and Richard Harm. Transport phenomena in a completely ionized gas. *Physical Review*, 89(5):977–981, Mar 1953.

[163] P McKenna, D A MacLellan, N M H Butler, R J Dance, R J Gray, A P L Robinson, D Neely, and M P Desjarlais. Influence of low-temperature resistivity on fast electron transport in solids: scaling to fast ignition electron beam parameters. *Plasma Physics and Controlled Fusion*, 57(6):064001, Apr 2015.

[164] D. A. MacLellan, D. C. Carroll, R. J. Gray, N. Booth, M. Burza, M. P. Desjarlais, F. Du, B. Gonzalez-Izquierdo, D. Neely, H. W. Powell, and et al. Annular fast electron transport in silicon arising from low-temperature resistivity. *Physical Review Letters*, 111(9), Aug 2013.

[165] Y. T. Lee and R. M. More. An electron conductivity model for dense plasmas. *Phys. Fluids*, 27(5):1273, 1984.

[166] David R. Blackman, A. P. L. Robinson, and John Pasley. Role of low temperature resistivity on fast electron transport in disordered aluminium and copper. *Phys. Plasmas*, 22(8):083108, Aug 2015.